

# Bright and Stable Betatron Beams from Laser-Driven Plasma Wakefield

## Dissertation

zur Erlangung des akademischen Grades  
doctor rerum naturalium (Dr. rer. nat.)



---

seit 1558

vorgelegt dem Rat der Physikalisch-Astronomischen  
Fakultät der Friedrich-Schiller-Universität Jena

von **Harsh**, M. Sc.

geboren am 17.07.1991 in Saharsa, Indien

## **Gutachter**

1. Prof. Dr. Matt Zepf  
Institut für Optik und Quantenelektronik  
Friedrich-Schiller-Universität Jena
  
2. Prof. Dr. Bernard Hidding  
Department of Laser Plasma Physik  
Heinrich Heine University Düsseldorf
  
3. Dr. Charlotte Palmer  
School of Mathematics and Physics  
Queen's University Belfast

Tag der Disputation: 25. 10. 2024

# Abstract

The acceleration of electron bunches reaching GeV energies within a centimeter-scale device exemplifies the remarkable advancements achieved in the field of laser-plasma acceleration. One essential by-product of such acceleration process is the production of highly energetic X-ray photons.

In this thesis, I will detail an experimental research centered on Laser Wakefield Acceleration (LWFA). The main focus of this research is directed towards exploiting LWFA as compact sources of brilliant, hard synchrotron radiation, commonly referred to as betatron radiation.

The primary result of the thesis follows the production of hard X-ray photons in keV regime using gas cell as the target for LWFA through ionisation injection scheme. The gas cell length was kept much longer than the electron dephasing length with an anticipation of the overlap of the laser fields with the charge trapped inside the plasma wave. This overlap could result in stronger transverse oscillation of the trapped electron bunches and an increase in the total emission of the X-rays produced by the LWFA. Hydrogen and Helium were used as the background gas with Nitrogen as the dopant. The resulting X-rays showed high critical energy, peak brilliance and source size at par with the results shown by other groups [1–4]. Additionally, the X-rays produced boast of high degree of shot to shot stability and reproducibility paving way for the implementation of single shot imaging set-up at JETi200 laser system in Jena, Germany.

Another result discusses the production of quasi-monoenergetic electron beams from LWFA by implementing shock-front injection mechanism [5, 6]. The X-ray beam measured from such quasi-monoenergetic beams were found to have critical energy similar to [7]. However, the X-ray beam had lower critical energy and photon yield than the beams produced using ionization injection mechanism. Therefore, to increase the betatron yield, a new experimental configuration was implemented to break the axial-symmetry of the injected electrons and to increase the transverse oscillation amplitude of the injected electron bunch by asymmetric injection, achieved experimentally by rotating the shockfront. This configuration aimed at increasing the betatron yield has its results supported by 2D PIC simulations.

# Zusammenfassung

Die Beschleunigung von Elektronenpaketen, die in einem zentimetergroßen Gerät GeV-Energien erreichen, ist ein Beispiel für die bemerkenswerten Fortschritte, die auf dem Gebiet der Laser-Plasma-Beschleunigung erzielt wurden. Ein wesentliches Nebenprodukt einer solchen Wechselwirkung ist die Erzeugung hochenergetischer Röntgenphotonen.

In dieser Arbeit werde ich eine experimentelle Forschungsarbeit zur Laser-Wakefield-Beschleunigung (LWFA) vorstellen. Das Hauptaugenmerk dieser Forschung liegt auf der Nutzung von LWFA als kompakte Quellen für brillante, harte Synchrotronstrahlung, die gemeinhin als Betatronstrahlung bezeichnet wird.

Das Hauptergebnis der Arbeit ist die Erzeugung harter Röntgenphotonen im keV-Bereich unter Verwendung einer Gaszelle als Target für LWFA. Die Länge der Gaszelle wurde viel länger gehalten als die Elektronendephaselänge, und ihre Auswirkung auf die erzeugten Röntgenphotonen wurde untersucht. Wasserstoff wurde als Hintergrundgas und Stickstoff als Dotiergas verwendet. Die erzeugte Röntgenstrahlung zeigte eine hohe kritische Energie, Spitzenbrillanz und Quellengröße, die mit den Ergebnissen anderer Gruppen vergleichbar sind. [1–4]. Darüber hinaus zeichnen sich die erzeugten Röntgenstrahlen durch ein hohes Maß an Stabilität und Reproduzierbarkeit aus und ebnet den Weg für die Implementierung eines Single-Shot-Imaging-Setups am JETi200-Lasersystem in Jena.

Ein weiteres Ergebnis ist die Erzeugung quasi-monoenergetischer Elektronenstrahlen aus LWFA durch die Implementierung eines Stoßfront-Injektionsmechanismus. Es wurde festgestellt, dass der aus solchen quasi-monoenergetischen Strahlen gemessene Röntgenstrahl eine ähnliche kritische Energie wie [7] aufweist. Der Röntgenstrahl hatte jedoch eine geringere Photonenausbeute als die Strahlen, die mit dem Ionisationsinjektionsmechanismus erzeugt wurden. Um die Betatronausbeute zu erhöhen, wurde daher eine neue experimentelle Konfiguration implementiert, um die axiale Symmetrie der injizierten Elektronen zu brechen und die transversale Oszillationsamplitude des injizierten Elektronenpakets durch asymmetrische Injektion zu erhöhen, was experimentell durch Rotation der Stoßfront erreicht wurde. Die Ergebnisse dieser Konfiguration zur Erhöhung der Betatronausbeute werden durch 2D-PIC-Simulationen bestätigt.

# Contents

<b>Abstract</b>	<b>iii</b>
<b>Zusammenfassung</b>	<b>i</b>
<b>1 Introduction</b>	<b>1</b>
1.1 Particle accelerators as light sources . . . . .	2
1.1.1 Insertion devices . . . . .	2
1.1.2 X-ray applications . . . . .	4
1.2 Laser wakefield acceleration . . . . .	6
1.3 Betatron Radiation as an X-ray source from Laser-Wakefield Acceleration	7
1.4 Thesis Outline . . . . .	8
<b>2 Theory</b>	<b>10</b>
2.1 Fundamentals of laser propagation in plasma . . . . .	11
2.2 Plasma effects at relativistic laser intensities . . . . .	12
2.3 Plasma based electron acceleration using high-power lasers . . . . .	17
2.3.1 Single electron motion in a laser field . . . . .	17
2.3.2 Electron acceleration in laser-generated plasma waves . . . . .	19
2.3.3 Laser wakefield acceleration in the blow-out regime . . . . .	23
2.4 Numerical 2D PIC simulations . . . . .	26
2.5 Secondary "betatron" radiation generation . . . . .	29
2.5.1 Electron orbit within the laser wakefield . . . . .	31
2.5.2 Radiation fundamentals . . . . .	32
<b>3 Experimental Methods and Diagnostics</b>	<b>36</b>
3.1 JETi200 Laser system . . . . .	36
3.1.1 Laser beam profile . . . . .	37
3.1.2 Gas targets . . . . .	39
3.2 Electron beam characterization . . . . .	41
3.3 Betatron beam characterization . . . . .	42
3.3.1 Detection System . . . . .	43
3.3.2 Betatron Beam Profile and Source Size . . . . .	46
3.3.3 Betatron Beam Spectral Characterisation . . . . .	48

---

<b>4</b>	<b>Bright and Stable X-rays from Ionization Injection</b>	<b>51</b>
4.1	Electron Beam Measurements . . . . .	51
4.2	Betatron Beam Measurements . . . . .	56
4.2.1	Reduced gas cell length . . . . .	60
4.2.2	Energy spectrum of the betatron beam . . . . .	63
4.3	Summary . . . . .	69
<b>5</b>	<b>Quasi-monoenergetic Electron Beam and Betatron Radiation</b>	<b>71</b>
5.1	Shock-front Injection . . . . .	71
5.1.1	Electron Beam Measurements . . . . .	72
5.1.2	Betatron Beam Measurements . . . . .	74
5.2	Betatron Beam Enhancement using Shock-Front Rotation . . . . .	78
5.2.1	2D PIC Simulation for Rotating Shock-front . . . . .	81
5.3	Summary . . . . .	86
<b>6</b>	<b>Discussions and Outlook</b>	<b>87</b>
6.1	Discussion of Results . . . . .	87
6.2	Outlook . . . . .	89
	<b>Appendix</b>	<b>92</b>
	<b>Bibliography</b>	<b>95</b>
	<b>List of Publications</b>	<b>109</b>
	<b>Danksagung</b>	<b>111</b>
	<b>Ehrenwörtliche Erklärung</b>	<b>113</b>
	<b>CV</b>	<b>114</b>



# 1 Introduction

At the core of scientific exploration lies the quest to enhance our understanding of the fundamental principles governing the natural world. Particle accelerators, which were first invented in the 1930s, have played a pivotal role in scientific discoveries and have found diverse applications in fields ranging from industry to healthcare. These accelerators, capable of accelerating particles to highly relativistic speeds, have led to significant advancements in modern science. The ongoing development of accelerator technology has resulted in ever-increasing particle energies and installment of more than ten thousand accelerators worldwide. A prominent example is the Large Hadron Collider (LHC) located at CERN in Geneva. The LHC serves as the world's most powerful microscope, with the aim of unraveling the internal structure of particles such as protons and neutrons. Through this colossal machine, researchers have made groundbreaking discoveries, including the detection of the Higgs boson, a particle responsible for giving mass to all other particles [8–10].

However, the LHC also exemplifies a fundamental challenge associated with conventional accelerators: the need for significant physical dimensions to achieve high particle energies. With a diameter of 27 km, the LHC stands as the largest accelerator on Earth. This size is primarily attributed to the acceleration technique. The charged particles are accelerated by traversing high electric field gradients within traditional metal cavities. The maximum field strength achievable in these cavities is around 100 MV/m. Fields exceeding this limit are susceptible to material breakdown, a phenomenon where electrons from the metal surface are drawn into the vacuum, resulting in the destruction of accelerating structure. Consequently, achieving higher particle energies requires a huge number of such cavities, ultimately requiring more physical space. In circular accelerators, particles are guided through multiple passes of the same acceleration cavities to amplify energy gains. However, the minimum diameter of the particle's orbit is constrained by energy losses attributable to synchrotron radiation.

Plasma accelerators brings innovative acceleration techniques to surpass the underlying limitations of material breakdown and enable the development of the next generation of small scale accelerators. The reduced scale and cost compared to traditional large-scale facilities could facilitate more widespread exploration of high-energy particle research, helping a greater number of scientists and institutions to contribute to advancements in this important scientific domain.

## 1.1 Particle accelerators as light sources

By employing thoughtful design, it's possible to generate a significant portion of the synchrotron radiation in the X-ray ( $>1$  keV) regime of the electromagnetic spectrum using particle accelerators. These sources have become highly sought-after for a wide array of applications, as demonstrated by the existence of more than 50 operational and planned synchrotron light sources worldwide, each equipped with multiple beamlines [11]. In the following section, we will provide a concise explanation of how these light sources operate, followed by an overview of their numerous applications. Additionally, we will delve into the concepts of average and peak brightness, highlighting the advantages that these sources offer over traditional x-ray tube technology. We will touch on the physics and findings associated with hard x-ray free electron lasers (X-FELs), representing the cutting edge of modern x-ray technology. This section will conclude with an exploration of the limitations inherent to these remarkable devices.

### 1.1.1 Insertion devices

While certain beamlines harness synchrotron radiation generated by bending magnets, a significant number opt for an insertion device configuration, which comprises a series of dipole magnets with alternating polarity (as illustrated in Figure 1.1). The insertion device offers a distinct advantage: it emits radiation from multiple oscillations of electrons in the forward direction, yielding a considerably brighter source compared to a bending magnet.

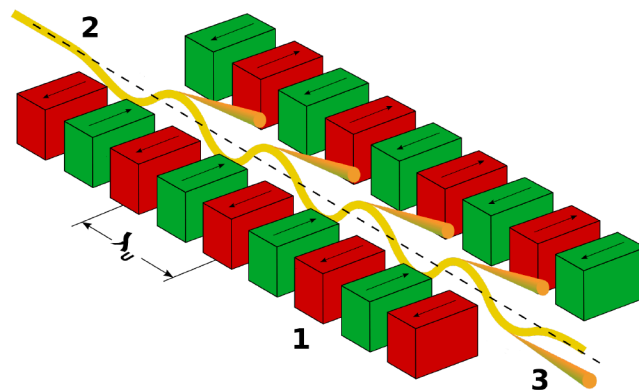


Figure 1.1: A diagram of an insertion device [12]. A relativistic electron beam (2) is wiggled by an assembly of magnets having alternating polarity (1) and spacing  $\lambda_u$  to produce a bright X-ray beam.

The insertion devices are often characterized by the dimensionless, undulator or

wiggler, parameter  $\mathfrak{K}$ , where

$$\mathfrak{K} = \frac{eB_0\lambda_u}{2\pi m_e c} \quad (1.1)$$

$B_0$  is the peak magnetic field in the device and  $\lambda_u$  is the dipole magnet spacing. When  $\mathfrak{K} \ll 1$ , the device is referred to as an undulator, and it emits monochromatic radiation due to the convergence and interference of emitted light cones. In essence, an undulator operates similar to a diffraction grating, where light emanating from distinct sources (points along the electron beam path) constructively interferes only when the source locations are spaced apart by an integer number of wavelengths. For an undulator, the wavelength of on-axis radiation emission is determined by the equation:

$$\lambda = \frac{\lambda_u}{2\gamma_e^2} \left( 1 + \frac{\mathfrak{K}^2}{2} \right) \quad (1.2)$$

where  $\gamma_e$  is the relativistic electron factor. The high value of  $\gamma_e$  available in modern particle accelerators, typically a few thousand, results in the generation of short-wavelength radiation. This radiation is tightly focused within a narrow cone with an opening angle of  $\approx 1/\gamma_e$ , making it an extremely valuable x-ray source.

For  $\mathfrak{K} > 1$  a white light continuum is produced and the insertion device is referred to as a wiggler. X-ray sources that utilize relativistic electron beams interacting with insertion devices are commonly referred to as 3rd generation light sources.

Peak brightness is a widely used metric for assessing x-ray sources. It is quantified in units of photons per second per square millimeter per milli-radian per 0.1 % bandwidth (photons/s/mm<sup>2</sup>/mrad<sup>2</sup>/0.1%BW). In essence, it represents the number of photons generated per second within a bandwidth of 0.1% centered around a specific energy, divided by the cross-sectional area and divergence of the beam. To put this into context, typical x-ray tube sources exhibit brightness values in the range of  $10^8$  to  $10^{10}$  photons/s/mm<sup>2</sup>/mrad<sup>2</sup>/0.1%BW. In contrast, synchrotron sources can achieve average brightness levels as high as  $10^{20}$  photons/s/mm<sup>2</sup>/mrad<sup>2</sup>/0.1%BW and peak brightness of  $10^{24}$  photons/s/mm<sup>2</sup>/mrad<sup>2</sup>/0.1%BW [13]. Here, the peak brightness is attributed to the single bunch of electrons whereas, the average brightness is determined by taking a time-average measurement over a considerable number of these electron bunches.

One such insertion device having highest peak brightness available currently is called X-ray free electron laser which will be discussed next.

**X-ray free electron lasers** In the year 2009, the world's first hard x-ray free electron laser (X-FEL), LCLS, began lasing. A free-electron laser (FEL), represents a 4th generation light source and is comprised of an electron accelerator followed

by a long undulator. As electrons move through the undulator's magnetic field, the radiation they emit starts to modulate the electron beam. This modulation leads to micro-bunching of the electron bunches at the wavelength of the emitted radiation. Once this micro-bunching is established, the electron bunches oscillate in phase and emit radiation that gains amplification from the electrons themselves. To initiate this process, seeding is essential. Seeding can occur naturally from random shot noise, and the radiation gets amplified in a phenomenon known as Self-Amplified Spontaneous Emission (SASE). This process is the standard operating mode for facilities like LCLS (Linac Coherent Light Source) and results in an exceptionally bright source of hard x-rays, with LCLS reaching a peak brightness of  $10^{33}$  photons/s/mm<sup>2</sup>/mrad<sup>2</sup>/0.1%BW [13].

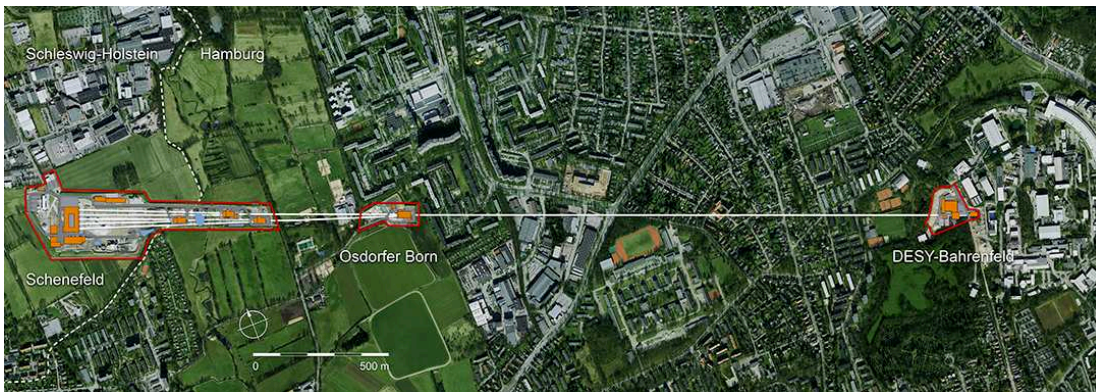


Figure 1.2: Aerial view of European X-ray Free Electron Laser spanning 3 km [14].

The LCLS counterpart European XFEL (Fig: 1.2) started operating in the year 2017 registering a peak brightness of  $5 \times 10^{33}$  photons/s/mm<sup>2</sup>/mrad<sup>2</sup>/0.1%BW at a rep. rate of 27 KHz. The European XFEL provides x-ray pulses with a duration of less than 100 fs for wavelengths from 0.05 nm to 4.7 nm and is 3 km long [14]. Figure 1.3 shows the peak x-ray brightness for a selection of 3rd and 4th generation light sources emphasising the huge gain in peak brightness due to lasing.

### 1.1.2 X-ray applications

X-ray radiation, since its discovery by Röntgen [15], has enabled numerous breakthroughs in medicine, chemistry, biology, and physics. X-rays possess the remarkable ability to penetrate various materials and biological tissues, providing a unique window into internal processes that would otherwise be inaccessible without destructive methods. The applications can mainly be categorised into spectroscopy, imaging and diffraction.

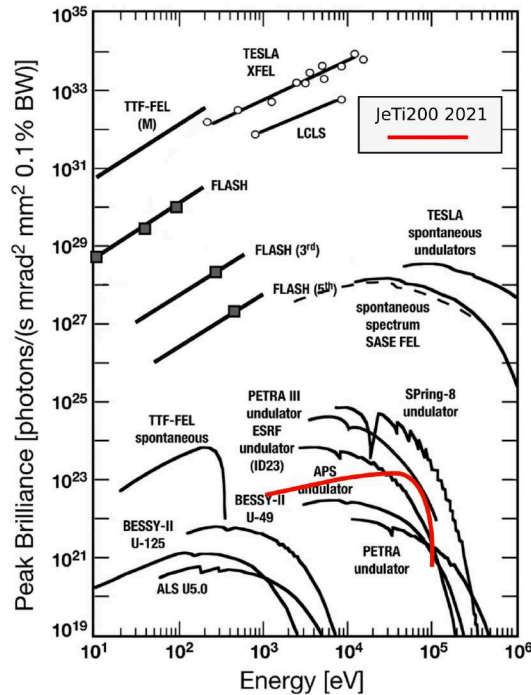


Figure 1.3: Peak brilliance of a number of third and fourth generation light sources from around the world [14]. The red solid line shows the brightness of the betatron radiation produced at the JETi200 laser facility in an experiment carried out in 2020-21, which is reported in chapter 4 of this thesis.

Spectroscopic experiments serve as powerful tools for researchers to uncover the elemental composition, chemical state, and physical properties of a wide range of materials, encompassing both inorganic substances and biological systems. Scientists employ various types of electromagnetic radiation, such as x-rays, infrared, ultraviolet, and visible light, to explore different aspects and characteristics of samples. These investigations span diverse fields, including the examination of biomedical specimens, condensed matter, engineering materials, and magnetic substances. X-ray absorption spectroscopy, angularly resolved photoemission spectroscopy and photo-emission electron microscopy are few examples of the spectroscopic application of the X-rays [16–19].

When X-rays interact with a crystal, they undergo scattering due to the ordered arrangement of atomic planes within the crystal lattice. Diffraction studies exploit this phenomenon to examine the structural characteristics of various materials, including chemical compounds and composite substances. These materials encompass a wide range, such as minerals, ceramics, biological specimens, as well as electronic and magnetic materials. This technique provides valuable insights into the atomic and molecular arrangements within these materials. The use of diffraction techniques for

determining crystal structures has yielded numerous scientific publications. A notable example of such an achievement is the determination of charge density in various forms of buckminsterfullerene (C60) [20]. Additional insights into the correlations among ion positions within a material can be understood through spectroscopic techniques like Extended X-ray Fine Structure (EXAFS) and X-ray Absorption Near Edge Structure (XANES). These methods provide valuable information about the local structure and chemical environment of atoms in a material.

X-ray imaging is widely favored due to its ability to reveal the contents of typically opaque objects. Variations in absorption among different elements within the material create contrast, enabling the generation of informative images. Alternatively, when employing a spatially coherent x-ray beam, even slight differences in the real part of the refractive index of the material can alter the wavefront. This effect is particularly valuable for examining biological tissue samples [21]. For instance, it can highlight the edges of a tumor, which may have a very similar level of absorption to the surrounding tissue. This technique is known as phase contrast imaging (PCI). X-ray PCI has found applications in various fields, including the reading of scrolls that were damaged during the eruption of Mount Vesuvius in 79 AD [22].

Laser wakefield accelerators provide an important alternative for such X-ray applications and in the next section we will learn more about such accelerators.

## 1.2 Laser wakefield acceleration

Conventional accelerators are confronted with several constraints that impede their further progress. One notable limitation is the restricted accelerating gradients achievable in radiofrequency(RF) cavities due to the occurrence of electric breakdown within the cavity. Moreover, despite efforts to minimize the size of conventional accelerators, these machines still demand substantial physical space and financial resources. Expanding the capabilities of these accelerators to reach higher particle beam energies would require even larger and more costly facilities, rendering them economically unfeasible. Consequently, there is a pressing need for a novel acceleration mechanism that offers a reduction in size and construction expenses.

Following the introduction of chirped-pulse amplification (CPA), a Nobel Prize-winning technique [23], the peak intensities of optical lasers have experienced exponential growth. Concurrently, the number of high-intensity laser systems has surged [24]. This remarkable advancement has sparked a revolution in our understanding of interactions between light and matter, triggering transformative changes [25].

CPA's emergence has given rise to entirely new scientific domains, including strong-field atom and molecular science [26, 27], attosecond physics [28], relativistic and nonlinear optics [29], and laboratory astrophysics [30]. Furthermore, it has facilitated the realization of plasma-based laser wakefield acceleration (LWFA) [31–33], wherein a laser pulse of relativistic intensities forms an accelerating cavity with high field gradients [34].

The laser pulse's high intensity exerts a force on electrons, causing them to move away from its trajectory and resulting in exposed ions directly behind the laser pulse. This charge separation leads to a Coulomb force, which in turn draws the electrons back towards the laser's path. As these electrons are pulled back, they gain energy and surpass their equilibrium positions. These collective plasma oscillations collectively create a wakefield that travels alongside the laser pulse. Electrons introduced into this wakefield experience a potent accelerating field, enabling them to attain highly relativistic energies.

The convergence of these two technologies—ultra-relativistic particle accelerators and ultra-intense lasers—holds immense promise for advancing our understanding of the natural world. It grants access to electromagnetic fields that can reach, and potentially surpass, those encountered in extreme astrophysical environments, such as those near the surface of a neutron star [30] and also potentially be used as a driver for the next generation compact light sources [35].

## **1.3 Betatron Radiation as an X-ray source from Laser-Wakefield Acceleration**

Professor Donald Kerst played a pivotal role in the development of the world's first magnetic induction accelerator at the University of Illinois in 1940. This innovative machine went through several early names such as "rheotron," "inductron," "Super-X-Ray Machine," and "cosmic ray machine" in initial press releases. To finalize a suitable name for the accelerator, a departmental contest was organized and Kerst settled on "betatron" [36].

The LWFA systems are known to produce intense x-ray radiation referred to as 'betatron radiation' [37, 38]. This radiation is emitted by electrons undergoing transverse oscillations as they are accelerated (Fig:1.4) by the laser. Betatron x-rays have small emission cone typically spanning milli-radians and are emitted from a micron scale source [37, 39] which permits high resolution imaging in a compact geometry [40].

The spectrum of betatron radiation is broadband and resembles that of a synchrotron, covering a wide energy range with a continuous high flux. Furthermore, betatron radiation boasts an intrinsic femtosecond duration, offering exceptional temporal resolution in addition to its other advantages. It is predicted that the spectral shape resembles the on-axis synchrotron spectrum [35]. The critical energy of this spectrum, which divides the energy spectrum into equal halves above and below it, is a characteristic parameter of this phenomenon [41].

## 1.4 Thesis Outline

This thesis documents the efforts to establish a stable and highly brilliant X-ray source, aiming for future applications at the JeTi200 laser system in Jena, Thuringia, Germany. The typical setup employed for Laser Wakefield Acceleration (LWFA) is illustrated in Figure 1.4, where a laser pulse is focused on a gas target, generating LWFA electrons and betatron radiation. Through the implementation of the shockfront injection mechanism, a quasi-monoenergetic electron beam was successfully generated. The subsequent characterization of the betatron radiation emanating from these beams was conducted. Additionally, the impact of asymmetric injection on the intensity of the betatron beam was investigated.

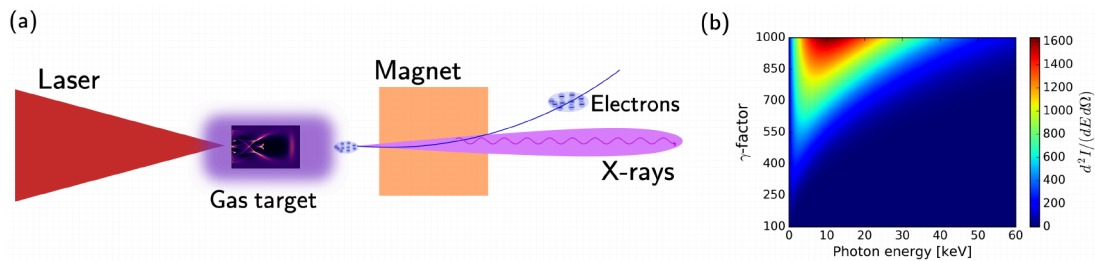


Figure 1.4: (a) A schematic for LWFA and betatron radiation. An intense laser pulse is focused onto a gas target and drives a plasma wave inside a plasma channel. The focusing forces of plasma channel causes transverse oscillation of the accelerating electrons which then emit synchrotron-like radiation. (b) Calculated synchrotron spectrum for range of electron energies at plasma density  $5 \times 10^{18} \text{ cm}^{-3}$ , keeping betatron oscillation amplitude and number of oscillations =1.

**Author's role:** The author was the Principal Investigator (PI) for all the experiments performed in this thesis done at JETi200 lab in Jena. The design of the experimental set-up, the calibration of the X-ray detector, construction of the X-ray spectrometer and 2D PIC simulations were done by the author.

The structure of the thesis consists of chapters with theoretical fundamentals, diagnostics & analysis methods and experimental results. **Chapter 2** dives into the fundamental principles of plasma and its interaction with ultrashort pulse lasers, providing insights into laser plasma acceleration. It also covers the theoretical underpinnings of synchrotron and betatron radiation.

**Chapter 3** shifts the focus towards the experimental aspects, detailing the methods employed for data acquisition in this thesis. It places particular emphasis on the diagnostics for electron beams and X-rays.

**Chapter 4 and 5** are dedicated to presenting the outcomes of the experiments conducted using ionization injection and shockfront injection mechanisms for LWFA, respectively.

Finally, **Chapter 6** serves as the conclusion of the thesis, summarizing the findings, and offering an outlook on potential future applications stemming from the results obtained.

## 2 Theory

In 1979, Tajima proposed the concept of plasma-based acceleration [42], which utilized the periodic charge density perturbations in plasma to propel charged particles using the resulting electric field. These wakefields can be induced by driver beams, such as laser pulses or energetic particles. An intriguing aspect of this accelerating structure is its existence as a plasma wave within an ionized gas, eliminating the need for fabrication and providing exceptional resistance to damage. As a result, it can sustain significantly stronger accelerating fields compared to conventional technologies.

Throughout the 1990s, initial experiments utilized long laser pulses to drive wakefields, successfully demonstrating the principle of plasma wakefield acceleration. This groundbreaking advancement was further enhanced by the development of chirped pulse amplification, for which Mourou was awarded the Nobel Prize in Physics the previous year [43]. Consequently, the field of laser plasma wakefield experiments has experienced remarkable progress and expansion.

Today's laser systems boast peak power on the order of tens of Terawatts (TW) and can achieve relativistic intensities of  $I_L \gtrsim 10^{18} \text{W/cm}^2$ , corresponding to an electric field of about  $\xi_L \gtrsim 10^{12} \text{V/m}$ . In comparison, an electron of Hydrogen atom with the atomic radius, the Bohr radius ( $a_B = \hbar^2/(m_e e^2)$ ), experiences an electric field of approximately  $|\xi_{atom}| = e/(4\pi\epsilon_0 a_B^2) \approx 5.1 \times 10^{11} \text{V/m}$ , leading to an atomic intensity of

$$I_{atom} = \frac{1}{2}\epsilon_0 c |\xi_{atom}|^2 \approx 3.5 \times 10^{16} \text{W/cm}^2. \quad (2.1)$$

Where  $\hbar$  is the reduced Planck constant,  $m_e$  rest mass of the electron,  $e$  the electron charge,  $\epsilon_0$  is the vacuum permittivity and  $c$  the speed of light in vacuum.

When these high-intensity laser pulses interact with matter, with a focus on gaseous interactions in this thesis, the laser pulse's rising edge (pre-pulse) partially or fully ionizes the target material. Understanding the relativistic laser-plasma interaction, injection schemes, electron acceleration, and the generation of secondary "betatron" radiation are crucial for comprehending the experimental work outlined in this thesis.

The following sections offer a summary of the underlying physics principles associated with the experiments described in this work. We begin by exploring the fundamentals of laser propagation in plasma (2.1), followed by an investigation of the effects of ultra-high relativistic laser pulse interactions with under-dense plasma(2.2). Subsequently, we delve into the possibilities of electron acceleration during such interactions and various methods of electron injection(2.3). Finally, we examine the generation of hard

X-rays from laser plasma interactions(2.5) .

## 2.1 Fundamentals of laser propagation in plasma

What is a plasma? According to [44], a plasma is a state of matter that consists of ionized and neutral particles. Despite the presence of charged particles, a plasma appears to be quasi-neutral, meaning that the overall charge is approximately balanced. The collective behavior of a plasma is a result of the electromagnetic interactions between its charged constituents.

A plasma primarily consists of a mixture of electrons and their heavier, positively charged parent atoms that have been dissociated. Consider a large number of particles  $\gtrsim 10^{18}$  particles/cm<sup>3</sup>, in the plasma consisting of lighter particles (electrons) doing faster oscillations compared to heavier particles (ions) doing slower oscillations [45]. In this research work, the laser-plasma interaction timescale spans several tens of femtoseconds (1fs = 10<sup>-15</sup>s), effectively causing the ions to act as a motionless background due to their higher mass-to-charge ratio. This allows us to treat ions as stationary with respect to the much faster-oscillating electrons during the laser-plasma interaction process. The large number of particles in the plasma is disturbed by the electromagnetic field of the interacting laser pulse, which oscillates the electron away from the equilibrium charge distribution with a characteristic plasma frequency  $\omega_p$ . As ions are considered motionless for the interaction time (*fs*), the plasma frequency is represented only by the frequency of the electrons,  $\omega_{p,e}$ , given by [46]

$$\omega_p \simeq \omega_{p,e} = \sqrt{\frac{e^2 n_e}{\epsilon_0 m_e}} \simeq 5.64 \times 10^{-8} \sqrt{n_e / \text{cm}^{-3}} \text{THz}. \quad (2.2)$$

Where  $m_e$  is the rest mass of the electron and  $n_e$  being the local electron density (number of electrons per unit volume). For the propagation of electromagnetic waves inside a uniform plasma, the dispersion relation can be given as

$$\omega^2 = \omega_{p,e}^2 + \kappa^2 c^2 \quad (2.3)$$

Where  $\omega$  and  $\kappa$  are the frequency and the wavenumber of the electromagnetic wave, respectively. In vacuum,  $\omega_{p,e} = 0$  (no electrons), hence the equation 2.3 gives the dispersion relation in vacuum. According to 2.3, the phase velocity of the electro-

magnetic wave is,

$$v_{\text{ph}} = \frac{\omega}{\kappa} = \frac{c}{\sqrt{1 - \left(\frac{\omega_{\text{p,e}}}{\omega}\right)^2}} = \frac{c}{\eta} \quad (2.4)$$

Where

$$\eta = \sqrt{1 - \left(\frac{\omega_{\text{p,e}}}{\omega}\right)^2} = \sqrt{1 - \frac{n_e}{n_c}} \quad (2.5)$$

is the refractive index of the plasma with

$$n_c = \frac{\epsilon_0 m_e \omega_L^2}{e^2} = \frac{1.1 \times 10^{21}}{(\lambda_L / \mu\text{m})^2} \text{cm}^3, \quad (2.6)$$

the critical plasma density for a given laser frequency,  $\omega_L$ . The critical plasma density is the electron density below which the plasma becomes transparent and the propagation of light in plasma is possible i.e.  $n_c > n_e$  ( $\omega_L > \omega_{\text{p,e}}$ ). For electromagnetic frequencies lower than the plasma frequency  $\omega_L < \omega_{\text{p,e}}$  ( $n_c < n_e$ ), the refractive index becomes imaginary (eqn. 2.5) and the electromagnetic waves are exponentially damped and will be reflected by the plasma. In this thesis, we will work only with the underdense plasma ( $n_e < n_c$ ) where the plasma becomes transparent and the electro-magnetic wave can propagate through the plasma.

When the ultra high laser intensities of the order of  $10^{18}\text{W}/\text{cm}^2$  is applied to a gaseous target, the electrons perturbed by the laser will oscillate with the speed close to  $c$  and therefore we should modify the description of laser-plasma interaction to the relativistic laser-plasma interaction. In the section 2.3, we will explore the various non-linear relativistic plasma effects which lays the theoretical groundwork for the experiments presented in the thesis but before we learn in brief about how the plasma behave under relativistic laser intensities in the next section.

## 2.2 Plasma effects at relativistic laser intensities

To describe how relativistic is a laser-plasma interaction, we use a parameter called 'laser strength parameter' denoted by  $a_0$ . It is defined as the peak amplitude of the normalized (dimensionless) vector potential of the electromagnetic wave. This parameter is given as

$$a_0 = \frac{e|\boldsymbol{\xi}_0|}{m_e \omega_L c} \simeq 0.85 \times \frac{\lambda_L}{\mu\text{m}} \cdot \sqrt{I_L / 10^{18} \frac{\text{W}}{\text{cm}^2}}, \quad (2.7)$$

Where  $|\boldsymbol{\xi}_0|$  is the electric field amplitude of the electro-magnetic wave. For a TiSa-based laser system operating at  $\lambda_L = 800\text{nm}$ ,  $a_0 = 1$  is reached at laser intensities of  $I_L \approx 2.2 \times 10^{18}\text{W/cm}^2$ .

For laser intensities,  $I_L$  corresponding to  $a_0 \ll 1$  the speed of the oscillating electrons is small compared to the speed of light and the excite plasma wave is linear, having the sinusoidal shape and the frequency equal to plasma frequency,  $\omega_p$  according to Equation 2.3 [47]. The relativistic effects are neglected in this regime. However, the laser intensities used for the experiments in this work have  $a_0 > 1$  which requires a full relativistic approach. Here the gain in the rest mass of the electron due to relativistic effects is given as  $\gamma.m_e$  determined by the  $\gamma$ - factor

$$\gamma(\mathbf{r}, t) = \left(1 - \frac{|\dot{\mathbf{r}}|^2}{c^2}\right)^{-1/2} \quad (2.8)$$

Where  $\dot{\mathbf{r}}$  is the velocity of the electron. This gain in mass will change the plasma frequency in Equation 2.3 and subsequently will change the refractive index in the Equation 2.5. This leads to

$$\omega_{p,rel} \simeq \omega_{p,e} = \sqrt{\frac{e^2 n_e}{\langle \gamma \rangle \epsilon_0 m_e}}. \quad (2.9)$$

As for the underdense plasmas  $\omega_L \gg \omega_{p,e}$  hence we can temporarily average the relativistic  $\gamma$ - factor over the fast laser oscillations and replace  $\gamma(\mathbf{r}, t)$  by  $\langle \gamma(\mathbf{r}) \rangle$  (for future purpose  $\langle \gamma(\mathbf{r}) \rangle$  will be written as  $\gamma$  for the ease of convenience). For an electron in a plane electromagnetic wave the momentary value of the relativistic  $\gamma$ - factor is related to the laser strength parameter  $a_0$  via [48]

$$\gamma \simeq 1 + \frac{a_0^2}{2}. \quad (2.10)$$

The electric laser field amplitude can also be expressed as a function of the laser strength parameter as

$$\boldsymbol{\xi}_0 \simeq 3.21 \times \frac{a_0}{\lambda_L / \mu\text{m}} \text{TV/m} \quad (2.11)$$

A change in plasma frequency, electron density or in the laser intensity can lead to a change in the refractive index (Equation 2.5). To analyse the non-linear relativistic effects, the variation of the refractive index for small modulation in a linear expansion can be expressed as [29],

$$\eta \simeq \underbrace{1 - \frac{1}{2} \frac{\omega_{p,e}^2}{\omega_L^2}}_1 \left( \underbrace{1 - \frac{\delta n_e}{n_e}}_2 - \underbrace{\frac{\langle a^2 \rangle}{2}}_3 - \underbrace{2 \frac{\delta \omega_L}{\omega_L}}_4 \right) \quad (2.12)$$

Term 1 represents the approximation of the Equation 2.5 for densities  $n_e \ll n_c$  (true for experimentally realised electron densities). Term 2 shows the normalized density perturbation  $\delta n_e$ . Term 3 describes the square of the vector potential averaged over the fast laser oscillations representing the laser intensity and the Term 4 denotes the modification to the laser frequency  $\omega_L$ .

The modulations in  $\eta$  will also change the group and phase velocity of the the laser as,

$$v_{gr} = c\eta = c \left[ 1 - \frac{1}{2} \frac{\omega_{p,e}^2}{\omega_L^2} \left( 1 - \frac{\delta n_e}{n_e} - \frac{\langle a^2 \rangle}{2} - 2 \frac{\delta \omega_L}{\omega_L} \right) \right] \quad (2.13)$$

$$v_{ph} = \frac{c}{\eta} \simeq c \left[ 1 + \frac{1}{2} \frac{\omega_{p,e}^2}{\omega_L^2} \left( 1 - \frac{\delta n_e}{n_e} - \frac{\langle a^2 \rangle}{2} - 2 \frac{\delta \omega_L}{\omega_L} \right) \right] \quad (2.14)$$

Where  $v_{gr}$  and  $v_{ph}$  are the group and phase velocity of the laser pulse. These effects shown in Figure 2.1 appear stationary in the laser pulse's frame of reference (co-moving in z-direction with the laser pulse) as a function of the pulse's frame variable  $\psi = t - z/c$  and  $\tau = t$ .

**Longitudinal changes in  $v_{gr}$ .** Consider the change of two longitudinally (temporally) separated part of the laser pulse (e.g. One part at the beginning of the laser pulse and the other at the end). Longitudinal changes of  $\mathbf{v}_{gr}$  during the laser propagation results in a longitudinal bunching of the laser pulse envelope (also called "Pulse compression " or "pulse stretching") figure 2.1 [Top] and is characterised by [29]

$$\frac{1}{L} \frac{\partial L}{\partial \tau} = -\frac{1}{c} \frac{\partial v_{gr}}{\partial \psi} \quad (2.15)$$

The longitudinal group velocity variation using the co-moving variables results in changes in the pulse length  $L = c\tau_L$ , meaning changes of the shape of the laser pulse envelope. Here  $\tau_L$  is the laser pulse duration in vacuum.

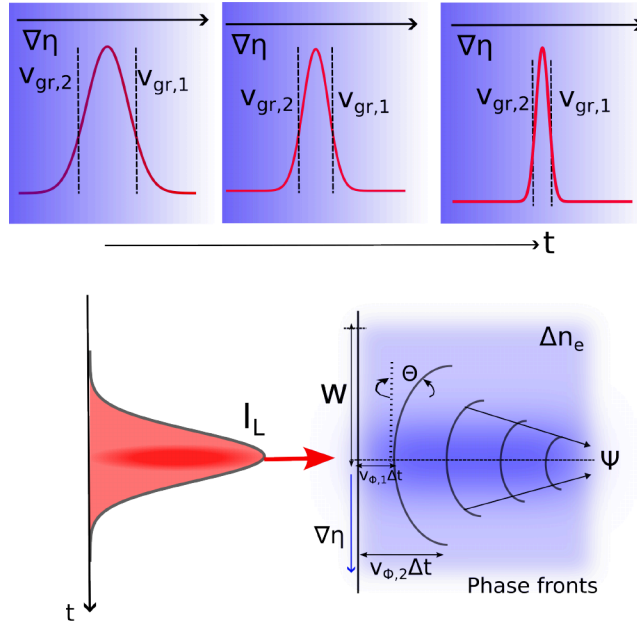


Figure 2.1: The change in the refractive index resulting from relativistic laser intensities triggers nonlinear effects. **[Top]** The presence of a density gradient in the direction of laser propagation leads to a disparity in the group velocity between the leading edge ( $v_{gr,1}$ ) and the trailing edge ( $v_{gr,2}$ ) of the incident laser pulse. As the laser pulse traverses the in-homogeneous plasma, it undergoes temporal compression, resulting in a temporally compressed output laser pulse. **[Bottom]** Considering a Gaussian-like laser intensity profile (depicted in red), it becomes apparent that the refractive index is higher on-axis (illustrated in dark blue), progressively diminishing as one transitions in the transverse direction (illustrated in light blue). This fluctuation in the index brings about a radially adjusted index of refraction,  $\Delta n_e$ . Consequently, the outer segment of the pulse's phase velocity ( $v_{\phi,2}$ ) outpaces the inner segment's ( $v_{\phi,1}$ ), yielding a curvature in the phase front and initiating relativistic self-focusing.

**The transverse and longitudinal changes in  $v_{ph}$**  Variations in the phase velocity along the longitudinal direction lead to a frequency shift in the laser pulse, a phenomenon known as "self phase modulation" or "photon acceleration". In contrast, changes in the phase velocity in the transverse direction induce a curvature in the wavefront, resulting in either "self-focusing" or "de-focusing". as shown in figure 2.1 [Bottom] and is described by [29] as,

$$\frac{1}{\lambda_L} \frac{\partial \lambda_L}{\partial \tau} = -\frac{1}{c} \frac{\partial v_{ph}}{\partial \psi} \quad (2.16)$$

This implies that when longitudinal variations in the phase velocity are introduced using the co-moving variable, they prompt the grouping of wavefronts, resulting in

changes in the laser spectrum. Such local frequency changes necessitate corresponding longitudinal adjustments in the refractive index, denoted as  $\eta$ , thereby leading to photon acceleration (Eq. 2.16) and pulse compression (Eq. 2.15). These dual effects occur simultaneously, as the pulse's spectrum and its duration are connected through Fourier transformation.

On a transverse plane, the modulation of the refractive index yields a consequential alteration in the phase velocity. This leads to the phenomenon of relativistic self-focusing. This self-focusing effect (Fig. 2.1 [Bottom]) is enabled by the establishment of a radially decreasing intensity profile within the focused laser beam, subsequently shaping the necessary refractive index profile for the self-focusing phenomenon. Let us assume two phase velocity components  $v_{\phi,1}$  and  $v_{\phi,2}$ . The first is located on the laser axis and the second is at the edge of the beam profile at a transverse distance 'w' from the laser axis. For  $v_{\phi,1} \neq v_{\phi,2}$ , the phase fronts are curved and the transverse laser energy will be focused inwards ( $v_{\phi,1} < v_{\phi,2}$ ) or defocused outwards ( $v_{\phi,1} > v_{\phi,2}$ ) which is equal to the change in the laser spot size  $\delta w$  given by [29],

$$\frac{\partial^2 w}{\partial \tau^2} = -c \left( \frac{v_{\phi,1} - v_{\phi,2}}{w} \right) \quad (2.17)$$

Equation 2.17 characterizes the acceleration of the laser spot size, denoted as w, arising from the transverse modulation in the phase velocity. Moreover, a diminished electron density at the axis can also originate from the ponderomotive force, which propels electrons away from high-intensity regions (details in section 2.3). This supplementary transverse variation in the refractive index yields analogous outcomes and is termed "ponderomotive self-focusing". The counteracting influence of natural diffraction acts against relativistic self-focusing, resulting in the enlargement of the laser spot size. When an equilibrium between both effects is attained throughout the laser-plasma interaction, the phenomenon of self-guiding occurs. To deduce the laser-power threshold condition,  $P_L$ , for self-focusing one can consider the diffraction of the laser beam and claim that the natural diffraction is balanced with relativistic self-focusing [34, 47, 49, 50] leading to,

$$P_L > P_c = 8\pi\epsilon_0 \frac{m_e^2 c^5 \omega_L^2}{e^2 \omega_p^2} \approx \frac{n_c}{n_e} .17.5\text{GW} \quad (2.18)$$

For a laser of power  $P_L = 100$  TW at a center wavelength of  $\lambda_L = 810$  nm, an electron density of  $n_e > 10^{18} \text{cm}^{-3}$  is required to fulfil the self-focusing condition which leads to the guiding effect for the high-intensity laser pulse.

## 2.3 Plasma based electron acceleration using high-power lasers

The preceding sections of this chapter have discussed both linear and non-linear laser pulse propagation within a plasma generated from a gaseous target. These discussions have highlighted how non-linear effects influence various parameters of the laser pulse.

To comprehend the mechanism through which such laser-plasma interactions can propel electrons to relativistic energies, it becomes imperative to investigate the behavior of the plasma when subjected to the propagation of an ultra-high-intensity laser pulse. This necessitates an examination of the interaction between a laser pulse and a single electron. It's noteworthy that this investigation will conclude that, under ideal circumstances, electron acceleration cannot be achieved using laser fields.

Subsequently, the focal point will shift towards the physical forces that lead to perturbations in electron density within the plasma, ultimately driving the generation of a "wakefield."

Lastly, in the context of the experiments done in this thesis, the most relevant acceleration regimes will be discussed. These discussions will offer a comprehensive overview of the crucial aspects underpinning the electron acceleration mechanisms studied in the thesis.

### 2.3.1 Single electron motion in a laser field

The fundamentals of electron acceleration via relativistic laser-plasma interactions can be described by the motion of a plasma electron in the laser's electromagnetic field. Here the electric field act on a charged particle via the Lorentz force. Using Newton's law one can write equation of motion(e.o.m) as

$$\frac{d\mathbf{p}}{dt} = \mathbf{F}_L(\mathbf{r}, t) = -e[\xi(\mathbf{r}, t) + \mathbf{v}(t) + \mathcal{B}(r, t)] \quad (2.19)$$

Where  $\mathbf{p}(t) = \gamma m_e v(t)$  is the electron's momentum. On the right-hand side, the initial term describes the linear reaction of electrons to the electric field, denoting Direct Laser Acceleration (DLA),  $\xi$ . The subsequent term describes the non-linear reaction attributed to the  $\mathbf{v} \times \mathcal{B}$  force (Ponderomotive laser acceleration). It is worth noting that the force acting on plasma electrons due to the magnetic field is considerably diminished for relativistic electrons, scaled by a factor  $\simeq \mathbf{v}/c = \mathbf{v}_e/c$  for relativistic electrons ( $|\mathbf{v}_e \rightarrow c|$ ). In the context of the simplest scenario involving an infinite plane and a linearly polarized electromagnetic wave, solving Equation 2.19 results in the

well-known **figure-of-8** motion within the co-moving frame and in a drift motion along the laser propagation axis in the corresponding laboratory frame [51].

Nonetheless, analytical computations considering more realistic laser pulse shapes reveal a continuous oscillatory energy exchange between plasma electrons and the electromagnetic field of the laser. This phenomenon is encapsulated in the "Lawson-Woodward theorem" [52, 53]. The theorem states that a single, isolated, relativistic electron does not gain energy from the electro-magnetic laser field if

- the laser pulse propagates in the vacuum with no walls or boundaries present.
- The electron's motion during interaction is highly relativistic ( $|\mathbf{v}_e \rightarrow c|$ )
- no static electric or magnetic fields are present
- The interaction's transverse region is infinite, and
- "ponderomotive effects" are disregarded.

In real-world experimental setups, when an intense ultrashort laser pulse is focused on a gaseous target, one or more of these assumptions are invariably compromised. For instance, the presence of the plasma itself violates point 1, while points 4 and 5 are transgressed due to the laser's tight focusing, which imparts a finite size to the laser spot. Additionally, the interactions trigger the generation of space charge effects and plasma currents, thus violating point 3. The subsequent section will delve into the violation of point 5, where the ponderomotive force exerted by a focused laser pulse results in a net energy exchange between the laser field and the electron.

**The ponderomotive force** To achieve relativistic energies in the order of  $10^{18}\text{W}/\text{cm}^2$ , the laser pulse needs to be intensely focused within a highly confined spatial range, approximately a few wavelengths. As described by Equation 2.7, the amplitude of the normalized vector potential  $a_0$  is substantially higher along the laser axis, thereby leading to the relativistic electron motion. As one moves radially away from the laser axis, the electric field weakens. This gives rise to the phenomenon where electrons are propelled or scattered outward from the laser axis (see Figure 9). This effect is attributed to the weakening restoring force on electrons off-axis in comparison to on-axis. In a simplified description, electrons experience a form of light pressure that expels them from the focal area (depicted in the figure). This phenomenon, marked by the movement of electrons away from the high-intensity region, is termed "ponderomotive scattering" due to the influence of the ponderomotive force [54, 55].

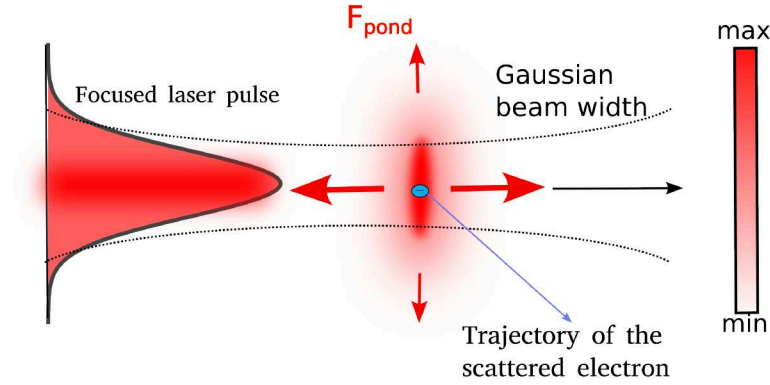


Figure 2.2: Schematics of the ponderomotive force,  $\mathbf{F}_{pond}$  (red arrows) arising from the light pressure which is pushing away the electron on-axis (blue) from the propagation axis (z- axis). The ponderomotive force is directed in the opposite direction to the gradient of the square of the electric field, i.e., the gradient of the laser intensity. The associated electric field within the generated wake is utilized to accelerate the electrons.

$$\mathbf{F}_{pond} = -\frac{e^2}{4\langle\gamma\rangle m_e \omega_L^2} \nabla |\xi_L|^2 \quad (2.20)$$

Which is obtained after time averaging of the Equation 2.19 over the fast laser oscillations [48]. Here  $\langle\gamma\rangle$  is the time averaged  $\gamma$ - factor taking into account the relativistic mass gain  $\gamma m_e$ .

### 2.3.2 Electron acceleration in laser-generated plasma waves

The mechanism to accelerate the electrons using the density modulations within the plasma and the generation of "plasma wave" (also "wakefield") by the interaction of a high intensity laser pulse with an underdense plasma was theoretically proposed by *Tajima and Dawson* [42] in the year 1979. The fundamental principle is that a single, short, high-intensity laser pulse is focused into a gas jet. After the pulse's rising edge has fully ionized the gas (Helium or Hydrogen) the main part of the pulse interacts with an underdense plasma. Figure (2.4) represents the fundamental principle of "laser wakefield acceleration" (LWFA).

**Wakefield generation** Within the central region of the laser pulse, where the intensity and consequently the ponderomotive force are relatively strong, electrons are propelled forward and radially outward from the optical axis (as shown in Figures 2.2 and 2.3). This motion triggers the generation of a space charge field that subsequently exerts an attractive force on the electrons, drawing them back toward the axis. This mechanism excites plasma oscillations at plasma frequency,  $\omega_p$  given by Equation

2.3. This plasma wave having speed close to the speed of light, has a wavelength in practical units given by

$$\lambda_p \simeq \frac{2\pi c}{\omega_p} = \frac{3.34 \times 10^{10}}{\sqrt{(n_e/cm^{-3})}} \mu\text{m}, \quad (2.21)$$

which is determined by the inertia of the electrons. With strong excitation, the plasma wave can break and the electrons are injected in the associated electric field (the wakefield) [47, 56, 57] with which they are accelerated in the forward direction to relativistic energies over distance of only a few millimeters or centimeters [31–33, 58]. According to Poisson’s equation, a non-relativistic approximation of the highest electric field which can be supported by a cold plasma wave can be associated with the limit for wave-breaking and can be written as [44]

$$|\xi_{wb}^*| = \frac{cm_e\omega_p}{e_0}. \quad (2.22)$$

The relativistic generalization reads as

$$|\xi_{wb}| = \sqrt{2(\sqrt{n_e/n_c} - 1)} |\xi_{wb}^*| \quad (2.23)$$

In practical units, Equation 2.23 can be written as [Schnell 37]

$$|\xi_{wb}| = 2.75 \times 10^7 (n_e/cm^{-3})^{-1/4} \text{V/m} \quad (2.24)$$

Consider, for instance, a laser with a wavelength of 800 nm and an electron density of  $n_e = 10^{18} \text{cm}^{-3}$ . Under non-relativistic conditions, the wave-breaking threshold is determined as  $|\xi_{wb}^*| \simeq 0.1 \text{TV/m}$ , while under relativistic conditions, the limit becomes  $|\xi_{wb}| \simeq 1 \text{TV/m}$ . An evident advantage: plasmas are capable of accommodating substantially elevated electric fields compared to the accelerating electric fields achievable in traditional radio frequency (RF) linear accelerators (linacs). The limitation in linacs is restricted to  $\simeq 100 \text{ MV/m}$  due to potential material breakdown occurring along the walls of the accelerating structure.

**Electron injection** To use the electric field inside the plasma wave for electron acceleration, electron must be injected into the wave. Since the velocity of the plasma wave is similar to the group velocity of the laser pulse ( $c$ ) electrons can be injected externally if they have significant velocity. In order to achieve minimal emittance, the electrons should be injected with sufficient initial momentum into a spatial volume

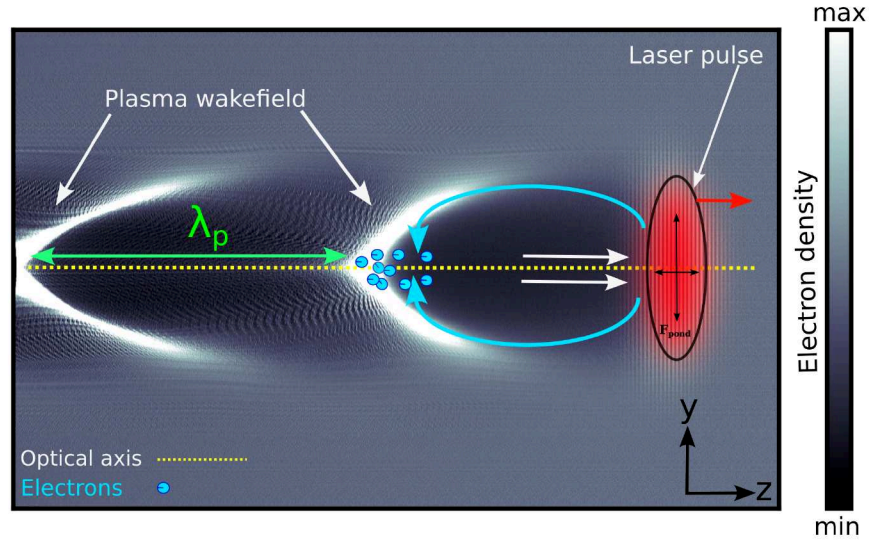


Figure 2.3: Mechanism of electron acceleration in the laser wakefield regime. The laser pulse travels along the z-axis (optical axis) from left to right. The ponderomotive force (indicated by black double arrows and linked to the laser pulse's intensity gradient, depicted in red shading) drives electrons away from the optical axis and triggers the initiation of a plasma wave characterized by a plasma wavelength  $\lambda_p$ . With a strong excitation, this plasma wave can break causing electrons (light blue circles) to be injected and subsequently accelerated in forward direction via strong longitudinal electric field.

that is matched to the beam charge and background density. This is difficult to achieve with an external electron source (RF), because it requires matching a beam from the RF injector with structure scales of centimeters to the plasma accelerator with 10's of  $\mu\text{m}$ . External injections was first proposed in 1993 [59] in low density plasma with long wavelength and later in 2006 with using a colliding second laser pulse creating a beat-wave inside the plasma [60, 61]. Electrons can also be completely self-injected via the process of wave-breaking. Here the velocity of the electrons forming the plasma wave reaches the phase velocity of the wave itself (Fig. 2.3). These electrons are self-injected into the wakefield and accelerated in the forward direction. Experimentally, self-injection this is the most straightforward approach to generate relativistic electrons. However, due to the expansion of the cavity size during the self-focusing of the drive laser, the phase velocity of the first wakefield peak slows down and allows electrons to be trapped more easily over a considerable distance leading to a large momentum spread. To avoid the appearance of an energy spread and in order to achieve quasi-monoenergetic electron bunches it is extremely important to spatially separate the electron injection and acceleration process [38, 62].

**Ionization injection** Another way of injection relies on "creating" electrons in already trapped orbits. Ionization injection uses the fact that different charge states of an atom are ionized at different electric field strengths. To calculate approximate ionization rates, models such as Ammosov-Delone-Krainov (ADK) [63] is used. Hydrogen or Helium already ionize before  $a_0 \sim 0.03$ , which is reached already in the rising edge of the main pulse. the same can be said for Nitrogen until 5th level. The ionization potential for the levels 6 and 7 requires much higher intensities ( $a_0 = 1.8$  or  $a_0 = 2.3$ ). A small percentage of a gas with medium Z (here: Nitrogen) is added to the Helium or Hydrogen gas target. Hence, these electrons are "born" right inside of the plasma wave and can be trapped [64]. Although its simple implementation and high charge output, ionization injection yields broad spectra because : a) Injection is continuous, as long as the trapping condition is fulfilled, and b) Tunnel ionization smears out the ionization threshold.

Atom	Level	IP(eV)	I (W/cm <sup>-3</sup> )	$a_0$
H	1	13.6	$2.2 \times 10^{14}$	0.01
He	1	24.6	$1.7 \times 10^{15}$	0.03
	2	54.4	$1.0 \times 10^{16}$	0.07
N	1	14.5	$2.8 \times 10^{14}$	0.01
	2	29.6	$1.2 \times 10^{15}$	0.02
	3	47.5	$3.3 \times 10^{15}$	0.04
	4	77.5	$1.2 \times 10^{16}$	0.08
	5	97.9	$2.0 \times 10^{16}$	0.1
	6	552	$1.8 \times 10^{18}$	1.8
	7	667	$2.3 \times 10^{18}$	2.3

Table 2.1: The ionization potential(IP) for Hydrogen, Helium and Nitrogen gases used for experiment during this thesis. Last two columns give intensity and corresponding  $a_0$  which causes an ionization rate of 0.5/fs as predicted by ADK model with  $\lambda = 800\text{nm}$ .

**Injection in density transitions** The limitations of self-injection can be mitigated by shaping the longitudinal plasma density profile. This injection, called down-ramp-injection, has a longitudinally decreasing plasma density which leads to a continuous increase of the plasma wavelength ( $\lambda_p \propto n_e^{-1/2}$ ). Effectively, this lowers the phase velocity of the back of the bubble and enables electrons to be trapped longitudinally. While the slow downward density transition can trap many electrons, it has two major drawbacks. First, the prolonged injection process will lead to a large energy spread, and b) the permanent increase in the plasma wavelength causes quick dephasing of the electron bunch, as it reaches the front part of the oscillating plasma only after a

short propagation distance.

To overcome this a sharp density down-ramp profile could be used where the change in plasma density occurs over a length shorter than the plasma wavelength. Here the density changes rapidly from  $n_{e,1}$  to  $n_{e,2}$  with  $n_{e,1} = \alpha n_{e,2}$  and  $\alpha \gtrsim 1$ . the relative change in plasma wavelength is calculated as [65, 66],

$$\frac{\Delta\lambda_p}{\lambda_p} = \frac{\lambda_{p,1} - \lambda_{p,2}}{\lambda_{p,1}} = \sqrt{\frac{n_{e,1}}{n_{e,2}}} \approx \frac{1}{2}(\alpha - 1) \quad (2.25)$$

And at the same time, the phase velocity can be described as

$$\frac{\Delta v_p}{v_p} = \frac{v_{g,2} - v_{g,1}}{v_{g,1}} \approx \left(1 - \frac{n_{e,2}}{2n_c}\right) \left(1 + \frac{n_{e,1}}{2n_c}\right) \approx \frac{n_{e,2}}{2n_c}(\alpha - 1) \quad (2.26)$$

These two equations shows that the change in plasma wavelength is much greater than the change in phase velocity of the for the typical underdense plasma used in the experiments. The phase velocity of the plasma wave is basically frozen during the rapid increase in the  $\lambda_p$  and the wave is instantly loaded with many electrons. These electrons are located at a similar phase of the wake with similar initial energy, exposing them to the same accelerating field. Therefore they will gain similar energy resulting in a quasi-monoenergetic beam. This mechanism was first proposed numerically in [65, 66] and was experimentally verified to produce monoenergetic electron bunches [5, 67]. In this thesis, the gas density profile from a supersonic gas nozzle was modified by a razor blade creating a narrow shock-front with the desired drop in the density profile [68, 69].

### 2.3.3 Laser wakefield acceleration in the blow-out regime

The most efficient mechanism to induce a plasma wave obtained with tightly focused, high-intensity laser pulses ( $a_0 \geq 2$ ) and pulse duration short enough to match half a plasma length  $c\tau_L \simeq \lambda_p/2 = \pi c/\omega_p$  is addressed in the so-called "blow-out" regime. According to Equation 2.21, for an electron density of  $n_e \geq 10^{18} \text{cm}^{-3}$  the plasma period is  $\lambda_p \leq 30 \mu\text{m}$  and the aforementioned condition can be fulfilled with pulse duration on the order of  $\tau_p \leq 56 \text{fs}$ . The highly non-linear broken wave regime, also called "blowout" acceleration regime, was explained in 2002 by *Pukhov and Meyer-ter-Vehn* in 2002 using computer simulations [70]. The main features of the blow-out regime are:

- A periodic plasma wave free from cold plasma electrons is formed behind the driving laser pulse (Fig :2.3).

- The electrons are pushed both in longitudinal and transverse directions and stream around the generated cavity with a chance of getting self-trapped in the ion-cavity. Here the longitudinal electric field inside the plasma wave structure is strong enough ( Equation 2.23) to accelerate the electrons in the forward direction up to the relativistic energies.
- The laser pulse propagates several Rayleigh lengths within the plasma without significant defocusing.

One special case of the blow-out regime is the "bubble" regime where the cavity generated by the laser pulse is assumed to be spherical in shape having radius  $r_{bub} = 2\sqrt{a_0}/k_p$ , where  $r_{bub}$  is the radius of the sphere assumed. "Bubble" acceleration has been developed through phenomenological laws via extensive analytical and simulation studies [71, 72]. It was described theoretically by [73] and the optimized conditions to generate quasi-monoenergetic electrons can be approximated. In the following discussion, simple scalings will be addressed to reach the bubble acceleration regime where quasi-monoenergetic electrons can be produced. Here, the parametric dependencies were determined from the analytical theory while the numerical pre-factors have been determined from three-dimensional particle-in-cell (PIC) simulations [73]. The threshold for the laser focus spot radius,  $w_0$ , pulse duration,  $\tau_L$ , and laser power,  $P_L$ , to create an efficient acceleration of the electron bunches are,

$$\frac{\omega_p}{c} w_0 \simeq \sqrt{a_0}, \quad \tau_L \lesssim \frac{w_0}{c} \quad (2.27)$$

and

$$P_L \gtrsim P_{bub} = P_{rel}(\omega_L \tau_L)^2 \simeq \left( \frac{\tau_L/\text{fs}}{\lambda_L/\mu\text{m}} \right)^2 \cdot 31 \text{ GW} \quad (2.28)$$

Here,  $P_{rel} = 4\pi\epsilon_0 m_e^2 c^5 \simeq 8.7\text{GW}$  is the natural relativistic power unit. The scaling for the maximum achievable peak energy of the quasi-monoenergetic electrons and the number of particles contained in such electron bunch can be approximated as,

$$E_{mono} \simeq 0.65 m_e c^2 \sqrt{\frac{P_L}{P_{rel}} \frac{c\tau_L}{\lambda_L}} = \sqrt{\frac{P_L}{P_{rel}} \frac{\tau_L/\text{fs}}{\lambda_L/\mu\text{m}}} \cdot 0.1 \text{ MeV} \quad (2.29)$$

and

$$N_{mono} = \sqrt{\frac{P_L}{P_{rel}}} (\lambda_L/\mu\text{m}) \times 10^{18} \text{ particle number} \quad (2.30)$$

According to the scalings in Equation 2.29 and 2.30, it was shown in 3D-PIC simulations that the laser energy conversion efficiency into such an accelerated electron bunch is constant and on the order of [73]

$$\kappa = \frac{N_{mono}(E_{mono}/\text{MeV})}{(P_L/\text{TW})(\tau_L/\text{fs})} \lesssim 20\% \quad (2.31)$$

which is very promising for the future applications.

### Limitations on energy gains

The main limitations for LWFA are three "detrimental Ds": Diffraction, Dephasing and Depletion. We will discuss them here briefly.

**Laser diffraction** In any focused beam, diffraction will reduce the laser intensity after a certain distance but self-focusing may balance this over many Rayleigh lengths. Outside the Rayleigh range the laser spot grows quickly, which reduces the intensity. The Rayleigh length is given as,  $z_0 = \frac{\pi w_0^2}{\lambda_L}$  where  $z_0$  is the Rayleigh length and  $w_0$  denotes the waist of the laser pulse. For Ti:Sa laser system used in this work, a beam waist of  $25\mu\text{m}$  gives Rayleigh length of around 2.5 mm , i.e. in the order of the acceleration length.

**Electron dephasing** The trapped electrons in the plasma can be accelerated arbitrarily close to the speed of light ( $v_e \approx c$ ), whereas the plasma wave propagates with the laser group velocity ( $v_g = \eta c < c$ ) . Hence, after a certain length  $L_{dph}$  the electrons overtakes the plasma wave and move to a region of decelerating fields. In other words, it loses energy by being decelerated as the electric fields reverse at the rising edge of the plasma wave. This process is called dephasing and the dephasing length is denoted by  $L_{deph}$ . In the 1D linear regime, dephasing length is given as

$$L_{deph} = \lambda_p \frac{n_c}{n_e} \propto n_e^{-\frac{3}{2}} \quad (2.32)$$

The dephasing length for a 3D bubble regime is given by [74, 75],

$$L_{deph} = \frac{4}{3} \frac{\omega_L^2}{\omega_p^2} \frac{\sqrt{a_0}}{k_p} \propto \sqrt{a_0} n_e^{-\frac{3}{2}} \quad (2.33)$$

For typical electron densities of  $\approx 5 \times 10^{18} \text{cm}^{-3}$  and  $a_0 = 2$ , the dephasing length is usually  $L_{deph} \sim 3 - 4 \text{mm}$ .

**Pump depletion** As the laser pulse propagates through the plasma, it slowly loses energy through diffraction and driving the wake. The energy loss is concentrated at the front of the laser pulse that is interacting with the medium and slowly etches away at a velocity  $v_{etch}$  [74, 75]

$$v_{etch} \simeq c \frac{\omega_p^2}{\omega_L^2} \quad (2.34)$$

This means that after a certain distance, the pump-depletion length  $L_{pd}$ , the pulse is not intense enough to drive the plasma wake and the cavity hence collapses. The depletion length in 3D bubble regime is given as ,

$$L_{pd} = \frac{c}{v_{etch}} c\tau \propto \frac{\omega_L^2}{\omega_p^2} c\tau \propto \frac{1}{n_e} \quad (2.35)$$

Higher plasma densities lead to faster etching of the pulse and shortens the depletion length, whilst reducing the density allows sustaining the accelerating structure over longer distances.

**Beam loading** For all the above cases, only single test electrons in the plasma fields have been considered. A highly charged bunch, however, will modify ("beam load") the electric field of the plasma wave., and therefore the acceleration process. Generally, the electrons that are accelerated in the plasma wave will be out-of- phase with the electrons constituting the plasma wave. Thus their electric field will counteract the fields of the plasma wave and damp the accelerating field. Typically, a beam loaded wakefield will manifest itself in a decrease in energy gain and a modified energy spread [76].

## 2.4 Numerical 2D PIC simulations

The study of laser wakefield acceleration involves a multitude of experimental parameters, many of which can be comprehended and determined using the 1D equations and scaling laws outlined in the preceding sections 2. However, achieving a comprehensive understanding of the entire process is a challenging task, and several parameters remain experimentally inaccessible, at least for the time being. Consequently, the investigation of laser wakefield acceleration heavily relies on computational simulations, particularly those conducted using a technique known as *Particle-in-Cell* (PIC) simulations [77–79].

A PIC simulation can be divided into two primary components. The first component deals with the electric ( $\mathbf{E}$ ) and magnetic ( $\mathbf{B}$ ) fields, which are represented by their values on a predefined grid within the simulation box. These fields are dynamic and evolve over time, and their temporal evolution is determined by solving Maxwell's equations numerically:

$$\frac{\partial \mathbf{B}}{\partial t} = -\nabla \times \mathbf{E} \quad \mu_0 \epsilon_0 \frac{\partial \mathbf{E}}{\partial t} = \nabla \times \mathbf{B} - \mu_0 \mathbf{J} \quad (2.36)$$

In a PIC simulation, these fields are calculated at each time step, taking into account the motion and interactions of the charged macro-particles within the simulation. This dynamic calculation allows the simulation to capture the complex interplay between electromagnetic fields and charged particles as the simulation progresses in time.

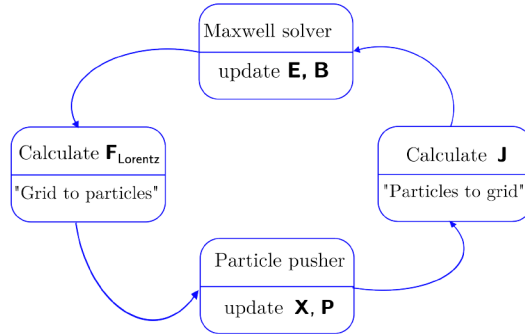


Figure 2.4: The PIC workflow: After advancing  $\mathbf{E}$  and  $\mathbf{B}$  fields, the Lorentz force ( $\mathbf{F}_{Lorentz}$ ) is calculated for every particle within the simulation. With these forces, all particle momenta  $\mathbf{P}$  and respectively the particle positions  $\mathbf{X}$  are updated. The moving charge  $\mathbf{J}$  creates a current on the simulation grid, which is inserted into Maxwell's equation during the next iteration. The cycle continues to evaluate the system of electromagnetic fields and particles. Adapted from [80]

The second component employ discrete macro-particles that are initially placed on a grid, typically with one macro-particle per cell. Each macro-particle represents a specific number of electrons, typically ranging from  $10^6$  to  $10^7$  electrons, and thus carries a designated charge and mass corresponding to this electron count. Also, since the position and the momentum of every single particle is known, all required quantities (like plasma density, charge density, current, temperature, etc.) can be calculated from macro-particles. The particle trajectories are calculated independently by solving each individual equation of motion [80, 81] :

$$\frac{d\mathbf{x}}{dt} = \mathbf{v} \quad \frac{d\mathbf{p}}{dt} = \mathbf{F}_{Lorentz} = q(\mathbf{v} \times \mathbf{B}) + q\mathbf{E} \quad (2.37)$$

The movement of the charged particles results in the generation of an electric current density,  $\mathbf{J}$ . This current density is calculated on the computational grid, taking into account the positions, velocities, and charges of the macro-particles within the simulation. The current density is then used as a source term in Equation 2.36, to upgrade the electromagnetic fields ( $\mathbf{E}$  and  $\mathbf{B}$ ) on the grid for the next time step. This process is iterative and repeated for each time step, allowing the simulation to evolve

over time as the particles move and interact with the electromagnetic fields (Fig: 2.4).

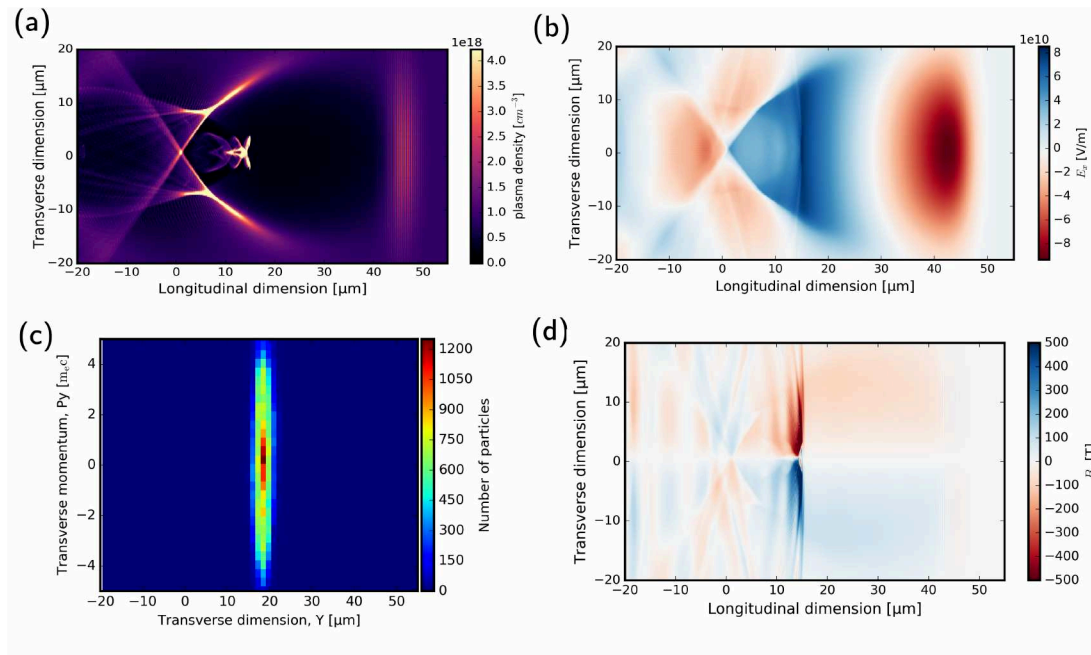


Figure 2.5: A single frame from a Particle-in-Cell (PIC) simulation during the interaction phase. The laser pulse is propagating from left to right. The entire simulation box has dimensions of 80  $\mu\text{m}$  in both the longitudinal and transverse directions. (a) Electron bunch is being injected into first plasma oscillation. (b) The longitudinal electric field co-propagating with the laser pulse and providing the necessary field to accelerate electrons up to relativistic energies.(c) The transverse phase space histogram of the electrons trapped in the first plasma oscillation giving the information about the symmetry of the injection of the electrons.(d) The Azimuthal magnetic field of the accelerated electron bunch, which could be used to detect the electron bunch via the Faraday effect [82]

Figure 2.5 captures a snapshot from a characteristic laser wakefield simulation. At this stage, the laser pulse has penetrated the plasma, reaching a depth of several hundred microns, and has triggered the development of a nonlinear plasma wave. During this time frame, electrons have been introduced into the initial oscillation, with a few electrons also evident in the subsequent oscillation. These electrons are presently experiencing the influence of a potent longitudinal electric field. Notably, the accelerated electrons contribute to the generation of a substantial azimuthal magnetic field. The valuable information about the phase space of the injected electrons can also be obtained from these simulations as shown in fig: 2.5. The visualization of transverse momentum and thus the phase space will give us insights into the asymmetric injection of the electrons using shock-front injection mechanism as presented in the chapter 5.

PIC simulations serve as a valuable tool for gaining insights into the fundamental processes of laser wakefield acceleration, especially when experimental measurements of critical parameters are limited. Naturally, the accuracy of these simulations increases with smaller individual cell sizes (corresponding to fewer particles per macro-particle) and larger total simulation box sizes. However, the choice of simulation parameters always involves a trade-off between achieving higher resolution and the computational resources available.

One notable challenge is the inherent limitation in capturing Coulomb explosion forces accurately because electrons within a single macro-particle cannot interact with each other.

## 2.5 Secondary "betatron" radiation generation

Laser-plasma based electron accelerators, described in section 2.3, are of great importance for realizing table-top sources of relativistic electron bunches for practical applications [83]. In this section, the subsequent generation of spatially and temporally coherent hard X-ray pulses in the femtosecond-time domain will be discussed. It is a basic physical principle that accelerating charges emit radiation. This radiation can be calculated from a solution to Maxwell's equations called Lienard-Wiechert fields, provided that the equation of motion of the accelerating charge is known [84]. Along with the longitudinal acceleration of the electrons to the relativistic energies, the electrons also undergo a transverse oscillation due to transverse electromagnetic fields, which leads to the emission of the X-ray radiation. In general, photon emission from radially accelerated electrons is referred to as synchrotron radiation which was first discovered in 1946 as "*Radiation from Electrons in a Synchrotron*" [85]. Of large interest are broadband femtosecond X-ray pulses that provide new opportunities for time-resolved X-ray absorption spectroscopy [86]. Due to its  $\simeq 1\mu\text{m}$  source size, it has been also sought after for phase contrast imaging techniques [40, 87, 88]. There are variety of keV X-ray generation methods based on laser-plasma interactions, including high order harmonics from gas or solid targets [27, 89, 90], sources based on the flying mirror technique [91] or  $K_\alpha$  sources [92] to name only a few. A more promising and compact approach for generating X-rays using emission from accelerated electrons via the relativistic laser and underdense plasma interaction is to induce a wiggling motion of the relativistic accelerated electrons with one of the following mechanisms.

- A conventional meter-scaled undulator consisting of a magnetic structure like in a synchrotron [93, 94].

- An electromagnetic wave undulator where the electrons oscillate in the laser field itself and emit femtosecond X-ray and gamma ray beams [95, 96].
- Or within the plasma itself, which is the simplest approach. Here the strong localized electric and magnetic fields inside the plasma are used to accelerate and wiggle the electrons and causes them to produce hard X-ray radiation as shown in figure [97, 98].

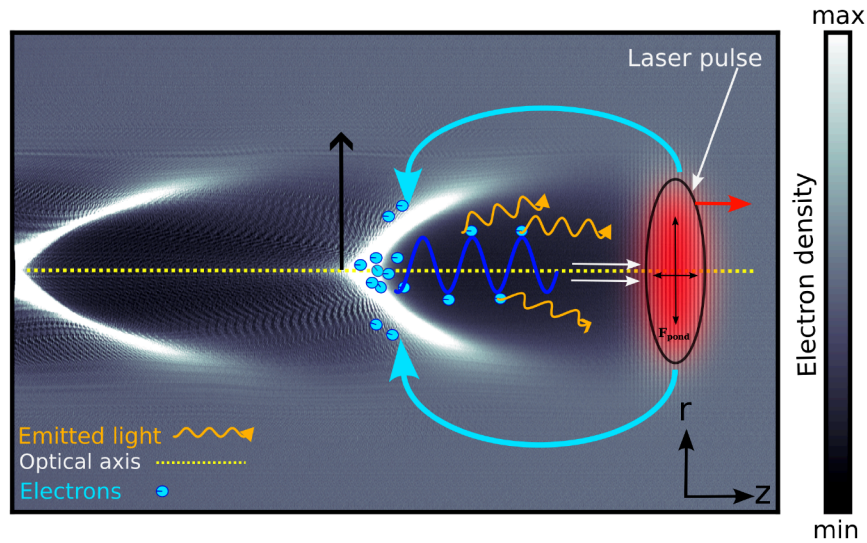


Figure 2.6: Mechanism of the betatron oscillation from relativistic oscillating electrons. A transverse electric field associated with the charge separation in the plasma wave forces the highly relativistic electrons to oscillate transversely (blue oscillation), leading to the emission of the betatron radiation in the X-ray regime in the forward direction with a finite divergence (orange emitted light is shown in the lab frame). The electron injection and acceleration is similar to Figure 2.3, but occurs together with transverse electron oscillation around the optical axis

The first successful experiments in a conventional undulator driven by a wakefield accelerated electrons resulted in spatially coherent soft X-rays up to an energy of 130 eV [93, 94]. The measured radiation was spatially and temporally confined in a 10 fs pulse having an angular distribution of only 2 mrad. However, an extension towards a shorter wavelength require more energetic electrons and/or a shorter undulator period. The later approach is known as "non-linear Thomson scattering" and "Thomson back-scattering" where the electrons oscillate in an electromagnetic wave and emit femtosecond X-rays and gamma rays. Here the shorter undulator period can be realised with the laser itself. In Thomson back-scattering, the electron is wiggled in a counter

propagating laser field [95, 96] and emitted X-ray energy scales with the square of the electron energy up to MeV energy range. Finally, the plasma itself can be employed as a wiggler for the accelerated electrons [97, 98] as shown in figure 2.4. Here the electrons oscillate with the so-called "betatron frequency", thus this kind of synchrotron radiation is called "**betatron radiation**". In the literature, there are many instances where the terms synchrotron radiation and betatron radiation have been used interchangeably. to be consistent with this thesis, the name betatron radiation is used for the X-rays generated from the laser plasma acceleration. this is the physical principle behind the experimental work done in this thesis and therefore will be discussed in detail in the following sections. The formulae would be derived for the simple model of a single-moving electron and the scalings are, strictly speaking, only valid for time constant parameters (will be explained in following sections), meaning for electrons without acceleration. However, due to the strong dependence of the X-ray spectrum on the electron properties, the largest number of the X-ray photons is emitted from the region in the plasma where the electrons have their maximum energy [39, 99], i.e., within the last betatron oscillation around the dephasing time. therefore, the formulas and scalings, derived for constant parameters can be used as a good approximation of the realistic case of the accelerated electrons by using the values at the dephasing time. *Corde et al.* [97] gives a comprehensive overview for femtosecond X-ray generation from laser-plasma accelerators.

### 2.5.1 Electron orbit within the laser wakefield

Apart from the longitudinal electric field and an azimuthal magnetic field, there exists a transverse electric field associated with a radial charge separation in the plasma wave. In the bubble regime, this transverse electric field can be written in the practical units as [47],

$$|\xi_{trans}| \simeq 9.06 \times 10^{-15} (n_e/cm^{-3})(r_s/\mu m) MV/m, \quad (2.38)$$

Where the ion cavity is described as the radius of sphere  $r_s$ . In a cylindrical coordinate system  $r$  is the transverse distance from the laser propagation axis.  $r = 0$  corresponds to the laser axis, where the ion cavity is centered and the transverse field is zero. One of the major advantage of the plasmas is that it can produce really high Gauss fields and have a much shorter effective wiggler period on the order of few hundreds of microns [39], resulting in a low divergence beam of X-rays even for electrons in the 100MeV range. The physical principle of the laser-plasma based betatron radiation

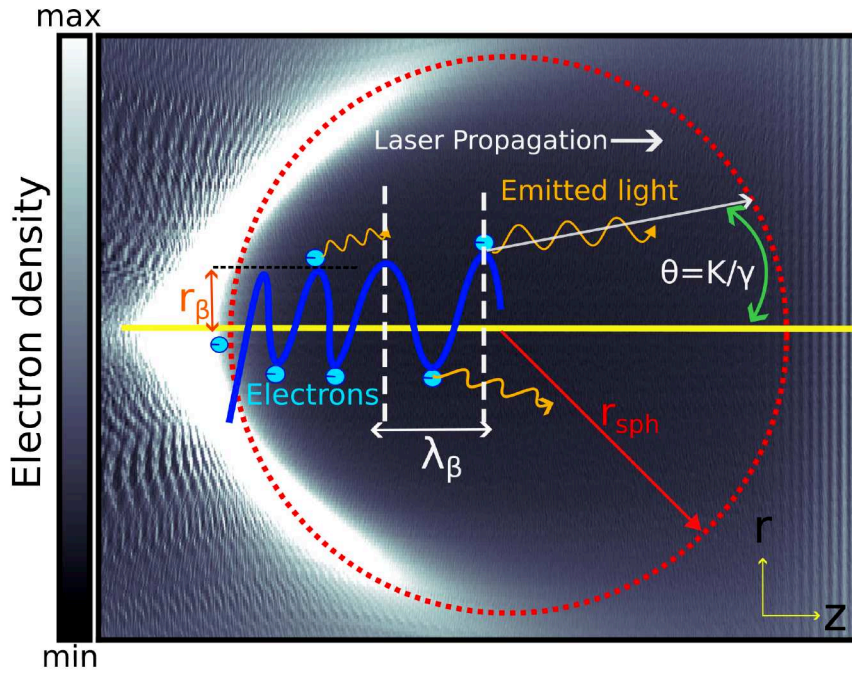


Figure 2.7: Parameters for betatron radiation from the relativistic oscillating electrons. The electrons oscillate (blue oscillations) with the betatron amplitude,  $r_\beta$ , and wavelength,  $\lambda_\beta$ . Here, the ion-cavity is described by a sphere of radius  $r_{sph}$  (red dashed circle). Light blue circles show the radiation point where the electrons radiate light in the forward direction in a cone of divergence characterized by  $\theta$  (orange emitted light is shown in the lab frame).

was first proposed by *Kieslev et al.* [100] in 2004 and was experimentally demonstrated by *Rousse et al.* [97].

## 2.5.2 Radiation fundamentals

As described in previous section, the radial space charge field will force the highly relativistic electrons to perform a transverse oscillation with the betatron wavelength [98] written in the co-moving frame as

$$\lambda_\beta = \sqrt{2\gamma}\lambda_p \simeq 4.72 \times 10^{10} \sqrt{\frac{\gamma}{n_e/cm^{-3}}} \mu\text{m}. \quad (2.39)$$

This leads to the emission of the betatron radiation as shown in figure 2.7, whose characteristics are similar to the synchrotron radiation in the wiggler regime [88] at the fundamental wavelength of

$$\lambda_0 = \frac{\lambda_\beta}{2\gamma^2} \simeq 2.36 \times 10^{10} \sqrt{\frac{1}{\gamma^3(n_e/cm^{-3})}} \mu\text{m}. \quad (2.40)$$

The fundamental wavelength is comparable to the betatron wavelength,  $\lambda_\beta$ , Doppler shifted in the laboratory frame. The ion-cavity acts as a plasma undulator with a period according to the Equation 2.39 and a betatron strength parameter written in practical units as,

$$\mathcal{K} = \gamma\theta \simeq 1.33 \times 10^{-10} \sqrt{\gamma(n_e/cm^{-3})}(r_\beta/\mu m), \quad (2.41)$$

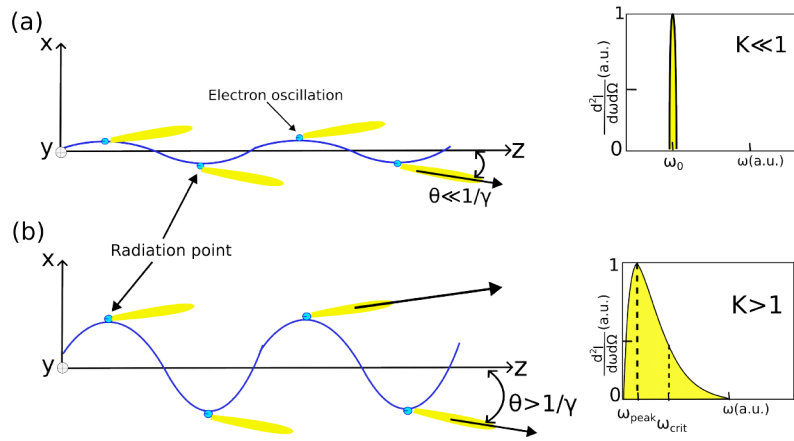


Figure 2.8: Schematic of the undulator and the wiggler regimes at the top and bottom of the figure, respectively. a) In the undulator regime the oscillation amplitude of the electrons is much smaller than in the wiggler limit, and the on-axis spectra is characterized by its fundamental frequency,  $\omega_0$  (Equation 2.40). b) For  $\mathcal{K} > 1$  (wiggler regime) the radiated spectrum is a broad-band continuum characterized by its critical frequency,  $\omega_{crit}$  (Equation 2.44).

Where  $\theta$  is the half angle of divergence and  $r_\beta$  is the betatron amplitude of the electron trajectory (Figure 2.8). This oscillation of the relativistic electron is similar to that of an electron oscillating in a conventional oscillator or in a wiggler of a synchrotron. Therefore, the characteristic values like the electron period (Eq: 2.39) or the strength parameter (Eq: 2.41), which are commonly used in synchrotron and FEL ("Free electron laser") community are also used here.. consequently, the radiation is emitted in forward direction in a narrow cone of divergence given by  $\theta = \frac{\mathcal{K}}{\gamma}$  and can be characterised by the amplitude of the strength parameter,  $\mathcal{K}$ , as [98]

$$\mathcal{K} \begin{cases} \ll 1 & \text{Undulator regime, emission at the fundamental frequency } \omega_0. \\ \simeq 1 & \text{Intermediate regime, emission at several harmonics.} \\ > 1 & \text{Wiggler regime, emission of a broadband continuum.} \end{cases}$$

Figure (2.7 2.8 a) shows that for the undulator regime, the electron motion remains near the axis with a weak oscillation amplitude and the radiation is emitted at the fundamental frequency according to the equation 2.40 in the forward direction ( $\theta \rightarrow 0$ ). Increasing the electron oscillation amplitude also increases the strength parameter to  $\mathcal{K} \simeq 1$  and several harmonics starts to appear. Going further,  $\mathcal{K} > 1$ , one reaches wiggler regime, schematically shown in Figure 2.8(b), where the electron oscillation amplitude is much higher compared to the undulator regime and many closely spaced high harmonics are radiated in a broad-band continuum. For laser-plasma based betatron sources operating in the blow-out (or bubble) regime a value of  $\mathcal{K} > 1$  is typically used.

The continuous X-ray radiation centered on the observation direction  $\mathbf{n}$  can be described by the radiated spectrum of a single electron on an arbitrary oscillation  $\mathbf{r}(t)$  [84]

$$\frac{d^2 I}{d\omega d\Omega} = \frac{e^2}{16\pi^3 \epsilon_0 c} \left| \int_{-\infty}^{+\infty} \exp\left[-i\omega\left(t - \mathbf{n} \frac{\mathbf{r}(t)}{c}\right)\right] \frac{\mathbf{n} \times [(\mathbf{n} - \boldsymbol{\beta}) \times \dot{\boldsymbol{\beta}}]}{(1 - \boldsymbol{\beta} \cdot \mathbf{n}^2)} dt \right|^2. \quad (2.42)$$

Here  $I$  is the spectral flux emitted into the solid angle  $d\Omega$  within a spectral band  $d\omega$  centered on frequency  $\omega$ . The emitted betatron spectrum depends on (and can be controlled by ) the electron velocity normalized to the speed of light in vacuum,  $\boldsymbol{\beta}$ , and the electron trajectory  $\mathbf{r}(t)$ . For zero electron acceleration,  $\dot{\boldsymbol{\beta}} = 0$ , no radiation is emitted. On the contrary, a maximum flux is reached for  $\boldsymbol{\beta} \cdot \mathbf{n} \rightarrow 1$ , meaning a highly relativistic electron,  $\boldsymbol{\beta} \simeq 1$ , that radiates in the direction of its velocity ( $\boldsymbol{\beta} \parallel \mathbf{n}$ ). For an asymptotic behaviour of the radiated spectrum observed on-axis ( $\theta = 0$ ), Equation 2.42 can be simplified to [35]

$$\left. \frac{d^2 I}{d\omega d\Omega} \right|_{\theta=0} \simeq N_\beta \frac{3e^2}{2\pi^3 \hbar \epsilon_0 c} \gamma^2 \alpha^2 K_{2/3}^2(\alpha), \quad (2.43)$$

Where  $N_\beta$  is the number of oscillations,  $K_{2/3}$  the modified Bessel function of the second kind and  $\alpha = E/E_{crit}$ . Here  $E_{crit} = \hbar\omega_{crit}$  represents the energy, within the distribution, where half of the radiated power is below  $E_{crit}$  and the other half lies above  $E_{crit}$  (Figure 2.8). This critical energy is defined in practical units by,

$$E_{crit} = \hbar\omega_{crit} \simeq 5 \times 10^{-24} \gamma^2 (n_e/\text{cm}^{-3}) (r_\beta/\mu\text{m}) \text{keV}. \quad (2.44)$$

and

$$N_{ph} \propto N_\beta (n_e/\text{cm}^{-3}) \mathcal{K}. \quad (2.45)$$

Where  $N_{\text{ph}}$  is number of photons emitted. According to the Equation 2.43 the radiated X-ray energy extends up to

$$E_{\text{peak}} = \hbar\omega_{\text{peak}} \simeq 1.45 \times 10^{-24} \gamma^2 (n_e / \text{cm}^{-3}) (r_\beta / \mu\text{m}) \text{keV}, \quad (2.46)$$

and drops exponentially down to zero.

In summary, this chapter illustrates how plasma transforms the transverse electric field of a laser into both longitudinal and transverse electric fields within the plasma wave. These fields enable the acceleration of electrons to relativistic energies and induce transverse wiggling with an amplitude denoted as  $r_\beta$ . This complex process results in the emission of betatron radiation characterized by a synchrotron-like energy distribution.

# 3 Experimental Methods and Diagnostics

In anticipation of the forthcoming chapters, this section will provide an introduction to the experimental methods and diagnostics employed in all the experiments detailed in this thesis. The laser plasma accelerator, which comprises the high-power laser system and the gas targets, will be examined. Subsequent sections will delve into the diagnostic techniques applied to the laser-plasma interaction region, encompassing diagnostics for the relativistic electron beams. Furthermore, particular emphasis will be placed on the detection and characterization methods used for the generated X-ray radiation (Figure 3.1).

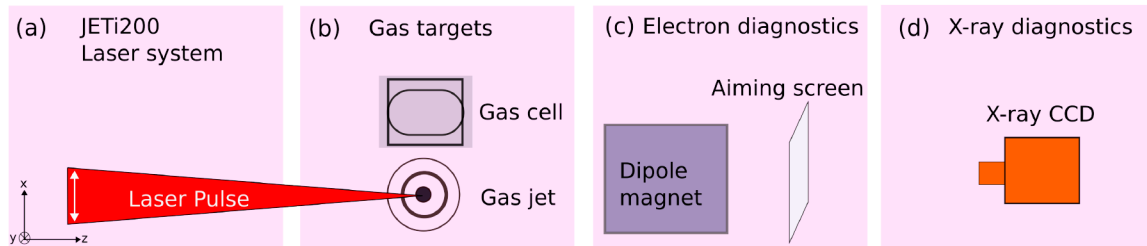


Figure 3.1: Top view of the flow chart for the electron acceleration and the X-rays generation setup followed in this work (light purple). (a) JETi200 laser system, where the double arrow white line indicates the laser polarization direction (Sec. 3.1). (b) The gas targets used during the experimental work in this thesis. The gas jet was used with a commercial razor blade to produce shock. (c) Electron diagnostics (Sec. 3.2) and (d) X-ray diagnostics (Sec. 3.3).

## 3.1 JETi200 Laser system

The Jenaer Titanium:Sapphire 200 Terawatt (JETi200) laser system utilizes a gain medium made of titanium-doped sapphire (Ti:sapphire) and employs passive mode-locking techniques. Titanium-doped sapphire (Ti:Sa) crystals used as the gain medium has a central wavelength of 800 nm and up to 80 nm pulse bandwidth. This system is capable of achieving peak power levels of up to 300 terawatts (TW). The JETi200 laser system employs a technique known as double-chirped pulse amplification (CPA) [23] to achieve high-power laser pulses with exceptional temporal contrast. CPA allows for the

amplification of laser pulses by first temporally stretching them before the amplification process. This stretching reduces the peak power of the pulses to levels below the damage threshold of optical components and amplifying crystals. Simultaneously, it keeps the laser system compact in size. In the final stage of the laser chain, the pulse is then temporally compressed to attain the desired short pulse duration. The JETi200 operating parameters for this work was a peak power of 200TW, 20 fs-short pulses, 5 J on target with 0.2 Hz repetition rate.

A vacuum beam transport line serves as a connection between the JETi200 compressor chamber and the long experimental chamber. To maintain the required vacuum conditions of approximately  $10^{-5}$  mbar during experiments, two turbomolecular pumps are utilized. Additionally, the optical breadboard for the experimental equipment is isolated from the chamber frame to prevent any vibrations caused by the pumps and deformations arising from pressure differences. An f/20 off-axis parabola (OAP) is employed to focus the JETi200 laser beam onto the gas targets. The characteristics of the laser profile and the gas-jet density profile will be elaborated upon in the subsequent sections.

The experimental setup involves introducing a mirror into the laser beam path to redirect the laser pulse towards off-line diagnostic equipment. To attenuate the laser intensity and protect sensitive equipment like cameras from damage, the laser pulse is reflected multiple times off uncoated, high-quality wedge surfaces.

The focal point created by the off-axis parabola (OAP) is then imaged onto a wavefront sensor (PHASICS SID4) using a high-quality objective (TSO apochromat F77) with a 50 mm aperture and  $24\times$  magnification. The manufacturer specifies a resolution of  $1.6\ \mu\text{m}$  for this objective. A closed-loop system involving a deformable mirror in the JETi200 compressor chamber is used to optimize the wavefront and correct distortions. Additionally, the focus can be manually adjusted and imaged on a CCD (charge-coupled device) camera.

The stability of both the near- and far-field is monitored by utilizing the low transmission ( $\leq 1\%$ ) of the laser pulse through the folding mirror located before the OAP.

### 3.1.1 Laser beam profile

To ensure the successful operation of the experiments, it is crucial to have a high-quality laser beam profile. In Laser Wakefield Acceleration (LWFA), a short-pulse laser is tightly focused to achieve high intensities, enabling it to generate a wakefield. However,

it must also maintain its guiding ability over an extended distance. It's important to note that only the energy concentrated in the center or centroid of the laser beam is effectively guided and contributes to the acceleration process. Energy distributed in the peripheral regions or "wings" of the laser beam is lost, which in turn reduces the peak intensity of the laser pulse [101]. Using the setup previously described, it is possible to scan both the far and intermediate fields with the laser system operating at low power. Instead of directly characterizing the high-power laser pulse, an attenuated low-power laser pulse is employed for characterization. In this low-power mode, the laser pulses go through the same amplification path, beam path, and optical elements as in the high-power mode, with the exception of specific thermal effects. Consequently, it is expected that the focal spot in the low-power mode closely resembles that in the high-power mode, making it a more manageable way to gather crucial data about the laser's characteristics.

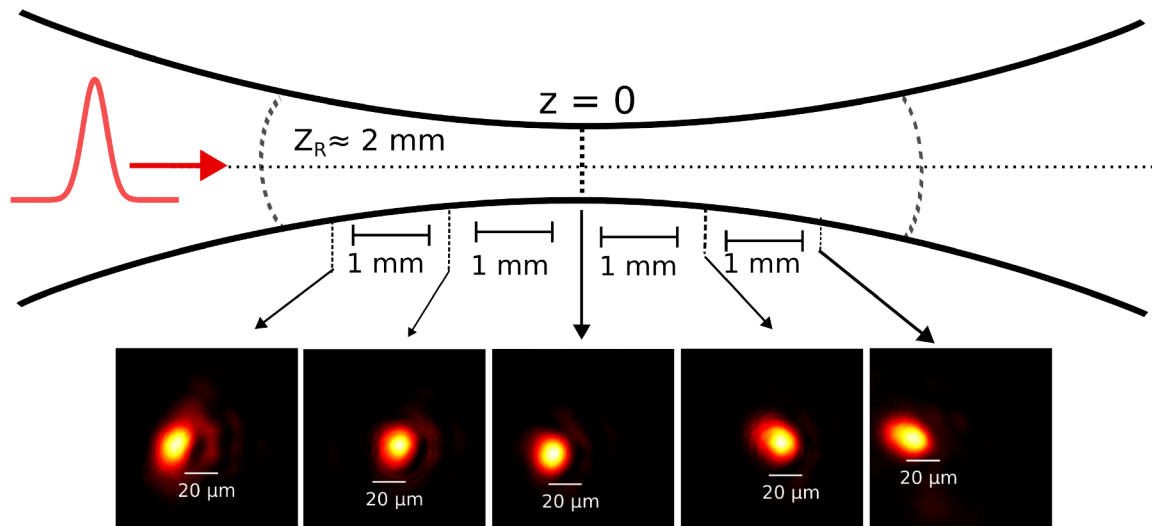


Figure 3.2: The scanning of the laser beam profile using  $f/20$  off-axis parabola around its focus spot. The spot size of  $20 \mu\text{m}$  was reached near the focus of the beam ( $z = 0$ ). The beam waist contains  $\sim 76\%$  of the laser energy, which corresponds to the Strehl-ratio of 0.9. The formation of ring-like structure around the center spot can be observed as we move away from the focus spot in either direction. The laser profiles were obtained at low intensity.

Figure 3.2 illustrates the evolution of the laser profile in a vacuum. The wavefront is optimized using a wavefront sensor (PHASICS SID4) operating in a closed loop with a deformable mirror. In this setup, the off-axis parabola (OAP) is able to achieve a focal spot size of  $20 \mu\text{m}$  (FWHM) in a vacuum. Approximately  $76\%$  of the laser energy is concentrated within the beam waist, defined as the region where the intensity drops

to  $e^2$  of the peak intensity. The focal spot maintains a Strehl ratio of 0.9, indicating high optical quality.

As the scan progresses, a Gaussian profile is preserved at the center of the beam, while the energy fraction decreases to below 60% towards the outer regions. The reduction in energy fraction at the outer fringes is likely responsible for the missing portion of beam energy observed in the figure 3.2.

### 3.1.2 Gas targets

Indeed, the choice of the plasma medium is a critical factor in Laser Plasma Acceleration (LPA) experiments. The density profile and characteristics of the plasma directly impact the performance and capabilities of LPAs. Various types of plasma targets have been developed to suit different experimental goals and conditions [58, 102, 103]. The choice of target depends on the specific goals of the experiment, such as producing high-energy electron beams, generating coherent X-ray radiation, or studying fundamental plasma physics. Different targets have distinct density profiles and plasma characteristics, which can be tailored to meet the requirements of the experiment. In this work, gas cell and gas jet has been used to produce the X-rays using ionization injection and shockfront injection mechanism respectively.

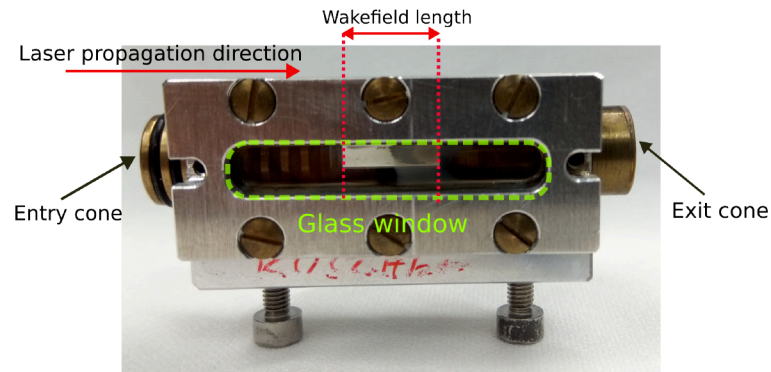


Figure 3.3: Variable length and density gas cell used at JETi200 for the experimental campaign described in this thesis. The length of the accelerator is varied by the varying the relative position of the entry and exit cones. Glass windows enable a transverse probe beam. The entry and exit cones are made of brass for high durability and have an orifice of  $800 \mu\text{m}$ .

**Gas cell** The experiment described in Chapter 4 utilized a versatile aluminum gas cell with adjustable density and length. This gas cell was designed by Dr. Stephan Kuschel from Helmholtz Institute Jena and had a maximum length of 20 mm. Figure 3.3 provides a visual representation of the gas cell and its components. The length of

the gas cell could be adjusted as needed for the experiments. This was achieved by changing the position of the entry cone tip inside the cell. The gas cell was equipped with replaceable glass windows (colored purple in the figure) that allowed for optical probing. These windows provided access for optical diagnostics and measurements. The electron density within the gas cell could be controlled by adjusting the backing pressure of the gas reservoirs connected to the cell. This allowed for precise control over the plasma density, which is a crucial parameter in laser plasma acceleration experiments.

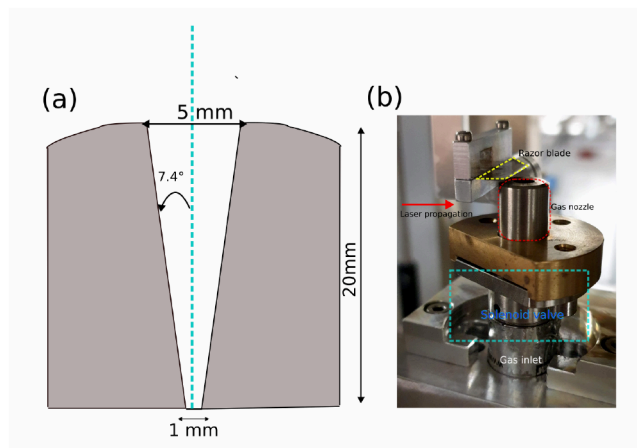


Figure 3.4: Gas jet and blade setup used at JETi200 for producing quasi monoenergetic electrons using shockfront injection mechanism (side view (b)). (a) Sketch of the 5mm nozzle design. (b) A 5mm gas nozzle (red) is mounted on a Peter-Paul solenoid valve (blue). A razor blade (yellow) is introduced to induce a shock front.

**Gas jet** In the experimental investigations detailed in Chapters 5, we employed conical aluminum gas nozzles to generate a supersonic flow of gas [102]. This involved the containment of gas within a reservoir, pressurized within the range of 10 to 100 bar. Subsequently, controlled release of the gas was achieved through the implementation of a Peter-Paul solenoid valve. The outcome of this process yielded a characteristic density profile, typically exhibiting a flat-top configuration with brief density gradients on either side. These controlled conditions provided electron densities on the order of few  $10^{18}\text{cm}^{-3}$ . Also, a steel blade was inserted into the gas flow above the nozzle to create a shock and facilitate shock-induced electrons. The blade was mounted on a rotational and translational stage allowing the change of height and the relative position of the blade with respect to the gas nozzle in all three dimensions. Figure 3.4 shows photo of this setup.

When an obstruction, in this case, a razor blade, is introduced into the gas flow, the

gas must locally adjust to accommodate this disruption. Consequently, this process results in the formation of a shock front, which propagates through the gas flow at a specific angle. The shock has a higher density than the surrounding gas and very sharp edges. This creates a sharp density transition profile which facilitates the generation of quasi-monoenergetic electrons when an ultra-high intensity is focused on it.

## 3.2 Electron beam characterization

A crucial component of LWFA diagnostics is the electron spectrometer, a tool that facilitates the measurement of various parameters related to the accelerated electron beam. This includes assessing beam quality, determining charge, characterizing electron energy, quantifying energy spread, and measuring divergence with pointing on the non-dispersive axis.

In order to utilize magnetic dispersion as a diagnostic tool, a scintillating LANEX screen is strategically placed behind the magnet. By performing calculations that take into account the trajectories of electrons across a range of energies, it becomes possible to establish a direct correspondence between each position on the screen and a specific electron energy. In situations where all electrons are initially directed into the magnet with a single defined position and angle, each location on the detector screen directly corresponds to a unique electron energy. However, when the incoming electrons exhibit variations in both angle and position, which is common in LWFA experiments, a single position on the detection plane can be associated with multiple electron energies.

These variations in angle and position typically arise from two primary sources. Firstly, the entire electron beam may be ejected from the accelerator at an angle relative to a reference axis that varies from shot to shot. This phenomenon, known as beam pointing, causes a systematic shift of the dispersed beam on the detection plane relative to the reference axis. Without appropriate corrections, this shift can lead to inaccuracies in the inferred electron energy. To address this issue, multiple detector screens or spatial references can be employed to identify and rectify beam pointing effects [104].

Secondly, the electron beam possesses a finite divergence, implying that even at a constant energy, electrons entering the magnetic field exhibit a range of angles. Consequently, instead of a single point, one energy level is mapped onto a finite spot, meaning that the dispersion or energy axis becomes intermingled with the spatial components of the beam.

In the experiments performed in this thesis, the detectors employed were scintillating

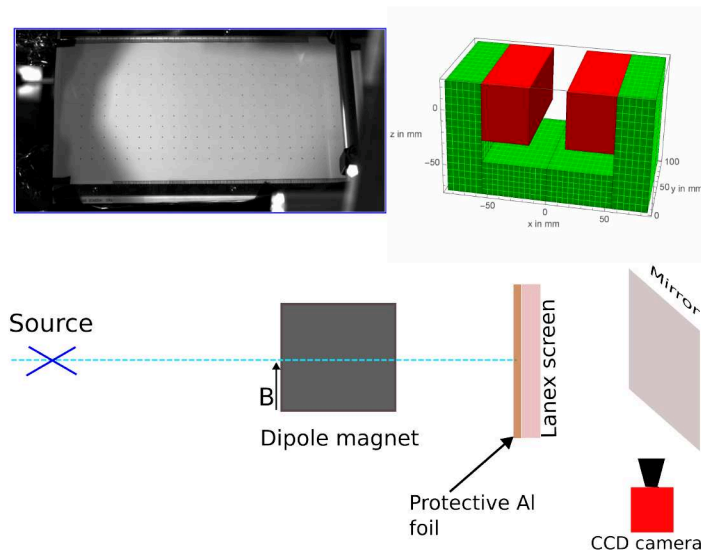


Figure 3.5: The electron spectrometer’s typical layout is depicted here. The electrons that have been deflected by the dipole magnet strike the LANEX screen, which is shielded by aluminum foil to protect it from any residual laser light. The scintillation occurring on the LANEX screen is captured using a CCD camera, aided by a mirror. In the top-left inset, you can see a reference image of an electron spectrometer screen. The dots on this image were manually added for spatial calibration purposes, and they are spaced 10 mm apart. Additionally, a paper ruler was affixed at both the top and bottom of the spectrometer for further reference. In the top-right inset, there’s a 10 cm dipole magnet with a 3 cm free pole gap, boasting a peak magnetic field strength of 800 mT. This magnet, designed in-house by Dominik Hollatz, was utilized in the experimental work detailed in this thesis.

Lanex screens, specifically Kodak Biomax MS [105]. These screens were captured using a combination of a mirror and a Basler 12-bit CCD camera. The screen was used as electron spectrometer by moving the magnet into the electron beam path, and was used for measuring pointing fluctuation by removing the magnet from the electron beam path (Figure 3.5).

### 3.3 Betatron beam characterization

X-ray photons in the energy range of 1 keV to 100 keV can interact with electrons in solid matter through various scattering processes. As an illustrative example, figure 3.6 displays the cross-sections for different scattering phenomena in silicon. The cross-section represents the likelihood of a scattering event occurring. Silicon is a

potential bulk material for CCD cameras.

In the figure 3.6, several typical trends in the interaction of X-ray photons with matter are evident. The total cross-section exponentially decreases as the photon energy increases. Consequently, for higher-energy X-rays, the detector material needs to be thicker to ensure sufficient photon detection. In the lower energy range, the photoelectric effect dominates, while Compton scattering becomes more significant for higher X-ray energies, typically above several hundred keV. Elastic scattering of photons with free and unbound electrons contributes to background signals.

Betatron radiation has a broadband nature, emitting X-rays and gamma rays, as discussed in chapter 2. Betatron diagnostics usually record photons with energies less than 100 keV, but gamma photons with energies around 1 MeV have also been observed [106]. Detector technology has seen significant advancements in recent years and is expected to enhance betatron diagnostics in the near future. However, the majority of betatron photons typically have energies around 10 keV, and silicon-based pixel detectors can effectively cover photon energies only up to 30 keV. Hence, another new detector based on the coupling of scintillating screen with the CMOS chip, having energy range 10 - 150 keV, has been employed in the experimental work presented in this thesis to characterise the photon energies up to  $\approx 100$  keV.

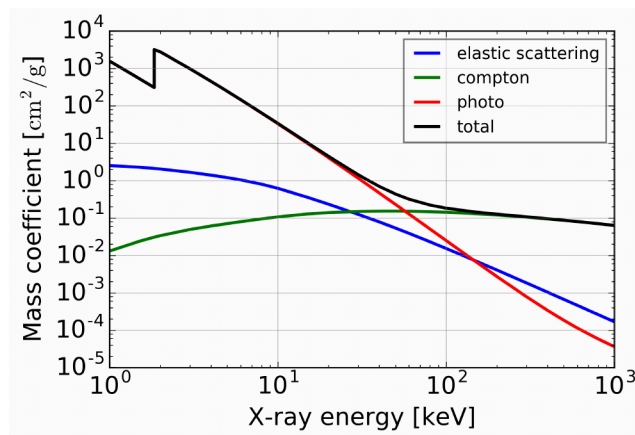


Figure 3.6: The total cross section of different X-ray photon energies when they interact with silicon. Photons in the keV energy range interact with the solid matter differently [107].

### 3.3.1 Detection System

The high resolution X-ray cameras available in the market today can be broadly categorized into two: direct detection (DD) and indirect detection (ID).

Direct detection (DD) cameras operate by exposing a silicon chip directly to X-rays. These X-rays are absorbed by the silicon, leading to the creation of electron-hole pairs. The quantity of electron-hole pairs generated is directly proportional to the energy of the incident X-ray photon [108]. This method is highly sensitive for X-ray detection, particularly for energies up to around 10 keV. However, its effectiveness decreases for X-ray energies higher than this, as very few X-rays are absorbed within the depletion region of the CCD (charge-coupled device).

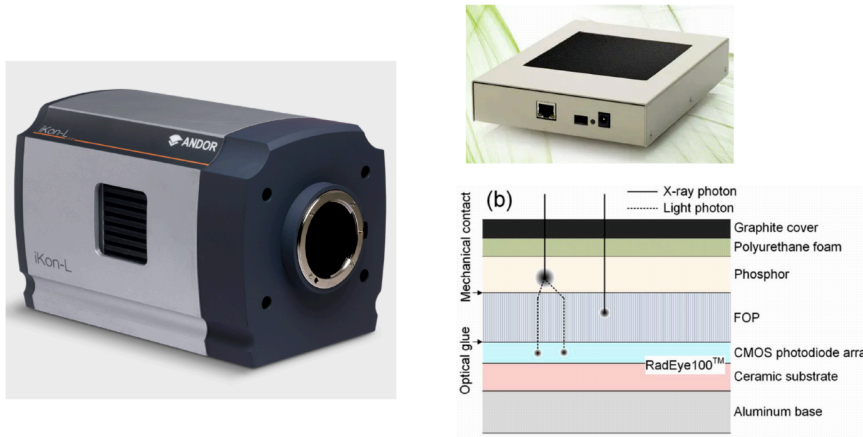


Figure 3.7: The back illuminated direct detection ANDOR CCD (left) and the indirect detection scintillating screen+ CMOS Shad-o-box (right) used as the X-ray detector for the experimental campaign presented in this thesis.

On the other hand, indirect detection (ID) cameras function by imaging a scintillator material. This scintillator converts X-ray photons into visible light photons. The camera then detects these visible light photons. While this process can result in some loss of information due to the conversion steps, scintillators can exhibit reasonable quantum efficiency (QE) for X-ray energies up to approximately 100 keV. In standard

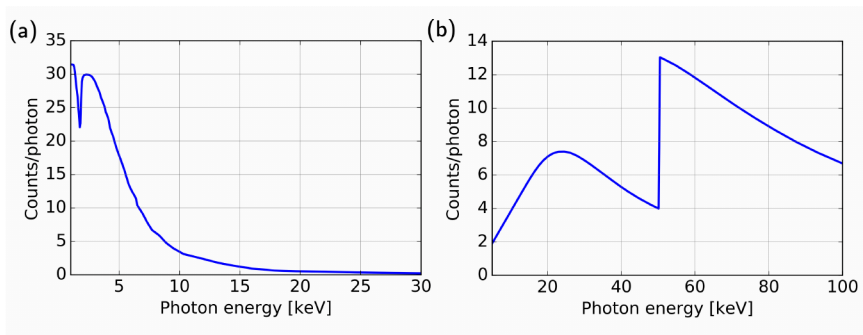


Figure 3.8: The detector sensitivity for the ANDOR (a) and the Shad-o-box (b) used during the experiments.

charge-coupled devices (CCDs), illumination occurs from the front side of the chip. However, this configuration presents a challenge for capturing shorter-wavelength photons because they have to traverse an inactive layer of electrical connections on the front side, which can absorb these shorter-wavelength photons. To address this issue and enhance sensitivity to shorter wavelengths, the CCDs used in the experiment are illuminated from the backside of the chip. This allows the device to efficiently capture and detect shorter-wavelength photons.

The first detector used in the experiments was an **ANDOR DO936N-M0Z-BEN** [109]. This CCD chip featured a high pixel count with dimensions of 2048 x 2048 pixels and an overall size of 27.6 mm x 27.6 mm. The small pixel size, measuring 13.5  $\mu\text{m}$  x 13.5  $\mu\text{m}$ , was especially advantageous for imaging objects using X-ray radiation, where achieving a high level of spatial resolution was essential. The camera was positioned at a distance of 2.3 meters from the target and was situated within a lead-shielded area. It was connected directly to the vacuum chamber with 50  $\mu\text{m}$  thick high purity beryllium window (Fig:3.7).

	<b>Andor iKon-L</b>	<b>Shad-o-box 6K-HS</b>
Set-up	Vacuum	Standalone
Pixels	2048 $\times$ 2048	2940 $\times$ 2304
Pixel Size	13.5 $\mu\text{m}$	49.5 $\mu\text{m}$
Well depth	150,000 $e^{-1}$	2,500,0000 $e^{-1}$
Digit.	16 bits	14 bits

Table 3.1: Parameters for the X-ray cameras

To capture the complete angular divergence of the X-ray beam, a large area ID detector **Shad-o-Box 6K HS Camera** from TELEDYNE was used [110]. It has the large detection area of 110 mm  $\times$  150 mm with 49.5  $\mu\text{m}$  pixel size. The CMOS sensor inside the Shad-o-Box HS camera contains a direct-contact Gd<sub>2</sub>O<sub>2</sub>S scintillator (DRZ fine). The scintillator in use is responsible for converting X-ray photons into visible light, which is then detected by the CMOS photo-diodes. To safeguard the sensor against potential harm and to prevent interference from ambient light, a thin 2 mm graphite cover is applied. Furthermore, the Shad-o-Box HS camera includes shielding composed of lead and steel to shield the camera's electronics from X-ray radiation. These cameras are capable of detecting X-ray energies as low as 10 keV (Fig: 3.7).

### 3.3.2 Betatron Beam Profile and Source Size

To characterize the angular distribution of the betatron beam, the detectors were positioned directly within the path of the X-ray beam. It is advantageous to utilize detectors with a substantial surface area when conducting beam profile analyses, including assessments of beam divergence and the stability of beam pointing.

To accurately calculate the source size of the betatron beam generated in LWFA, it's critical to ensure that the measured radiation originates solely from the laser-plasma interaction and not from electrons striking the chamber walls. To achieve this, an object was placed between the laser-plasma interaction region and the X-ray detector, allowing for a shadowgraphic image of the micrometer-sized object to be captured on the detector.

The key indicator of success in this approach is obtaining a high-contrast image of the back-lit micrometer-sized object. Such an image would suggest that the radiation primarily originated from the laser-plasma interaction, as any background radiation resulting from the electrons would diminish the obtained image contrast. If the back-lit object is distinctly visible in the raw image obtained, it implies that the source size cannot exceed the dimensions of the micrometer-sized back-lit object. Otherwise, as the source size increases, it would blend with the background, resulting in poor image contrast. To perform this validation, tungsten wires with dimensions on the order of micrometers were employed as the back-lit object.

In the process of calculating the source size through geometrical analysis, a knife-edge was utilized as the back-lit object. The shadowgraphic image produced by the knife edge can be divided into three distinct regions:

- **High Intensity Region:** This area corresponds to the portion of the image where the blade of the knife is not obstructing the X-rays, resulting in high-intensity radiation.
- **Low Intensity Region:** In this section, the image corresponds to the shadow cast by the knife blade, resulting in lower-intensity radiation.
- **Transition Area:** This area contains information related to both the source and the knife-edge, representing the region where the transition between high and low intensity occurs.

For this geometrical analysis to yield accurate results, several assumptions are made:

- **X-ray Absorption:** It is assumed that the knife-edge has 100% X-ray absorption, meaning that no X-rays pass through the knife-edge itself.

- Straight Knife-edge: The knife-edge is assumed to be perfectly straight, without any bends or irregularities.
- Gaussian Source Distribution: The source distribution is assumed to be Gaussian in shape.
- Neglecting Diffraction: Diffraction effects are neglected in the analysis.

With these assumptions in place, the analysis employs a step-function as the model for the knife-edge and a Gaussian-like source distribution. When these two functions are convolved, the resulting intensity distribution on the raw image takes the shape of an error function given by:

$$I(x) = I_0 + \frac{I_1}{2} [1 + \operatorname{erf}(\frac{x - x_0}{d})] \quad (3.1)$$

Where  $I_0$  and  $I_1$  are the offset and the intensity of the X-ray source and the resulting error function's width,  $d$ , can be estimated by fitting the error function to the intensity profile obtained on the raw image. taking the geometric magnification  $M$  into account, the Gaussian-like source size,  $\sigma$ , can be calculated by using

$$\sigma = d.M \quad (3.2)$$

By delving deeper into the raw image of the shadowgram, one can see the diffraction features which could be explained by Fresnel diffraction method [111].

Fresnel diffraction is the diffraction pattern obtained on a detector when an electromagnetic wave is impinged on an arbitrarily shaped aperture and is diffracted in the near field. It is dependent on the wavelength of the wave  $\lambda$  and the distance between the diffracting object and the detector,  $v$ . To work in Fresnel regime requires the Fresnel number  $F = A^2/(\lambda v)$  to be larger than 1 where  $A$  is the characteristic size of the object.

The electric field ( $dE$ ) at point  $P$  on the detector from a point source  $S$  emitting spherical wavefront having wavelength  $\lambda$  diffracted at coordinates  $(x, y, z)$  is given by the Fresnel-Kirchhoff equation :

$$dE(P) = -\frac{K(\theta)E_0}{\lambda pr} \exp(i[k(\rho + r) - \omega t])d\sigma, \quad (3.3)$$

where  $k = 2\pi/\lambda$ ,  $\omega = c/k$  and  $K$  is the Kirchhoff function,  $E_0$  is the source strength and respective parameters are shown in figure 3.9. Using small angle approximation,

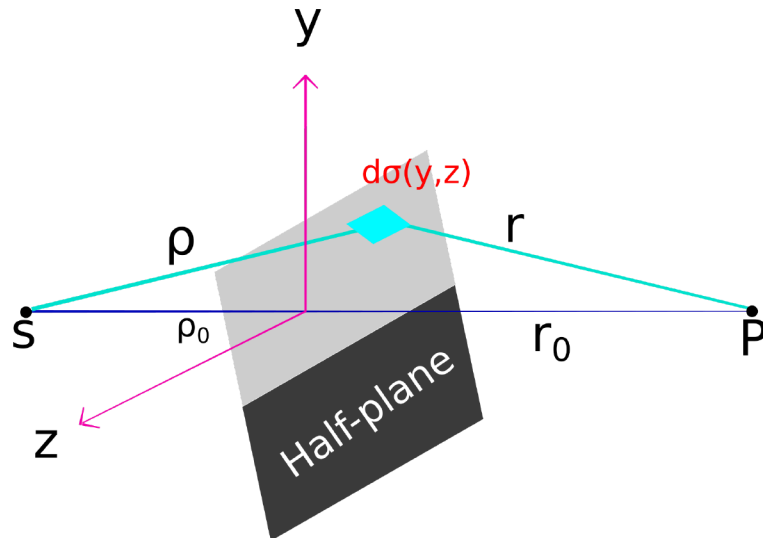


Figure 3.9: Fresnel diffraction sketch.  $S$  is the source emitting spherical waves of wavelength  $\lambda$  and  $P$  is the point on the detector. The half plane is formed by the obstacle (here blade).  $r$  and  $\rho$  are the distances.

the amplitude of the equation (3.3) becomes  $\frac{K(\theta)E_0}{\lambda\rho r} \approx \frac{E_0}{\lambda\rho_0 r_0}$ , where  $\rho_0$  and  $r_0$  are the source-back-lit object and the back-lit object-detector distances respectively [46, 83].

### 3.3.3 Betatron Beam Spectral Characterisation

Due to a very high photon flux generated from the LWFA electrons, the methods for spectral characterisation of the betatron beams were limited. The spectrum could be characterised using single photon counting method [46] but due to our high total number of *photons/eV* this method could not be used. Due to fluctuation in laser parameters on shot to shot basis, it is convenient to have a spectral diagnostic having broad spectral range and can be analysed on a single shot basis. One such method is based on the measurement of the x-ray photon transmission through a set of different filters called Ross filters. The filters used for spectral evaluation in this thesis are shown in figure 3.10.

Filters	Niobium	Copper	Tin	Neodymium	Tantalum	Lead	Mylar	Aluminum
Thickness ( $\mu\text{m}$ )	20	50	40	100	34	30	120	30

Table 3.2: Ross filters used during the experiment with their respective thickness.

The Ross filter pairs have identical transmission except the energy range between their K-edges. The difference in the signal obtained on detector through two filters is

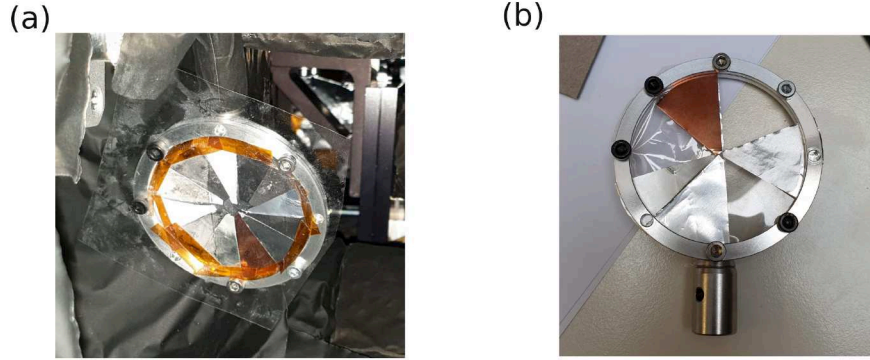


Figure 3.10: The image of the Ross filter pairs used for (a) ionisation injection campaign and (b) Shockfront campaign. The filters were designed keeping in mind the expected photon energy radiated from both injection method. An area without any filter was left in both the filter wheel to get the reference beam used for spectral calculation.

due to the energy band between the two K-edges. The transmission through four such filters is shown in the figure 3.11. The subtracted filter transmission of Ross filters provides data points for different energy bins, giving a rough idea about the betatron spectrum 3.11.

The X-rays transmitted through the filters were recorded on the X-ray diagnostic cameras. The estimated signal level on the camera image for filter  $i$ ,  $Y_i$ , is given by

$$Y_i = A \int_{E_{min}}^{E_{max}} E.S(E).Q(E).T_i(E)dE \quad (3.4)$$

Where the integration limits were the energy sensitivity of the detectors used,  $A$  proportionality constant,  $S(E)$  the x-ray number spectrum ( $dN/dE$ ),  $Q(E)$  quantum efficiency of the camera and  $T_i(E)$  is the transmission of the filter  $i$  and the materials in betatron beam path until the detector.

The spectrum  $S(E)$  was assumed to be an on-axis synchrotron (*cite*) spectrum with a critical energy  $E_c$  that was to be determined. To find the  $E_c$  which fits the measured data, we need to minimise the quantity given by

$$X = \sum_i (Y_{m,i} - Y_i)^2 \quad (3.5)$$

Where  $Y_{m,i}$  is the measured counts through filter  $i$ . The  $E_c$  with the smallest  $X$  parameter was taken as the true critical energy for the given data.

To calculate the number of photons we subtract the measured signal [*counts/steradian*] between the Ross filter pairs and take into account the the transmission of the filters

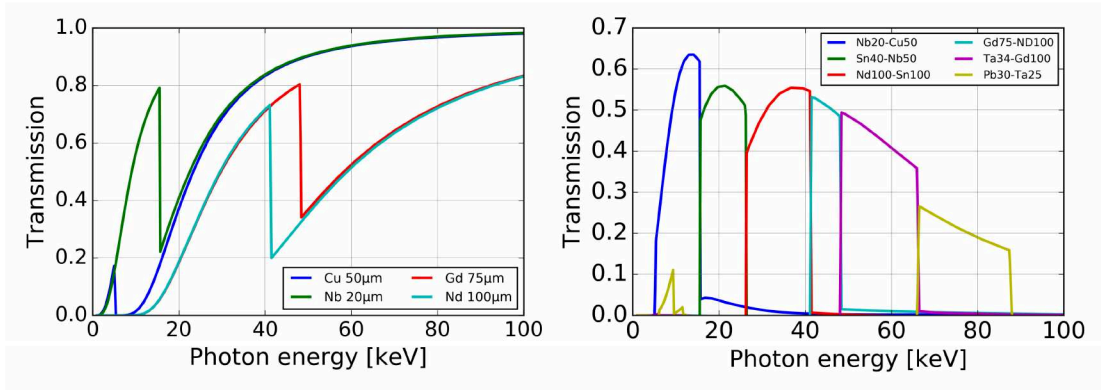


Figure 3.11: (Left) The transmission curve for the Ross filters used for the experiment. The metals and their thickness were chosen such that they have similar K-edges. (Right) Filter pairs with their transmission curves subtracted, providing energy bins in the range 10-100 keV. These pairs were used to spectrally characterise the betatron spectrum measured for ionization injection scheme.

and the detector sensitivity. The absolute number of photons/energy bin / solid angle can be given as:

$$\mathcal{N}[\text{Photons}/\text{keV}/\text{srad}] = \frac{\mathcal{R}[\text{counts}/\text{srad}]}{\frac{\int_{E_{min}}^{E_{max}} (T_j - T_i) K(E) dE}{E_j - E_i} [\text{counts}/\text{photons}]} \cdot \frac{1}{(E_j - E_i) [\text{keV}]} \quad (3.6)$$

Where  $K(E)$  is the detector sensitivity,  $T_{i,j}$  Ross pair filters,  $E_j - E_i$  the edge energies of the filters used.

# 4 Bright and Stable X-rays from Ionization Injection

To compare the betatron X-ray sources generated from different injection schemes, a key metric of interest is the peak brightness of the source. This physical quantity is quantified in units of photons per unit area per second per milliradian squared per 0.1% bandwidth. Calculating peak brightness requires measuring the betatron beam's divergence in milliradians, the source size, intensity in photons per second, and the spectral energy distribution in keV.

Within this chapter, LWFA with gas cell as the target and Nitrogen ( $N_2$ ) (5% by volume) as the dopant was studied. Hydrogen ( $H_2$ ) and Helium (He) at 95% by volume were used as the background gases separately to produce two different gas targets. Furthermore, the betatron radiation emitting from gas mixture producing electron beams with higher charge, strong dephasing and smaller pointing fluctuation was characterised and the results are discussed. An in-depth characterization of betatron X-rays generated from laser-plasma interaction employing ionisation injection (as discussed in Sec. 2.3.2) scheme has been conducted, allowing for a comprehensive analysis.

## 4.1 Electron Beam Measurements

Figure 4.1 illustrates the experimental setup utilized in this study. The laser's energy was measured to be  $\sim 3$  J upon reaching the target. Post-compression, the laser pulse exhibited a full width at half maximum (FWHM) duration of  $\approx 23$  fs. The pulse was focused onto the gas cell, using an off-axis parabolic mirror with an f/20 configuration and a focal length of  $\approx 2.5$  m, with a spot size FWHM of approximately  $20 \mu\text{m}$ . The accelerated electrons were captured on a scintillating Lanex screen. In the experimental arrangement, the electron beam profile (scintillating screen) also functioned as an electron spectrometer when the magnet was strategically positioned in the path of the generated electrons. This setup allowed for the characterization and analysis of the electron beam profile. The electron beam profile was located 1 m away from the gas target and was shielded with  $30 \mu\text{m}$  thick aluminum foil. Additionally, it was slightly angled with respect to the the laser beam axis to mitigate any potential damage resulting from back reflection to the laser. The position of the electron beam

profile could be adjusted, enabling up and down movement with respect to the laser axis.

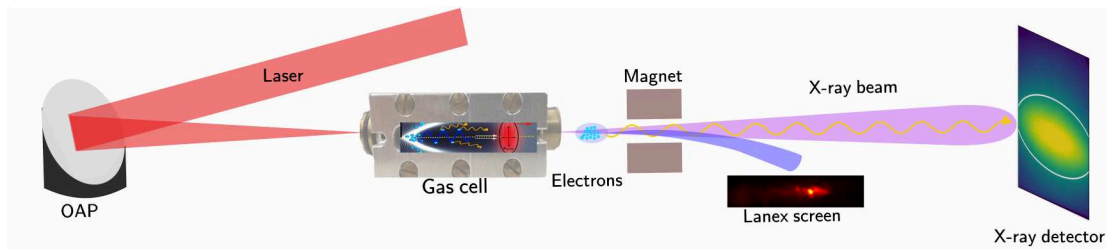


Figure 4.1: Diagram of the experimental set-up for the betatron beam characterization from ionization injection method. The laser pulse is focused by an f/20 off-axis parabola over a distance of 2.5 m onto a gas cell with gas cell length 10 mm. The accelerated electrons are then swiped by the permanent magnet placed in the electron beam path onto a scintillating screen for energy and charge measurements. To measure the pointing fluctuation in the electron beam and the charge, the motorised magnet is moved out of the way of the electron beam. The betatron beam emanating from the accelerated electrons is captured by an X-ray detector 2.3 m downstream from the source.

The gas cell used had been well characterised and the gas density formula was given by :  $N[10^{18}/\text{cm}^3] = 2.4(1.42 * p[\text{bar}] + 0.15)$  For 1mm aperture and gas mix of  $He : N_2$  95 : 5, where  $p$  is the backing pressure in bar. A pressure scan was done to compare the charge obtained by the mixtures  $He : N_2$  95 : 5 and  $H_2 : N_2$  95 : 5 for 10 mm gas cell length. The pressure scan resulted in reaching higher backing pressure for  $H_2 : N_2$  than  $He : N_2$  as H is lighter than the He. This allowed us to utilize higher backing pressure for H gas mix without damaging the gas cell (i.e. exploding of the glass windows used in the gas cell for transverse probing). The result of the pressure scan shows the change in charge yield for both the gas mixture with the plasma density. It was observed that the gas mix containing H has more charge compared to the gas mix with He even at same plasma density (Fig: 4.2 [Left]). The pointing fluctuation of the electron beam for  $H_2 : N_2$  at  $n_e = 7.5 \times 10^{18}[\text{cm}^{-3}]$  was smaller than  $He : N_2$  at  $n_e = 5.1 \times 10^{18}[\text{cm}^{-3}]$ . The fixed plasma density as operating points for both gas mix was chosen at the parameters where the electron signal was stable and reproducible. It showed that even at higher plasma density the pointing stability of gas mix with H is higher than the pointing stability of the gas mix with He (Fig: 4.2 [Right]). The higher charge for Hydrogen is due to higher electron background signal implying a longer injection duration for Hydrogen than Helium. This means that the injection threshold is achieved earlier for Hydrogen than Helium (Tab:2.1). Due to higher charge and

better pointing stability, the gas mix with H was chosen for further studying of X-ray generation at JETi200.

The primary objective of this experiment was to measure the most intense betatron

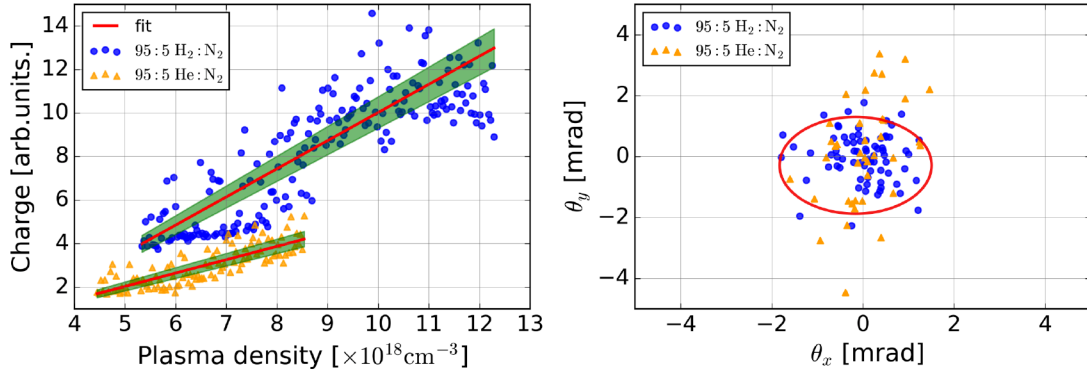


Figure 4.2: Electron charge yield vs plasma density scan for gas mix  $H_2 : N_2$  (Blue) and  $He : N_2$  (Orange). (Left) Higher charge was recorded at the same plasma density for  $H_2 : N_2$  gas mix. The linear fit (red) with standard deviation (shaded green) shows the mean charge yield for both the gas mix. (Right) The  $\theta_y$  pointing fluctuation of gas mix  $H_2 : N_2$  was lower than  $He : N_2$  showing better pointing stability of the electron beam from  $H_2 : N_2$  gas mix for the data taken at fixed plasma densities.

beam, making the X-ray detectors pivotal as the primary diagnostic tool. For this, the electron beam characteristics (Charge, pointing stability) were fine-tuned based on the observed betatron yield on the detector during the experiment. To optimize the outcomes, a thorough pressure scan was conducted, holding all other experimental variables constant, while measuring the betatron yield on the detector (Fig:4.3). Following this pressure scan, two specific operating pressure points were selected (light gray shaded). The pressure points corresponded to  $n_{e,1} = 9.3 \times 10^{18}[\text{cm}^{-3}]$  (**High density**) and  $n_{e,2} = 7.5 \times 10^{18}[\text{cm}^{-3}]$  (**Low density**). These points were chosen to achieve the highest attainable yield while ensuring reproducibility with minimal fluctuation in photon flux. For plasma density  $> 9.5 \times 10^{18}[\text{cm}^{-3}]$  the photon yield variance was quite high and the Gaussian-fit shows minimal ( $< 20\%$ ) increment in the mean yield.

After selecting the two plasma densities  $n_{e,1}$  (High plasma density) and  $n_{e,2}$  (Low plasma density) for a gas cell length of 10 mm containing gas mix  $H_2 : N_2(95 : 5)$ , the electron spectrum for both the cases were measured. As the gas cell length was 10 mm, the dephasing length (Sec:2.3.3) for  $n_{e,1}$  and  $n_{e,2}$  was calculated to be 0.85 mm and 1.1 mm respectively. The injected electrons caught up to the tail of the laser pulse and had increased transverse oscillation seen also on the electron spectrum shown in

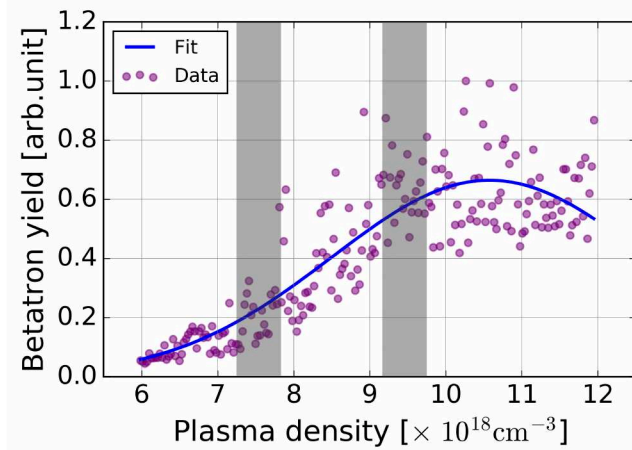


Figure 4.3: Total integrated betatron yield measured with the change in plasma density (backing pressure). A Gaussian fit (blue solid line) was done to show the variation of betatron yield with changing pressure. Two plasma densities for this experimental campaign are marked with shaded region. The increased variance in betatron yield at higher plasma densities may be attributed to instabilities introduced in the higher energy range of the electron spectrum. These instabilities could result from the wobbling of the betatron bubble or the overlapping of the electron bunch with the laser tail.(see Fig:4.4).

figure 4.4. Dephasing leads to the reduction of peak electron energy and beam quality [76]. As dephasing length is  $\propto (\text{plasma density})^{-1}$ , higher plasma density leads to smaller dephasing length (stronger dephasing) and hence greater electron beam divergence (Fig: 4.4[Top]).

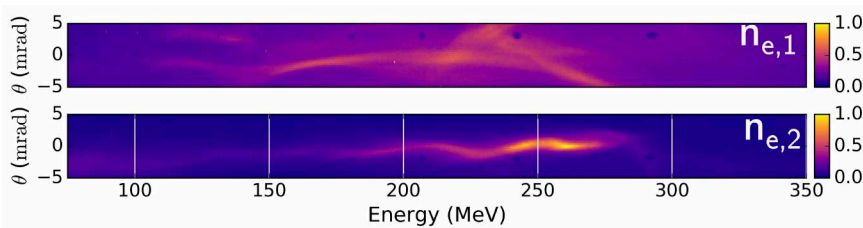


Figure 4.4: Single shot electron spectrum after dephasing strongly for high plasma density ( $n_{e,1}$ ) and low plasma density  $n_{e,2}$  for a gas cell length of 10 mm obtained on Lanex screen. Stronger dephasing for high plasma density ( $n_{e,1}$ ) lead to bigger divergence of the electron beam [Top]. The charge was calculated to be 174 pC for  $n_{e,1}$  (Top) and 204 pC for  $n_{e,2}$ (Bottom.)

The reconstructed spectra is shown for both the cases ( $n_{e,1}$  and  $n_{e,2}$ ) in figure 4.5. Electrons accelerated through ionization injection mechanism show a broad, continuous spectrum. As the laser beam is self-focused and compressed in the plasma, the inner shell electrons of the dopant ( $N_2$  here) is released continuously producing a broad

spectrum. The total mean charge was calculated to be  $163 \pm 32$  pC for  $n_{e,1}$  and  $207 \pm 40$  pC for  $n_{e,2}$  respectively. In general, the injected charge increases with the increase in plasma density which is not the case here. This could be due to higher plasma density reducing the bubble radius and hence smaller volume is available for electron injection inside the bubble. The shrinking of the wakefield bubble leads to smaller injected charge.

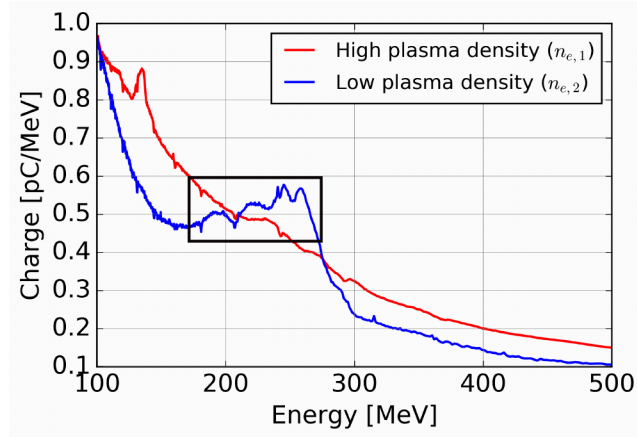


Figure 4.5: Reconstructed single shot electron spectrum for high plasma density (red) and low plasma density (blue) is shown in the figure. The continuous spectrum for both the case shows the peak around 200-250 MeV. For low plasma density, due to dephasing, the strong wiggling of the electron beam is imprinted on the electron spectra as modulations between 180-260 MeV (Black rectangle). Due to higher plasma density this effect is not localised on the electron spectrum for  $n_{e,1}$ .

Furthermore, the electron beam pointing fluctuation for both the plasma densities was plotted (Fig:4.6) and it was observed that for higher plasma density (red) the variance in the pointing fluctuation was higher. For  $n_{e,1}$ ,  $(\Delta\theta_x, \Delta\theta_y)$  was (7.2 mrad, 6.3 mrad) and for  $n_{e,2}$ ,  $(\Delta\theta_x, \Delta\theta_y)$  was (0.6 mrad, 0.8 mrad). The standard deviation in the pointing fluctuation for  $n_{e,1}$  was almost  $10\times$  higher due to high plasma density, for which the bubble size becomes smaller and hence the accelerating electron catches up to the laser tail quickly. This results in the strong transverse oscillation of the electron bunch in the laser electric field. For lower plasma density, the fluctuations are smaller due to lower degree of overlap between the laser pulse and accelerated electron bunch as seen in the Fig: 4.6.

In conclusion, with 10 mm gas cell length having a gas mixture of hydrogen ( $H_2$ ) at 95% and nitrogen ( $N_2$ ) at 5% provided a peak energy of  $\approx 250$  MeV and total charge around 200 pC. Due to high plasma density and longer gas cell length, the injected electrons were overlapped with the tail of the laser. The injected charge was expected

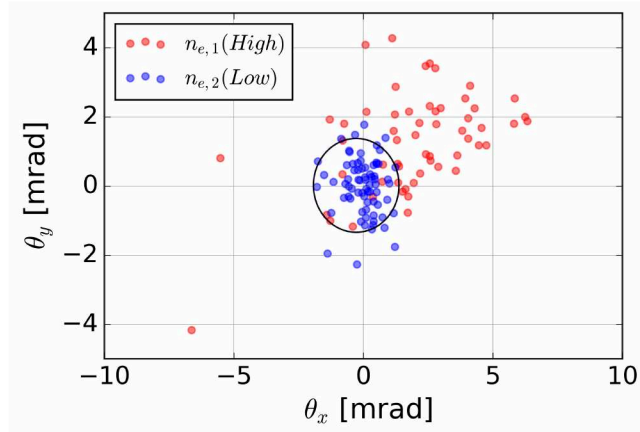


Figure 4.6: Pointing fluctuation measured for  $\mathbf{n}_{e,1}$  (high plasma density) and  $\mathbf{n}_{e,2}$  (low plasma density). The variation of the electron beam on shot to shot basis was higher for  $\mathbf{n}_{e,1}$ . The standard deviation in  $\theta_x$  and  $\theta_y$  was 10 times more for  $\mathbf{n}_{e,1}$ . Electron beams with greater pointing stability was generated from lower plasma density ( $\mathbf{n}_{e,2}$ ).

to increase with increasing plasma density but the total charge for  $\mathbf{n}_{e,1}$  was 20% less than the  $\mathbf{n}_{e,2}$  for same gas cell length. At lower density, the bubble size becomes bigger which accommodates more charge hence higher charge was seen for  $\mathbf{n}_{e,2}$ . The electrons observed in this experiment had their output energies in general lower than the prediction of the scaling law (Eq:2.29) due to smaller dephasing length because of higher plasma density.

## 4.2 Betatron Beam Measurements

During the interaction of an ultra-intense laser with plasma, the generation of a relativistic electron beam is accompanied by the production of X-rays (Subsection:2.5). These X-rays, known as the betatron beam results from the transverse oscillations of the relativistic electron beam, co-propagating through the laser axis. In this experimental setup, the X-ray diagnostics were positioned at a distance of approximately  $\approx 2.3$  m from the gas cell, ensuring a direct line of sight between the X-ray diagnostics and the X-ray source. To shield the detectors from laser light, a  $30 \text{ } \mu\text{m}$  thick aluminum layer was employed (Fig: 3.7).

For precise characterization of the betatron beam generated in this campaign, two types of X-ray detectors were utilized (subsection: 3.3.1). The first was a thermoelectrically cooled, back-illuminated X-ray CCD camera, and the second was a CMOS chip camera equipped with DRZ-fine Lanex as the scintillator, connected to the chip

using Fiber Optic Plates (FOP). The Shadobox camera was primarily utilized for measuring the critical energy and betatron beam profile. On the other hand, the ANDOR CCD camera was employed for determining the source size and assessing betatron beam stability in terms of photon flux and reproducibility.

### Betatron Beam profile, divergence and beam pointing

The betatron beam profile was directly measured by positioning the detector in the beam's path 2.3 m away from the source. The Shadobox detector, with an active area of  $2940 \times 2300$  pixels ( $10 \times 15$  cm<sup>2</sup>) and a pixel width of  $49.5$   $\mu$ m, was employed for this purpose. The Shadobox detector produces 14-bit images, providing high-resolution data for precise characterization of the betatron beam profile.

For 10 mm gas cell length, at a plasma densities  $\mathbf{n}_{e,1} \sim 9.2 \times 10^{18}$ cm<sup>-3</sup> and  $\mathbf{n}_{e,1}, \sim 7.5 \times 10^{18}$ cm<sup>-3</sup> the angular spread of the betatron beam for a single shot was found out to be  $25 \times 10$  [mrad<sup>2</sup>] and  $19 \times 12$  [mrad<sup>2</sup>] respectively. Taking mean electron energy measured during this experimental campaign  $\sim 200$  MeV ( $\gamma = 400$ ), the betatron strength parameter ( $\mathcal{K}$ ) is calculated (Tab: 4.1). A 25% increase  $\mathcal{K}$  for higher plasma density ( $\mathbf{n}_{e,1}$ ) along the laser polarization direction shows stronger transverse oscillation at higher plasma density. This is due to the injected electrons catching up to the tail of the driver laser and oscillating under the influence of the laser's electric field.

Plasma Density [ $\times 10^{18}$ (cm <sup>-3</sup> )]	$\mathcal{K}_x$	$\mathcal{K}_y$	$L_{dephasing}$ [mm]
$n_{e,1} = 9.2$	10	4	0.85
$n_{e,1} = 7.5$	8	4	1.1

Table 4.1: The wiggler strength parameter,  $\mathcal{K}$ , calculated for plasma densities  $\mathbf{n}_{e,1}$  and  $\mathbf{n}_{e,2}$ . For higher plasma density,  $\mathcal{K}_x$  is 25% higher in the laser polarization direction (x), and  $L_{dephasing}$  is around  $\sim 25\%$  smaller implying stronger wiggling at higher plasma density.

It is to be noted that the divergence of the betatron beam is a function of electron density and increases with increasing plasma density [111], which is also shown by Fig: 4.7. The elliptical shape seen in figure 4.7 (a) is due to the stronger dephasing of the accelerated electron bunch resulting in more photon emission in the polarization direction of the laser electric field.

For lower density  $\mathbf{n}_{e,2}$ , this behaviour is not pronounced, as the transverse oscillation of the electrons are not strongly affected by the fields of the laser tail due to longer

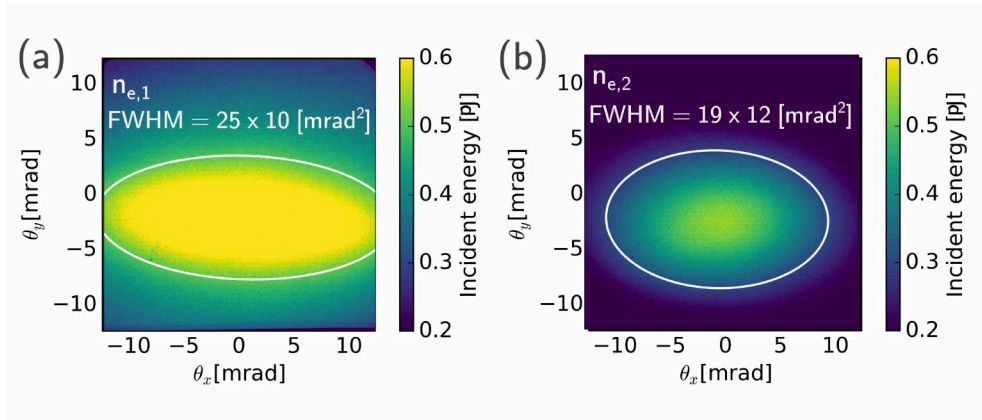


Figure 4.7: 2D Gaussian fitted single shot images for  $\mathbf{n}_{e,1}$  (a) and  $\mathbf{n}_{e,2}$  (b) respectively. The colorbar represents the incident energy in picojoule (pJ). The FWHM divergence was  $25 \times 10$  [mrad<sup>2</sup>] for  $\mathbf{n}_{e,1}$  and  $19 \times 12$  [mrad<sup>2</sup>] for  $\mathbf{n}_{e,2}$ . The laser polarization direction was parallel to the X-axis of the figure. Shadobox detector having sensitivity  $> 10$  keV was used as the betatron detector.

dephasing length (25% longer than  $\mathbf{n}_{e,1}$ ). The wiggling parameter,  $\mathcal{K}$ , also affects the divergence of the betatron beam. Considering similar electron energies were observed for both operating pressure points, a 25% higher  $\mathcal{K}$  for  $\mathbf{n}_{e,1}$  leads to higher betatron beam divergence. The total integrated incident energy recorded for the single shot images shown in Fig:4.7 for the plasma densities  $\mathbf{n}_{e,1}$  and  $\mathbf{n}_{e,2}$  was  $0.6 \mu\text{J}$  and  $0.3 \mu\text{J}$  respectively for incident photons  $> 10$  keV (Detector sensitivity  $> 10$  keV). An increase in  $\mathcal{K}$  for  $\mathbf{n}_{e,1}$  also lead to increase in total photon energy and the angular divergence of the betatron beam in the lasers polarisation direction. This implies the dependence of total photon energy and the angular spread of the betatron beam on  $\mathcal{K}$ . The beam profile for  $\mathbf{n}_{e,2}$  shows greater relative collimation than the beam profile for  $\mathbf{n}_{e,1}$ .

The mean divergence was calculated to be  $\theta_x = 32 \pm 7$  [mrad] and  $\theta_y = 18 \pm 6$  [mrad] for  $\mathbf{n}_{e,1}$  and ( $\theta_x = 19 \pm 5$  [mrad] and  $\theta_y = 13 \pm 2$  [mrad]) for  $\mathbf{n}_{e,2}$ . The mean divergence in  $\theta_x$ , the polarization axis of the laser pulse, was almost 2 time higher for high plasma density ( $\mathbf{n}_{e,1}$ ) while the mean divergence in  $\theta_y$  was only  $\approx 50\%$  higher thus confirming the effect of electron bunch-laser tail overlap during the acceleration process.

To study the pointing stability of the generated betatron beam profile, the centroids of several consecutive betatron beam profiles were plotted for  $\mathbf{n}_{e,1}$  and  $\mathbf{n}_{e,2}$ , as shown in Figure 4.8. In figure, the higher plasma density ( $\mathbf{n}_{e,1}$ ) resulted in strong influence on the betatron beam pointing along the polarization axis of the laser (X-axis in figure). When the plasma density was decreased ( $\mathbf{n}_{e,1}$ ), no such influence was observed.

The mean centroid of the betatron beam profiles was set as the center of the detector

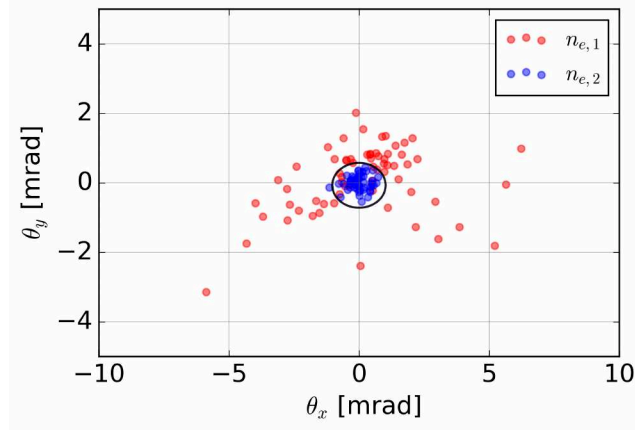


Figure 4.8: Betatron beam pointing fluctuation for high plasma density (red) and low plasma density (blue). For  $\mathbf{n}_{e,1}$ , the fluctuation from the mean peak position was recorded as 2.5, 1.1 [mrad] and for  $\mathbf{n}_{e,2}$  the fluctuation was recorded as 0.4, 0.2 [mrad] in x and y direction respectively.

(0,0) having x-axis deviation of  $\Delta\theta_x = 2.5$  mrad and y-axis deviation of  $\Delta\theta_y = 1.1$  mrad for 68 shots taken for  $\mathbf{n}_{e,1}$ . For  $\mathbf{n}_{e,2}$ , the x-axis deviation was  $\Delta\theta_x = 0.4$  mrad and y-axis deviation was  $\Delta\theta_y = 0.2$  mrad for 49 consecutive shots. The pointing fluctuation was  $6\times$  smaller for  $\Delta\theta_x$  and  $\Delta\theta_y$  for the operating point  $\mathbf{n}_{e,2}$  (lower density). This shows improved pointing fluctuation of the betatron beam profile for the  $\mathbf{n}_{e,2}$  and very strong pointing stability for the betatron beams generated from the ionization injection in the dephasing regime at lower density.

Table 4.2 compares the pointing fluctuation between the electron beam and the betatron beam for both plasma densities  $\mathbf{n}_{e,1}$  and  $\mathbf{n}_{e,2}$ .

	$\mathbf{n}_{e,1}$ [ $9.2 \times 10^{18}(\text{cm}^{-3})$ ]		$\mathbf{n}_{e,2}$ [ $7.5 \times 10^{18}(\text{cm}^{-3})$ ]	
Std. dev. (Pointing)	$\Delta\theta_x$ (mrad)	$\Delta\theta_y$ (mrad)	$\Delta\theta_x$ (mrad)	$\Delta\theta_y$ (mrad)
Electron beam	7.28	6.36	0.65	0.80
Betatron beam	2.5	1.1	0.4	0.2

Table 4.2: Table comparing the standard deviation in the pointing fluctuation of the electron beam and the betatron beam for both plasma densities. It shows that the pointing fluctuation in the electron beam is linearly related to the pointing fluctuation in the betatron beam, as for higher pointing fluctuation in the electron beam at higher plasma density ( $\mathbf{n}_{e,1}$ ), the betatron pointing fluctuation is also higher.

The comparison shows that for higher plasma density the pointing fluctuation is higher for both the electron beam and the betatron beam. A 10X increment in the electron beam pointing fluctuation for  $\mathbf{n}_{e,2}$  resulted in almost 6X increment in

the pointing fluctuation of the resulting betatron beams. This shows an underlying correlation between the pointing fluctuation of the electron beam and the betatron beam.

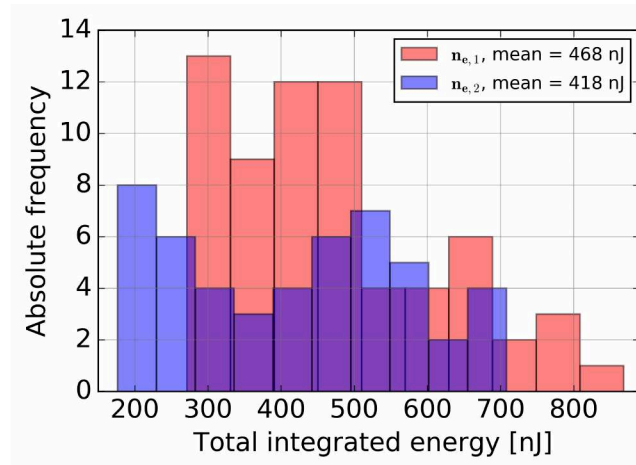


Figure 4.9: The total integrated betatron yield of plasma densities  $\mathbf{n}_{e,1}$  and  $\mathbf{n}_{e,2}$  for photon energy  $> 10$  keV was calculated in nano-joules (nJ). The data sets of figure 4.8 was used to compare the total incident photon energy for both plasma densities. The average photon flux was  $\approx 10\%$  higher for  $\mathbf{n}_{e,1}$  owing to the high plasma density and strong wiggler parameter ( $\mathcal{K}$ ). The standard deviation in photon yield measured was calculated to be around 30%.

After calculating the pointing stability of both plasma densities, comparison of the betatron yield measured for both plasma densities, for a 10 mm gas cell length, was done. For higher plasma density the dephasing and the strength of the wiggler parameter ( $\mathcal{K}$ ) is stronger which leads us to compare the X-ray yield from both plasma densities. In Fig:4.9, the histogram illustrates the total incident energy variation in nanojoules for the same data-sets as Fig:4.8, considering photon energy  $> 10$  keV. The photon flux variation (standard deviation) was measured to be around 30% for both the cases. The mean photon flux was  $\approx 10\%$  higher for  $\mathbf{n}_{e,1}$  as the higher backing pressure implies higher plasma density. This high plasma density leads to smaller dephasing length and a stronger wiggler parameter due to the accelerating electron bunch overlapping with the laser tail and oscillating strongly under the electric field of the driver laser pulse.

### 4.2.1 Reduced gas cell length

To measure the impact of gas cell length on the betatron radiation generated, the gas cell length was reduced to 5 mm from 10 mm while maintaining the same gas mixture

( $H_2(95\%) + N_2(5\%)$ ). A pressure scan was conducted to determine the plasma density at which stable and higher betatron beam yield could be produced. The betatron beam thus produced was compared with the betatron beams from 10 mm gas cell length. Higher plasma density was needed to generate the betatron beam yield comparable to 10 mm gas cell. The data was recorded for the plasma density  $n_{e,3} = 14 \times 10^{18} [\text{cm}^{-3}]$ , which was almost 50% higher than  $n_{e,1}$  and was  $\sim 2\times$  higher than  $n_{e,2}$ .

First the single shot electron spectrum along with the mean electron spectrum over 70 consecutive shots for 5 mm gas cell was compared with the single shot electron spectrum of 10 mm gas cell ( $n_{e,2}$ ). The modulations seen in the 10 mm spectrum is not so much visible in 5 mm gas cell spectrum (Fig:4.10) even though the plasma density is 2X higher. The high plasma density should have resulted in the strong wiggling of the injected electron. The average energy was around 250 MeV similar to the case with 10 mm gas cell. The charge was calculated to be  $246 \pm 20$  pC, a 20% increment over 10 mm gas cell ( $n_{e,2}$ ).

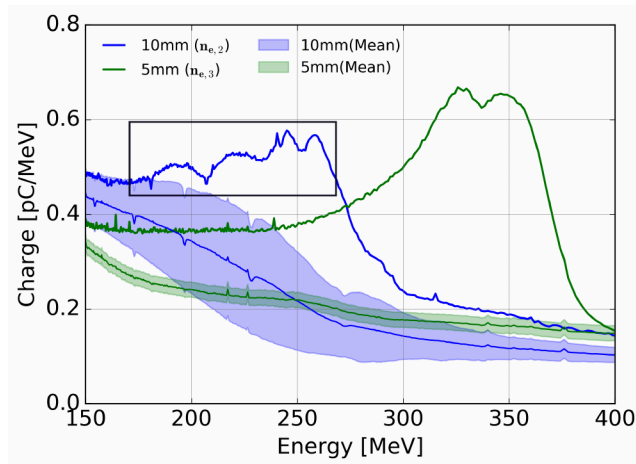


Figure 4.10: Single shot electron spectrum for 5mm gas cell (green), 10 mm gas cell (blue) and mean spectrum over 70 consecutive shots for 5mm gas cell with error (red, shaded). The charge modulation is not significant for 5mm gas cell even at 2X higher plasma density than  $n_{e,2}$ . The average energy was around 250 MeV and the mean charge was  $246 \pm 20$  pC for  $n_{e,3}$ .

Now the angular distribution of betatron beam from 5mm gas cell along with the pointing fluctuation of the beam for 30 consecutive shots at  $n_{e,3} \sim 14 \times 10^{18} \text{cm}^{-3}$  was measured. The divergence (FWHM) of the single shot beam was  $20 \times 10$  (mrad<sup>2</sup>) which was similar to the case  $n_{e,2}$  for 10 mm gas cell. The pointing fluctuation of the beam was  $\Delta\theta_x = 0.5$  mrad and  $\Delta\theta_y = 0.5$  mrad as shown in figure 4.11. The mean incident photon energy for 5 mm gas cell was  $316 \pm 89$  nJ. The mean integrated incident energy for 5 mm gas cell ( $> 10$  keV) was  $\sim 35\%$  lower than best case for

10 mm gas cell ( $\mathbf{n}_{e,1}$ ). This could be due to weaker wiggler strength parameter  $\mathcal{K}$ , evident from no strong modulations seen on the electron spectrum lineout for 5mm gas cell (Fig:4.10).

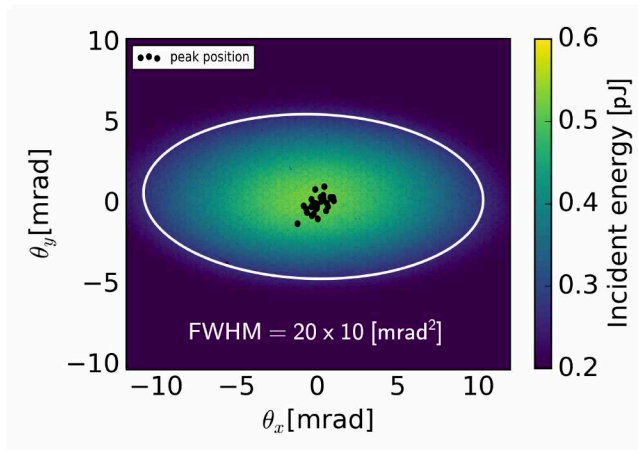


Figure 4.11: Single shot betatron angular distribution overlaid with peak position of 30 consecutive betatron beam profiles for 5mm gas cell length at  $\mathbf{n}_{e,3} \sim 14 \times 10^{18} \text{cm}^{-3}$ . The FWHM divergence after fitting 2D Gaussian profile as  $20 \times 10 \text{ [mrad}^2\text{]}$  similar to the divergence measured for  $\mathbf{n}_{e,2}$  (figure 4.8). The pointing deviation (standard error) was calculated to be 0.5 mrad in both x and y direction respectively. The total incident energy ( $> 10 \text{ keV}$ ) was  $316 \pm 89 \text{ nJ}$ .

Table 4.3 compares the electron beam parameters and the total integrated betatron energy for 5 mm and 10 mm gas cell. The pointing stability of the betatron beam was strongly correlated with the electron beam pointing stability for both the cases. Due to stronger wiggling caused by the overlap of the electron bunch with the laser tail for higher plasma density, the photon yield was seen  $\approx 30\%$  higher for the operating point  $\mathbf{n}_{e,1}$  compared to  $\mathbf{n}_{e,3}$ . The depletion length for 5 mm gas cell length was 0.65 mm leading to the depletion of laser pulse energy after 0.65 mm hence, there was no transverse momentum gain under the affect of the electric field of the laser tail. It was concluded that reducing the gas cell length did not increase the betatron yield and therefore 10 mm gas cell was preferred for further studies.

Gas cell length (mm)	Plasma Density [ $\times 10^{18} (\text{cm}^{-3})$ ]	Mean Electron Energy (MeV)	Mean Electron Charge (pC)	Mean Betatron Energy (nJ)
10	$n_{e,1} = 9.2$	$\sim 200$	$163 \pm 32$	$470 \pm 130$
10	$n_{e,2} = 7.5$	$\sim 200$	$207 \pm 40$	$418 \pm 110$
5	$n_{e,3} = 14$	$\sim 200$	$246 \pm 20$	$316 \pm 89$

Table 4.3: Table comparing electron beam and betatron beam parameters for 5mm and 10 mm gas cell.

The data suggests that if the application demands high X-ray photon yield and high divergence irrespective of the pointing fluctuation then such X-ray source can be obtained at higher plasma density ( $n_{e,1}$ ) for the gas cell length of 10 mm having  $H_2 : N_2, 95 : 5$  as gas target otherwise lower plasma density ( $n_{e,2}$ ) with similar gas cell length and gas mixture should be preferred.

### 4.2.2 Energy spectrum of the betatron beam

To measure the energy spectrum of the X-ray photons emitted by relativistic electrons, Ross pair filters are very useful. In this section, the spectral shape of the betatron beam is characterised using Ross filters.

Using the spectrum analysis method detailed in Chap:3, the energy spectrum of the betatron beam was extracted from the Ross filter images obtained on the detector. The filter array was placed in vacuum and was imaged with the X-ray detector attached to the vacuum chamber. A Ross pair filter wheel imaged on the shadobox detector is shown in figure 4.12 (a). The images are background subtracted.

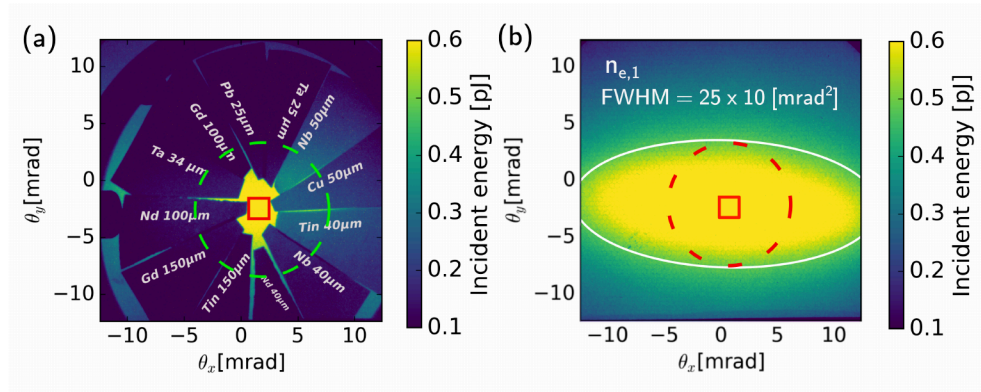


Figure 4.12: Background subtracted Ross filter wheel imaged on the Shadobox detector for 10 mm gas cell length at  $n_{e,1}$  operating point (a) and the betatron beam profile (b). The red square was placed at identical location in (a) and (b) for normalising the signal on the Ross filters.

The filters are arranged in shape of 'pizza slices' having K-edge energies in increasing order in clockwise direction (Fig:4.12 (a)). An area of  $50 \times 50 \text{ pixel}^2$  over each filter inside the green circle was normalised with the area inside the red circle from the spatial distribution of the betatron beam without any filters (Fig:4.12 (b)). This was done because a homogeneous distribution of the beam over each Ross filters is required to calculate actual transmission through the filters. This calculation process can be understood as follows using figure 4.12:

- Let say the mean total count of red square is A in figure 4.12 (b) and when we place this red square on the figure 4.12 (a) we still get A counts which means in both the cases the total peak count is same for the case with no filters.
- Now suppose we move the red square on Tin  $40\mu\text{m}$  in the figure 4.12(a) inside the green dashed circle and calculated the total mean count as C, and then place this red square at exact same location on figure 4.12 (b) and calculated the mean count for this area to be B. Then  $A/B$  is the correction factor which we need to multiply to the C of figure 4.12(a) to get the actual mean count.
- These two steps were repeated for all the filters and thus the counts were corrected for each filter

Using the equation 3.4 and 3.5 for the Ross filter image obtained in figure 4.12(a), we get a plot for fit residual against the energy range of the detector ( $> 10$  keV). The sum of the squares of the residuals, shown in black (Fig:4.13), has a minima at 28.21 keV giving the critical energy for the betatron beam as,  $E_c = 28.21$  keV. The squared residuals of some of the filters is also included for comparison, showing a good agreement with the value obtained. After calculating the critical energy, the power and number spectrum was calculated.

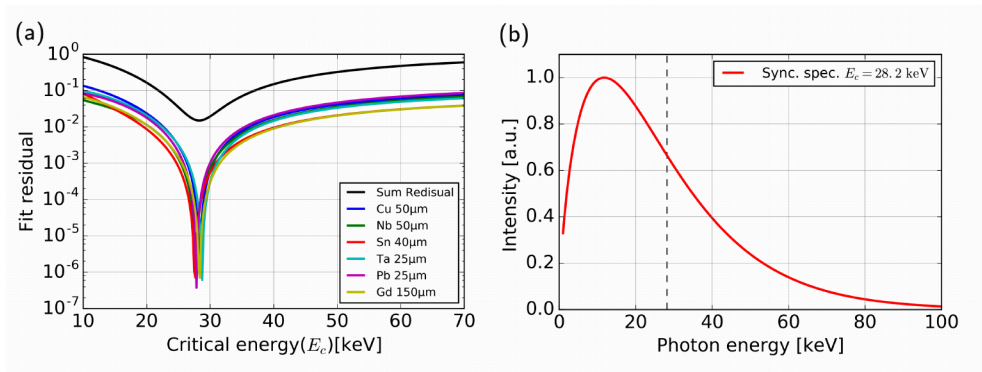


Figure 4.13: (a): The sum of squared residuals (black) and residuals of some of the Ross filters used (colours) for the single shot image. The critical energy was the minima of the sum of the squared residuals (black),  $E_c = 28.2$  keV. (b) Using the critical energy obtained by fit-residual method, the reconstructed normalised synchrotron spectrum was plotted and the spectrum peaks at 11.2 keV.

The normalized betatron spectrum obtained in figure 4.13 (b) for  $E_c = 28.2$  keV was unfolded with the detector efficiency and the transmission efficiency of the materials in the betatron beam propagation path. The betatron beam passed through  $30 \mu\text{m}$  Al,

100  $\mu\text{m}$  Mylar and 2  $\text{mm}$  carbon before reaching the detector, excluding the Ross pairs. From figure 4.12(b), we calculate the total incident energy on the detector, ( $E_{inc.}$  [keV]), by integrating the total number of counts and using 6.17 Counts/keV to convert the incident energy from counts to keV. Now we integrate the unfolded spectrum in energy limits 10-100 keV, ( $E_{norm.}$  [keV]). Then we take the ratio of ( $E_{inc.}$  [keV]) and ( $E_{norm.}$  [keV]) and multiply it with the normalised spectrum. This product was the power spectrum ( $dI/dE$ ). The power spectrum is related to the number spectrum as  $dI/dE \propto E dN/dE$  and thus the number spectrum was calculated for the single shot image shown in 4.12(a). The corrected number spectrum for a single shot (Fig:4.12(a)) is shown in figure 4.14 (a). The shaded region is the standard deviation obtained over 30 consecutive shots for the plasma density  $\mathbf{n}_{e,1}$ . The absolute number of photons obtained from Ross filters are shown with black dots. The y-error in measured number of photons/keV/shot is the standard deviation and the x-error is the spectral width of the of the Ross pairs used. Mean critical energy for high plasma density ( $\mathbf{n}_{e,1}$ ) was calculated to be  $30.2 \pm 5$  keV and  $16.9 \pm 2$  keV for low plasma density ( $\mathbf{n}_{e,2}$ ) for gas cell length of 10 mm (Fig:4.14(b)). This results in 10X more photons for  $\mathbf{n}_{e,1}$  than  $\mathbf{n}_{e,2}$  at energies  $>50$  keV.

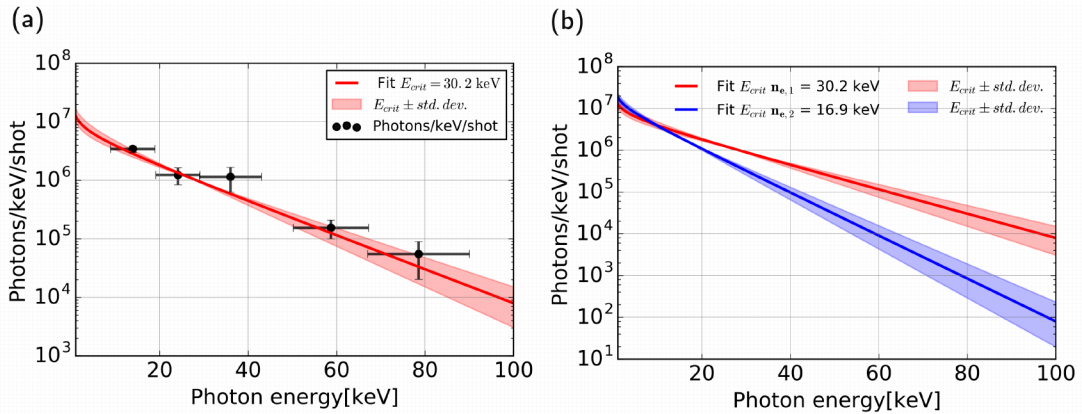


Figure 4.14: (a): The number spectrum ( $dN/dE$ ) with mean critical energy calculated for plasma density  $\mathbf{n}_{e,1}$  over 30 consecutive shots was  $E_{crit} = 30.2 \pm 5$  keV (red [solid line, shaded]). The absolute number of photons/keV/shot calculated from the Ross pairs (black circle) plotted shows good agreement. (b) The mean reconstructed number spectrum for  $\mathbf{n}_{e,1}$  and  $\mathbf{n}_{e,2}$  are compared and the standard deviation was measured over the respective data sets for both plasma densities having 30 and 33 images respectively.

As the wiggler strength parameter ( $\mathcal{K}$ ) was strong due to higher plasma density and hence shorter dephasing length for  $\mathbf{n}_{e,1}$ , this resulted in a  $\sim 75\%$  higher critical energy

for this case (Fig:4.14 (b)). For  $n_{e,2}$  although the pointing stability of the betatron beam is almost 10 times better than the  $n_{e,1}$ , the critical energy is lower due weaker influence of wiggler strength parameter at lower density. The error calculated is the standard deviation for 30 and 33 consecutive images in the data sets of the plasma densities  $n_{e,1}$  and  $n_{e,2}$ .

After finding the betatron spectrum, one can also calculate the peak brightness of the source. For this, the betatron beam was assume to have a pulse duration of 10 fs. The peak brightness for both the case was of the order of  $\approx 10^{22}$  photons/s/mm<sup>2</sup>/mrad<sup>2</sup>/0.1%BW, which is comparable with the X-ray brilliance available in the latest generation of synchrotrons [112, 113].

To summarise this section, the critical energy recorded for the two different plasma density for a 10 mm gas cell length having gas mix ( $H_2(95\%) + N_2(5\%)$ ) was  $E_{crit} = 30.2 \pm 5$  [keV] for  $n_{e,1}$  and  $E_{crit} = 16.9 \pm 2$  [keV] for  $n_{e,2}$ . For single stage laser wakefield acceleration and having a laser system with  $\sim 200$ TW peak power, the critical energy achieved during this campaign is comparable to the results achieved at other laser facilities [37, 88].

### Source size measurement

For the rough estimation of the source size, that can be done during the experiments, the shadowgraphic image of the object in the betatron beam path can be used. In this section, we will first estimate the source size of the betatron beam using geometrical analysis and then for more precise measurement we will use Fresnel diffraction method (Sec:3.3.2). If the image of the back-lit object is visible on the detector with good enough contrast, we can safely assume that source size is similar to the object dimensions and cannot be larger [46]. The experimental setup used for measuring the source size is shown in the figure 4.15.

The backlit objects were tungsten wires of 10  $\mu$ m and 50  $\mu$ m thickness placed 21 cm from the betatron source and the X-ray detector (ANDOR CCD) was placed 230 cm from the source. The backlit objects and the razor blade were placed on a translational stage to move in and out of the betatron beam path when required. The magnification obtained on the X-ray CCD detector was 10.95. The radiograph shows the single shot image for the backlit objects and the razor blade. The 10  $\mu$ m tungsten wire is visible with good contrast implying that the source size is  $< 10$   $\mu$ m.

The average lineout over 200 pixels for a radiographic image of razor blade is shown in picture. The first diffraction overshoot (dotted green circle) happens just before the blade edge as for X-ray wavelengths ( $\sim$  nm) contained in the betatron beam the

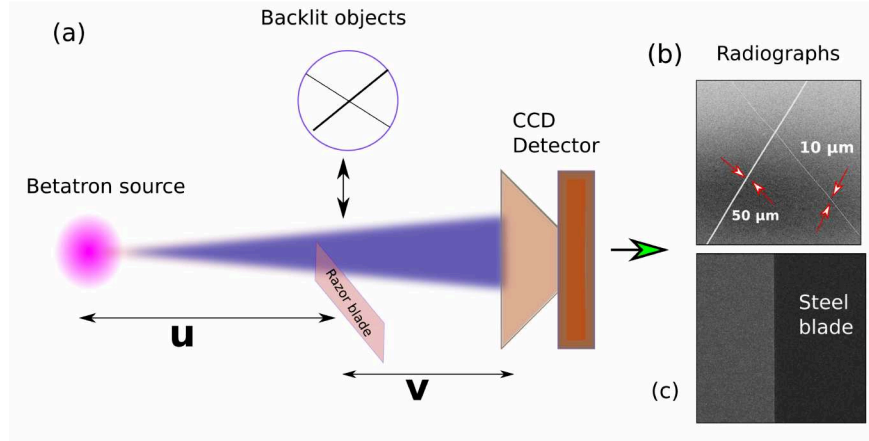


Figure 4.15: The experimental set-up to measure the source size of the betatron beam from LWFA using ionization injection scheme. The backlit objects were tungsten wires of  $10\ \mu\text{m}$  and  $50\ \mu\text{m}$  thickness. The backlit objects were at a distance of 21 cm from the source. The ANDOR CCD was placed 230 cm from the source providing a magnification of 10.95. The radiographs shows the images of backlit objects obtained on the X-ray detector.

blade edge is infinitesimally thin thus they get diffracted. It is shown in literature that greater the first overshoot, smaller is the source size [83]. Due to tapered shape of the razor blade, the error-fit function (Fig:4.16) deviates just after the blade edge as shown by the dotted rectangle (The error function represents the ideal blade). In region 3 the betatron signal is transmitted through the homogeneous thickness of the razor blade. Due to high critical energy ( $> 25\ \text{keV}$ ), some part of the spectrum transmits through the razor blade and therefore the betatron signal intensity does not drop completely to zero in the blade region. Using equation 3.1, 3.2 and the magnification of 10.95, the source size using error-fit was  $2.25 \pm 0.26\ \mu\text{m}$  for the single shot image presented in the figure 4.16. The error fit is also an approximation as the deviation produced by the lineout cannot be fitted with the error-function.

To get more precise measurement of the source size, we use Fresnel diffraction method (Sec: 3.3.2) by placing a half plane (razor blade) in the betatron beam path. A typical intensity distribution on the detector looks like a half shadow (Fig: 4.16), whose details are a convolution of information about the x-ray source and half plane. To extract the source size information from this convolution, we first model the expected diffraction pattern for various sources for the critical energy calculated during this experiment ( $\sim 30\ \text{keV}$ ). We model the diffraction pattern for a monochromatic point source, poly-chromatic point source and also for a source with Gaussian transverse profile having  $1\ \mu\text{m}$  waist. It was observed that the point source emitting synchrotron

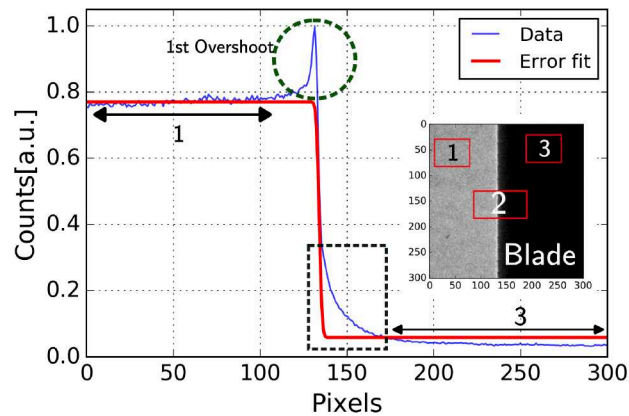


Figure 4.16: The average lineout over 200 rows of the razor blade radiograph (inset) obtained on the X-ray detector is fitted with a straight edge (error-fit). The source distribution is assumed to have a Gaussian shape. With magnification of 10.95, the source size obtained using error-fit was  $2.2 \pm 0.2 \mu\text{m}$  for the single shot image (inset).

radiation and the Gaussian source emitting synchrotron radiation have all intensity oscillations except the first one washed out due to the superposition of the diffraction fringes generated by photons with different energies. With a finite source size, the rising slope of the first overshoot becomes even smoother.

The inset of figure 4.18 shows a radiograph of the razor blade produced on the X-ray detector by the betatron beam. Integrating the betatron beam intensity along the direction of the blade edge gives the experimental data shown in figure 4.18 (black squares), which was normalised to the beam intensity in the transparent (blade free) region. The observed higher overshoot peak in the normalized experimental data compared to the overshoot peak for a point polychromatic source (Fig: 4.17) suggests an interesting phenomenon. The assumption is that the experimental overshoot results from X-ray refraction in the razor blade part. Due to the tapered profile of the blade, with a few microns thick apex, certain photons can penetrate the obstacle and get deflected towards the blade-free area. The deflected photons then overlap with the diffracted photons, giving rise to the observed intensity overshoot. Since the model shown in figure 4.17 was designed for an ideal knife-edge having 100% absorption, the attempt was made to fit the profile instead the amplitude of the intensity overshoot observed in the experiment. All the fit magnitudes were adjusted to have the same maximum value as the experimental one. All the fit curves on the blade side are lower than the experimental data due to the photons not being completely absorbed by the blade owing to their higher energy. The rising slope of the first overshoot of the

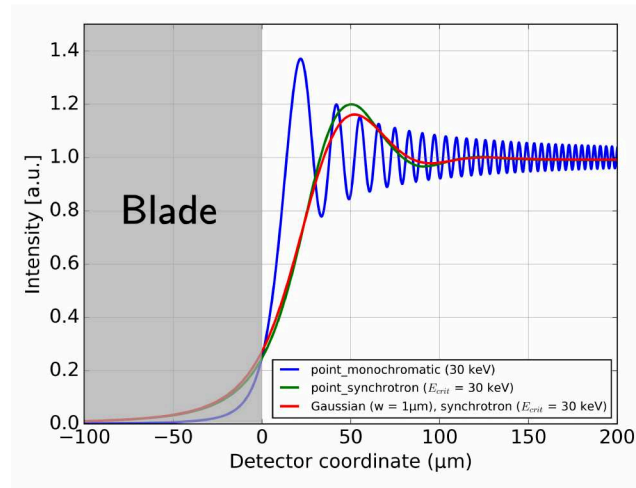


Figure 4.17: The modeled intensity profiles of Fresnel diffraction for different sources. The distance between the source and the half-plane (blade) was 21 cm and the distance of the detector plane from the half-plane was 230 cm.

experimental data follows the model with source size as  $1 \mu\text{m}$  and  $2 \mu\text{m}$  quite closely and the falling slope lies in between them. We can therefore tentatively conclude the X-ray source has a Gaussian distribution with  $1/e^2$  intensity size between  $1 \mu\text{m}$  and  $2 \mu\text{m}$ . This was case for both the plasma densities  $n_{e,1}$  and  $n_{e,2}$  concluding no significant effect of stronger wiggling parameter ( $\mathcal{K}$ ) on the betatron beam size. The small source size of the betatron source could used to image features within a sample up to few microns resolution.

### 4.3 Summary

With the aim to improve and optimise a laser-based X-ray source, it was demonstrated that using a 10 mm gas cell with  $H_2 : N_2(95 : 5)$  as the gas mixture, synchrotron-like X-ray beams can be produced with critical energy around 30 keV. The dephasing of the trapped electron bunch increased the betatron wiggler strength parameter  $\mathcal{K}$  and thus the critical energy and photon flux was increased. Reducing the gas cell length or the plasma density results in lower critical energy but improves the pointing stability of the betatron beams at constant laser energy. However, the pointing fluctuation of the betatron beam was always smaller than the single shot betatron beam divergence. The greater shot-to-shot reproducibility coupled with micron source size and high critical energy is promising for various applications such as ultrafast pump-probe study, phase contrast imaging, micro-tomography [37, 88, 114].

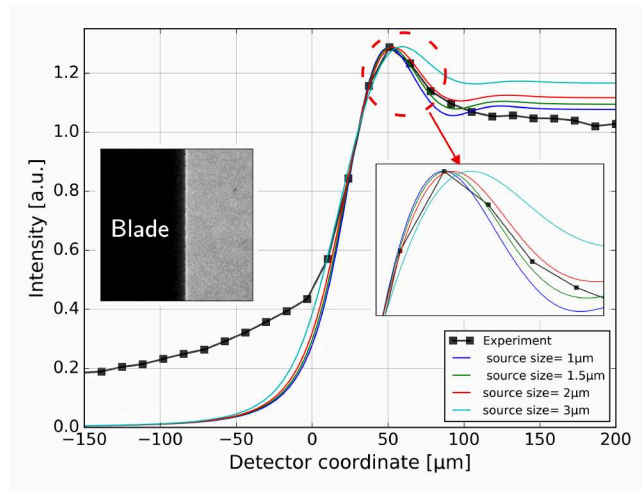


Figure 4.18: The experimental mean lineout of the razor blade over 200 pixels along the blade edge (black squares) plotted with the calculated Fresnel models having critical energy  $\sim 30$  keV and various source size (solid colors). The experimental data lies between the calculated Fresnel model profile of  $1 \mu\text{m}$  and  $2 \mu\text{m}$  and follows the  $1.5 \mu\text{m}$  profile. The distance between the source and the half-plane (blade) was 21 cm and the distance of the detector plane from the source was 230 cm.

# 5 Quasi-monoenergetic Electron Beam and Betatron Radiation

The key element for the stability of the electron acceleration is the injection of background plasma electrons into the plasma wave. As the self-injection scheme is highly non-linear with the laser intensity where even small local fluctuations leads to big instabilities [76], another method for controlled injection of the electrons into the wakefield bubble was tested at JETi200 laser system. This section will present the results of the shockfront injection scheme which is less dependent on the laser intensity and could produce quasi-monoenergetic electrons. The X-rays emitted from these quasi-monoenergetic electron bunches will be diagnosed. Furthermore, the results of a novel experimental technique is presented which aimed to increase the betatron yield hence produced from this injection mechanism.

## 5.1 Shock-front Injection

To achieve controlled trapping of the injected electron bunch, at JETi200 laser system, we modified our gas target (5mm jet) with shock engineering to suppress self injection while still exciting an intense wake structure using shock-front injection method. A shock is created when a supersonic flow encounters an obstruction that turns the flow into itself and compresses it. In this case, a blade placed in the gas jet creates a subsonic region upstream of the blade and is re-expanded. The boundary of higher density is inclined with respect to the main jet axis. The longitudinal plasma density profile of the jet+blade assembly could be represented as Fig:5.1. The modified gas target has density up-ramp(1), sharp density down-ramp (L) and then a density plateau region as shown in figure 5.1.

In the up-ramp region (1) the laser pulse self-focuses and increases in energy, in the steep density drop region (L) the plasma wavelength increases and this causes the wake bubble to expand which lowers the trapping threshold of the background plasma electrons. In region (2), the bubble expansion stops and the injection is terminated due to the slowly varying density and the trapped electrons are accelerated until the laser depletion. This method results in a highly localized injection and produces quasi-monoenergetic electrons. If the experiment is not limited by dephasing or depletion effects, electrons are accelerated from the density transition until the end of the gas jet.

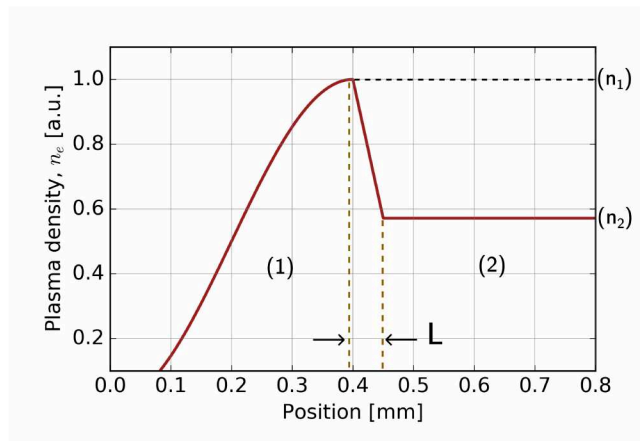


Figure 5.1: The longitudinal density profile created by the modified gas target (Jet+Blade) with up-ramp region (1), a sharp down-ramp density transition of  $(\Delta n = n_1 - n_2)$  and the density plateau (2).

### 5.1.1 Electron Beam Measurements

To create a shock, a commercial razor blade was placed on top of the nozzle of the supersonic gas jet and was motorized to move in the laser propagation direction, the transverse directions and also was able to rotate on the axis of the gas jet nozzle (Fig: 5.2). The laser was focused into the disturbed flow a few 100 micron above the gas nozzle. With  $a_0 \approx 3$  and plasma density around  $4 \times 10^{18} \text{ cm}^{-3}$ , the gas jet produced electrons via self-injection mechanism.

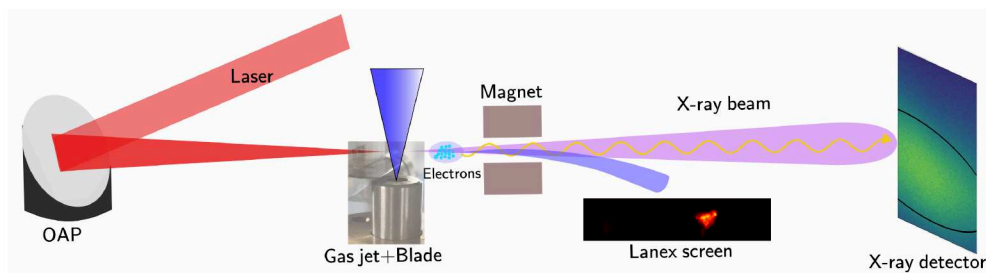


Figure 5.2: The jet+blade assembly used to create sharp density transition. The blade could be moved left to right to change the coverage of the gas jet exit nozzle, rotated in a plane perpendicular to gas exit direction and moved transversely to the laser propagation axis (left to right). It was placed on top the gas nozzle covering 30% (best results) of the 5 mm nozzle. The acceleration length was around 3.5 mm

A transition from self-injection to shock-injection was made to suppress self-injection induced electrons in the wakefield bubble. Initially, when the ultra-high intensity laser was focused on the gas jet without blade, the electrons were injected via self-injection.

Therefore, to suppress the self-injection the backing pressure (plasma density) was decreased until there was no signal on the Lanex screen. The laser still generated a non-linear wakefield but due to low plasma density, the electrons were not getting trapped. Once the blade was introduced it created a sharp density gradient which kick-started the acceleration process again (Fig: 5.3).

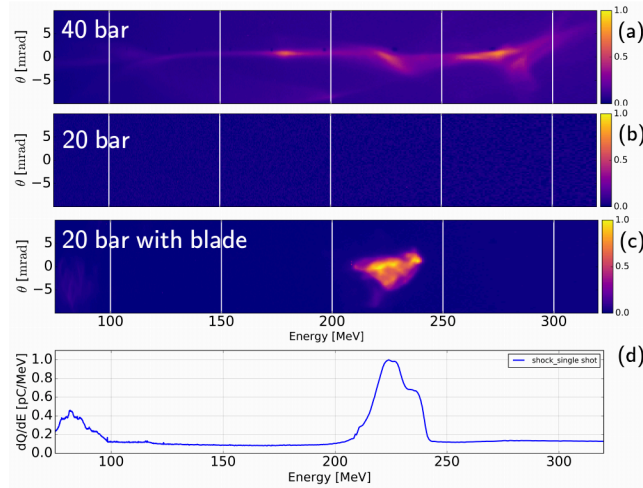


Figure 5.3: Electron spectrum for the transition from self-injection to shock-front regime for a 5mm nozzle gas jet. (a) The electron beam measurement without blade at 40 bar backing pressure ( $\approx 4 \times 10^{18} \text{cm}^{-3}$ ). (b) No electron signal for reduced backing pressure of 20 bar ( $\approx 2 \times 10^{18} \text{cm}^{-3}$ ). (c) The recorded quasi-monoenergetic beam after introducing the razor blade covering 30 % of the 5mm exit nozzle at 20 bar backing pressure. (d) The lineout of (c) gives peak energy of 220 MeV and the rms spread for this shot was 19 MeV (1/e) which gives  $\frac{\Delta E}{E} < 10\%$ .

Now we start analysing the quasi-monoenergetic electron beam thus recorded on the electron diagnostic screen. The blade coverage scan showed the best results (70 % shots of the data set produced best quasi mono-energetic electrons) at 30 % blade coverage which was in line with the literature [6]. One such electron beam produced is shown in the figure 5.3 (20 bar). Figure 5.4 (Left, gray), shows the electron spectra from a data-set containing shots from a single run, where the data points having no electrons were excluded. The mean spectra (red) for the data-set shows a low energy spread of  $< 10\%$  around the mean energy of 220 MeV. For this data-set containing 47 shots, the mean charge was calculated to be  $34.8 \pm 17$  pC and the divergence was  $< 10\%$ . The pointing fluctuation was greater than the pointing fluctuation of the gas cell (ionisation injection) most likely due to sharp density transition as compared to homogeneous density distribution in gas cell.

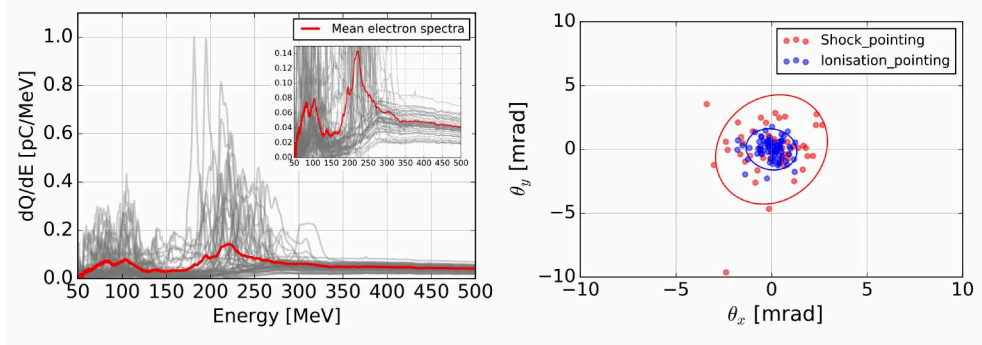


Figure 5.4: (Left): Electron beam spectrum (grey) from a single data-set showing the fluctuation in peak energy and narrow energy spread around the peak energy confirming quasi-monoenergetic electron beams from shock-front injection mechanism. The mean energy spectra (Inset, red) shows 2X more charge/MeV for mean peak energy than the lower energy end of the spectrum. (Right) The pointing fluctuation compared with the electrons produced from gas cell (ionisation injection). The confidence ellipse contains 95% of the data points.

### 5.1.2 Betatron Beam Measurements

After producing quasi-monoenergetic beams successfully, we then measured the betatron radiation generated from such beams. We measured the angular beam distribution, energy spectra of the X-ray beams from the localised injection of the electrons using the same experimental methods as used in section 4.1. In this section we will evaluate the betatron beam generated from the shock-front injection mechanism.

The angular distribution of the betatron radiation from shock-front injection was measured by placing ANDOR CCD 2.3 m from the gas target. The measured angular deviation (FWHM) for a single shot was  $21 \times 6 \text{ mrad}^2$ , where the X-axis is in the laser polarization direction. To characterise the betatron energy spectrum a set of Ross filters was placed 200 cm from the source in vacuum (30 cm in front of the CCD)(Fig:5.5).

Furthermore, the betatron energy spectrum and the source size of the beam thus generated was calculated. For measuring the spectrum the Ross pair method (refer Sec: 3.3.3) was used. Andor CCD with  $50 \mu\text{m}$  Beryllium window in front of the CCD was utilized as the X-ray detector. The Beryllium window put a cut-off on the photon energy reaching the detector ( $> 1 \text{ keV}$ ). An analysis approach similar to Sec:4.2.2 was taken to reconstruct the betatron spectrum from the recorded Ross pair data. The critical energy for a single shot image was calculated to be around 10 keV (Fig: 5.6). Due to lack of statistics for the betatron beams measured using shock-front injection

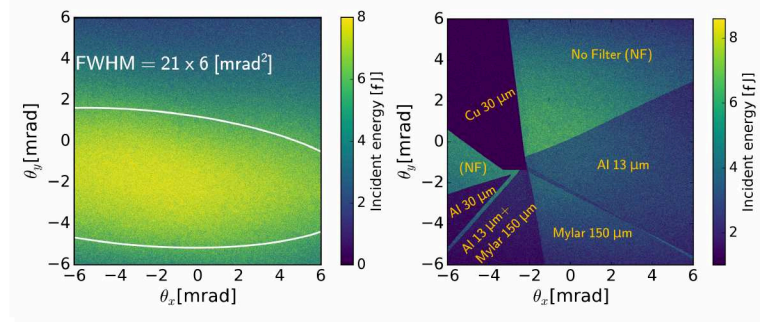


Figure 5.5: (a): The angular distribution of the X-ray beam generated by using the shock-front injection in LWFA was measured to be  $21 \times 6$  mrad<sup>2</sup> for a single shot image. The laser polarization is in the direction of the x-axis of the image ( $\theta_x$ ). (b) The Ross filters used to characterize the energy spectrum. Due to weak signal level obtained on the CCD as compared to the ionization injection, the filters used were changed from Ross filter pairs to individual Ross filters. The images are background subtracted.

scheme, a standard error could not be provided but was estimated to be around  $\sim 50\%$ . The total number of X-ray photons above  $> 1$  keV was estimated to be  $\sim 10^7$ . The critical energy and the number of photons obtained by shockfront injection scheme was lower than the ionization injection scheme due to two reasons. First, the critical energy of the betatron spectrum is dependent on the electron peak energy and plasma density. As the peak energy was similar for both the cases, the reduced plasma density for the case of shockfront injection resulted in reduced critical energy. Also, there was no dephasing as the dephasing length was greater than the acceleration length. The electrons did not catch up to the laser tail and gained transverse momentum by wiggling under the influence of the laser's electric field.

To measure the source size back-lit objects, 10  $\mu\text{m}$  and 50  $\mu\text{m}$  Tungsten wires and a commercial razor blade, were used. The radiographs shown in the fig 5.7b and 5.7c illustrates the projection of the wires and the Fresnel target on the CCD chip of the camera. In the radiographs, a diminished contrast would result from a source larger than the backlit objects or an isotropic radiation background, whereas the presence of multiple sources would give rise to the casting of multiple shadows. The 10  $\mu\text{m}$  tungsten wire can be clearly seen on the CCD detector with good enough contrast showing the presence of none and provides an upper limit for the X-ray source size being  $< 10$   $\mu\text{m}$ . Using the analysis method for source size as mentioned in (Sec:3.3.2), we take an average lineout of the radiographic image obtained on the X-ray CCD Detector, after doing background noise subtraction from the raw image. We fit the obtained lineout with the error function to retrieve the source size of the betatron

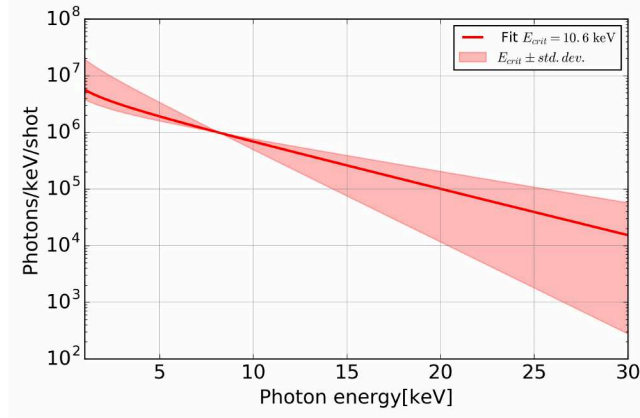


Figure 5.6: The reconstructed betatron spectrum from the Ross filters for a single shot image for the shock-front injection method shows a critical energy,  $E_c$ , of 10.6 keV. There was 50% error in the critical energy (shaded region) arising mainly from high electron beam charge variance. Andor CCD was used as the X-ray detector.

beam produced from quasi-monoenergetic beam. With a magnification of 5.4, the source size for a single shot was calculated to be  $5.5 \pm 0.2 \mu\text{m}$ .

For precise measurement of the source size, we do Fresnel diffraction analysis (ref.4.2.2). The Fresnel diffraction model had convoluted information of the synchrotron spectrum with 10 keV critical energy and the X-ray source having Gaussian distribution. The Fresnel models with different source size ( $1 - 4 \mu\text{m}$ ) was plotted against the experimental data 5.8. The model assumes 100% photon absorption in the blade region however, that was not the case. The high background noise would have an effect on the mean lineout plotted for the experimental data. Due to the deflection of the X-ray photons by the tapered profile of the blade edge into the blade free region and the high background, the peak intensity of the experimental data is higher than expected. Hence, all the fit magnitudes were adjusted to have the same maximum intensity and an attempt to fit the rising and/or falling slope of the fit profiles was made. The source size measured was less than  $5 \mu\text{m}$  as the first fringe width of the Fresnel model ( $5 \mu\text{m}$ ) is larger than the experimental data. The Fresnel model with source size  $3 \mu\text{m}$  matches the rising slope and falling slope of the experimental data quite closely. It can be tentatively said that the source size was around  $3 \mu\text{m}$ . The relatively larger source size than the ionisation injection could be due to the off-axis injection of the electrons for the shock-front injection mechanism.

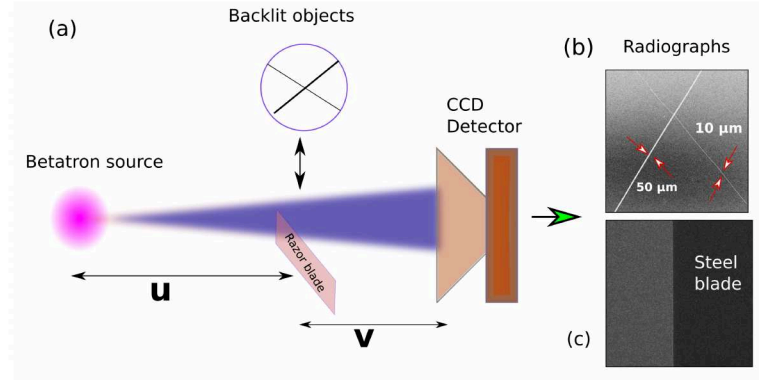


Figure 5.7: The setup used for radiography and Fresnel diffraction includes the betatron source, backlit objects and the X-ray CCD as shown in (a). The accelerated electrons from the LWFA were deflected by a magnet (not shown) before the backlit objects for imaging. (b) The radiograph shows mesh of tungsten wire with thickness  $10\ \mu\text{m}$  and  $50\ \mu\text{m}$ . (c) The steel blade used for source size estimation using error fit and the Fresnel diffraction.

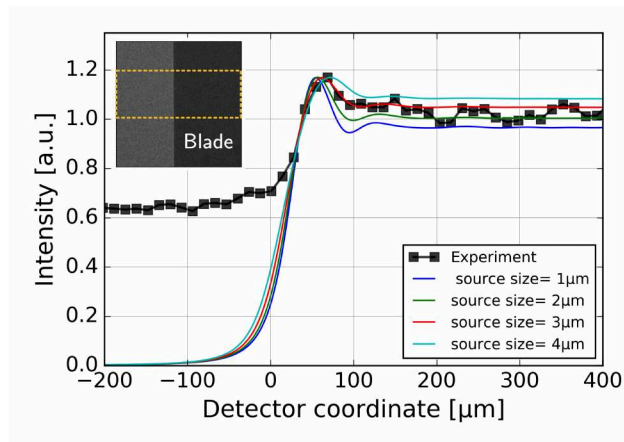


Figure 5.8: The figure shows lineout of the radiographic image of a commercial razor blade as knife edge (inset) and the Fresnel models for various source size with synchrotron spectrum having critical energy  $10\ \text{keV}$ . The rising and falling slope for the source size  $3\ \mu\text{m}$  matches quite closely with the experimental data. All the fit magnitudes were adjusted to have the same maximum intensity as the blade was not an ideal knife-edge. The signal in the blade free region is only  $2\times$  the signal in the blade region (ideally should be zero) implying high background signal.

In conclusion, the shockfront injection campaign resulted in the quasi-monoenergetic electrons having  $\approx 220\ \text{MeV}$  peak energy with  $\frac{\Delta E}{E} < 10\%$  for a gas jet having  $5\ \text{mm}$  nozzle and the blade coverage of  $30\%$ . The mean charge was measured to be  $34.8 \pm 17\ \text{pC}$  and the divergence was reported to be  $< 10\ \text{mrad}$  for the Helium gas target. The resultant betatron beam had the critical energy of  $\approx 10\ \text{keV}$  for a single shot image

with around 50% uncertainty over the whole campaign due to unreliability in the electron generation and high variance in the electron beam charge ( $\sim 50\%$ ). The source size was measured to be around  $3 \mu\text{m}$  with the uncertainty arising from the high background signal and non-ideal knife edge. With  $3 \mu\text{m}$  source size,  $21 \times 6 \text{ mrad}^2$  angular spread and assuming 10 fs pulse width the peak brilliance was calculated to be  $\sim 10^{20}$  photons/s/mm<sup>2</sup>/mrad<sup>2</sup>/0.1%BW.

## 5.2 Betatron Beam Enhancement using Shock-Front Rotation

After conducting measurements on the X-ray beam properties produced from shock-induced electrons in LWFA, a subsequent evaluation was performed to examine the influence of shock-front rotation on the yield of X-ray photons. It is well-established that the betatron beams arise from the transverse oscillation of the trapped electron bunch [37]. By introducing controlled rotation of the shock-front, generated by the jet+blade assembly, we hypothesized an increase in the transverse oscillation amplitude ( $r_\beta$ ) of the injected electrons. This increase in amplitude  $r_\beta$ , will then increase the number of X-ray photons produced by increasing the betatron beam divergence (Eqn.2.45). In this section, we will delve into the electron beams and the resulting betatron beams produced at various angles of shock-front rotation and will do a 2D PIC simulation using the experimental parameters to qualitatively compare the results obtained.

### Electron and Betatron Beam Measurements

The shock-front, formed using a Jet+Blade assembly, was subjected to rotation at different angles within a plane perpendicular to the gas nozzle. In order to study and analyze the electron beam profile, a LANEX screen was placed at a distance of 90 cm from the target. To perform electron spectrum measurements, a permanent magnet was applied to modify the LANEX screen to function as a spectrometer as well. There was a high degree of fluctuation in the data for higher angles of shock-front rotation.

The reproducibility of the stable electron beam suffered heavily with changing the angle of shock-front rotation, indicating high sensitivity of shock-front rotation towards the wakefield acceleration parameters (plasma density, laser pulse front tilt, laser pointing). The background seen on the  $60^\circ$  (Fig:5.10) are the electron being sprayed all over the screen showing the electrons trapped in the first bubble experiencing different acceleration gradient.

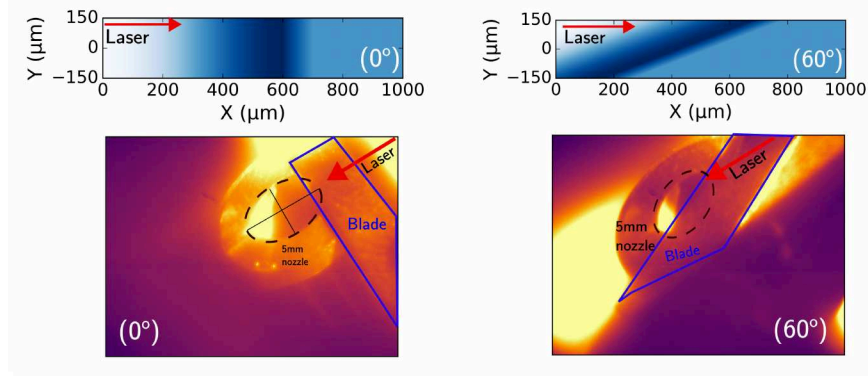


Figure 5.9: The longitudinal density profile used for 2D PIC simulation (top) and the experimental configuration to achieve similar profile (bottom) for  $0^\circ$  and  $60^\circ$  shockfront rotation angles.

To maintain consistent injection points during the varying shock-front rotations, a CCD camera was employed to capture images of the plasma channel resulting from the laser-plasma interaction. The imaging setup had a resolution of  $100 \mu\text{m}$ . To focus on the specific region of interest (ROI) surrounding the plasma channel, the shock-front was adjusted in parallel to the blade edge direction for each rotation, ensuring that the plasma channel always remained within the designated ROI. Throughout all the measurements, the height of the razor blade and its coverage in relation to the nozzle of the 5 mm gas jet were kept constant to ensure reproducibility and consistency in the experimental setup. Figure 5.10 shows the best single shot images for the datasets corresponding to  $0^\circ$ ,  $30^\circ$  and  $60^\circ$  angles of shock-front rotation. It could be seen that the peak energy is increasing along with the increase in the rotation angle. This could be due to the increase in the acceleration length, as increasing the rotation angle could also increase the acceleration length for the injected electrons. However, the single shot image should not be enough to show complete picture and we could not get statistics with multiple images due to poor reliability of the electron spectrum.

Afterwards, the betatron beam images obtained from the Andor CCD for the electron shots corresponding to the figure 5.10 were examined. When analyzing the results, it was observed that the betatron beam divergence and photon flux showed minimal variation for the shock-front rotation angles of  $0^\circ$  and  $30^\circ$ . However, for the case of a  $60^\circ$  shock-front rotation angle, both the beam divergence and photon flux exhibited an increase. This change may be attributed to the concurrent increase in the injected charge and also higher oscillation amplitude as the electrons are now being injected from a higher off-axis angle. It is important to note that the critical energy for all the cases remained within the range of 7 – 11 keV. However, due to significant fluctuations

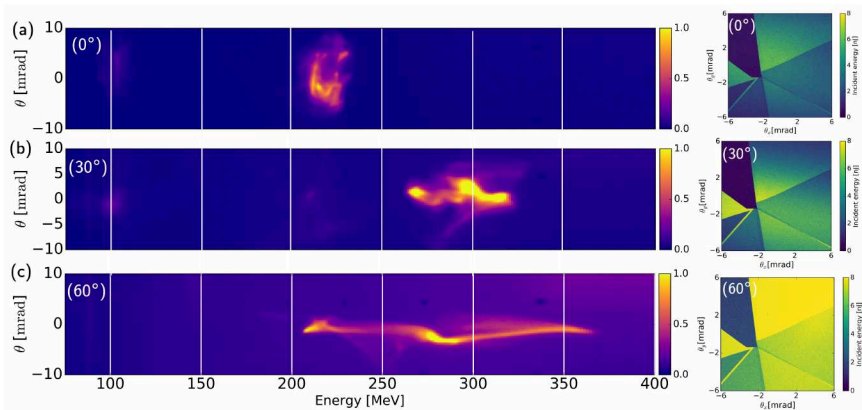


Figure 5.10: Figure shows the electron spectrum and the respective X-ray CCD image for  $0^\circ$ [Top],  $30^\circ$ [Middle] and  $60^\circ$ [Bottom] angle of shock-front rotation. These single shots are the best images from the data-sets taken for respective rotation angles. The measured divergence of the analysed data-shots was  $< 10$  mrad and the peak energy was in between  $250 - 350$  MeV. (Right panel): The corresponding betatron beam with Ross filters imaged on X-ray CCD. The beam divergence and photon flux remained fairly similar for  $0^\circ$  and  $30^\circ$  while it increased for the case of  $60^\circ$  angle of shock-front rotation. The critical energy,  $E_c$ , was  $\approx 9$  keV for all the three cases.

in the data collection process for the rotating shock-front data-set, it was not feasible to calculate a statistical value for the betatron beam parameters. Therefore, the figure 5.11 represents the best single-shot data available for the analysis.

Furthermore, we were investigating the betatron yield for various shock-front rotation angles. Our objective was to determine whether the observed increment in the photon flux can be attributed to an increase in the transverse oscillation of the injected electron. To achieve this, we computed the ratio of the betatron beam flux (CCD counts) to the product of the mean electron beam energy and the electron charge. This ratio will provide valuable insights into the relationship between the shock-front rotation angles and the effect on the transverse oscillation of the injected electron.

Additionally, to conduct a comparative analysis of the charge (total integrated counts) and the mean weighted energy for different rotation angles, we plotted data from 10 good shots extracted from each data-set corresponding to the respective angle of rotation (Fig: 5.12). Notably, in the case of a  $60^\circ$  rotation angle, the total integrated charge exhibited an increase, which can be attributed to the possibility of a longer ramp and, consequently, a longer injection time. These factors may have influenced the observed variations in the total integrated charge and the mean weighted energy among the different rotation angles.

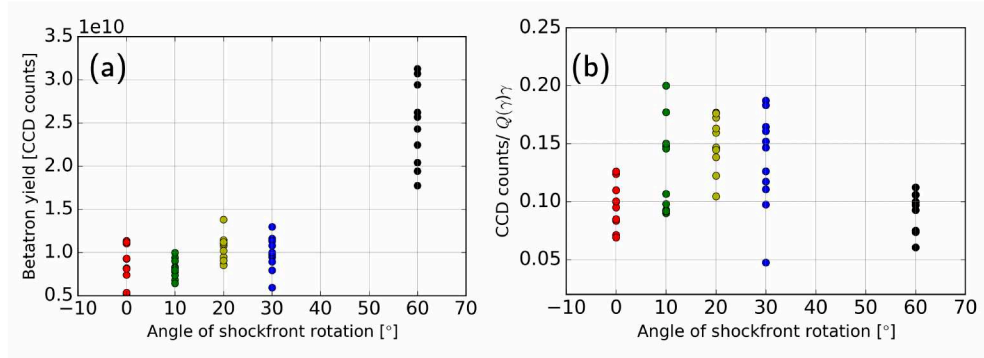


Figure 5.11: (a) The plot shows the variation of the total integrated X-ray CCD counts against the shock-front rotation angles. An increase in the photon flux for the case of  $60^\circ$  shock-front rotation angle. For the rotation angle  $40^\circ$  and  $50^\circ$ , due to experimental limitation the data was not collected. The dots correspond to the single shot data for the data-set. (b) The betatron yields were subsequently normalized with respect to the electron beam energy ( $\gamma$ ) and charge ( $Q[\gamma]$ ).

In the investigation, it was observed that the X-ray photon flux (CCD counts) demonstrated an increase when the shock-front rotation angle was set at  $60^\circ$ . However, upon normalization with both the corresponding electron beam energy and electron beam charge, this effect was not evident. The experimental approach employed in this thesis to enhance betatron yield through shock-front rotation does indeed result in an increased betatron yield. Nevertheless, it is important to note that this increase is primarily attributed to the increase in electron beam charge rather than an increment in the amplitude of the transverse oscillation of the injected electron bunch.

### 5.2.1 2D PIC Simulation for Rotating Shock-front

To model the asymmetric injection of the electrons into the wakefield bubble and to characterise the synchrotron radiation emitted from the transverse oscillation of these relativistic electrons numerically, a 2D Particle-in-cell (2D PIC) simulations were carried out (Sec. 2.4). These simulations also allowed to verify the experimental findings for the betatron beam enhancement by creating an asymmetry in the electron injection process.

To evaluate the impact of asymmetric injection of the electrons by rotating the shockfront on the X-ray photon yield, this section will report the findings from the simulations. We will first model the gas density profile corresponding to the rotating shockfront as in the experiment (Fig:5.9), followed by the inspection of the tilt of the plasma "bubble". Thereafter, we will analyse the phase space properties of the injected

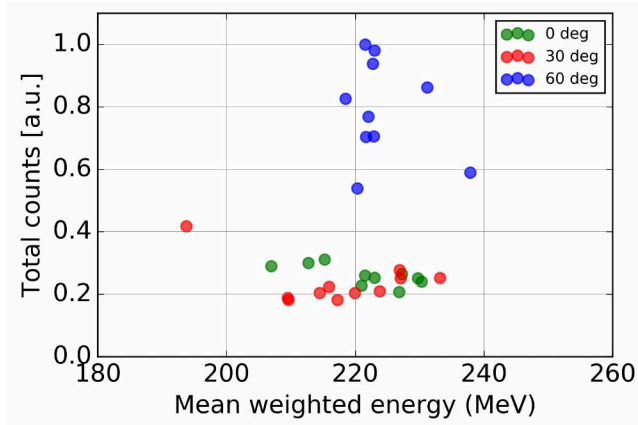


Figure 5.12: Figure showing the best electron data from each set of shock-front rotation. The dots represent a data from the specific rotation angle data-set. The total integrated count is plotted against the mean weighted energy of the electron beam obtained on the LANEX screen. The mean energy was calculated to be around 210 – 235 MeV. The plot indicates higher charge for 60° shock-front rotation angle which could be due to the formation of longer downramp length.

electrons and will compare the injected charge for different angles of shock-front rotation.

In the simulation conducted using the particle-in-cell (PIC) code SMILEI in a 2D geometry, a laser beam with a wavelength  $\lambda_0 = 800$  nm and a normalized amplitude  $a_0 = 3$  is focused on density profiles featuring both a straight and a rotated downramp, as depicted in Fig. 5.13. The overall plasma length considered was 4 mm, and the ramp profile exhibited a peak density twice that of the density in the acceleration section ( $8.5 \times 10^{17} \text{cm}^{-3}$ ). The rotation of the downramp resulted in breaking of axio-symmetric injection of the electrons as seen in figure 5.13 (a, b). This break in symmetric injection was expected to cause larger transverse oscillation of the injected electrons, hence enhancing the number of X-ray photons produced.

From the simulation, the phase space information of the injected electrons was extracted (Fig: 5.14). This information was crucial for understanding the transverse oscillations of the injected electrons, as it allowed for the measurement of their transverse momentum ( $P_y$ ) and transverse oscillation amplitude ( $Y$ ). Through analyzing this data, the first and second order moments ( mean and variance) of  $P_y$  and  $Y$  was calculated. Figure 5.14 is the phase space histogram of  $Y$ - $P_y$  values for the last time step of the simulation for straight and rotated downramp. This again shows a symmetric distribution of particles for straight edge (0°) when compared with the rotated edge (60°). The higher number of particles for (60°) could be due to a longer

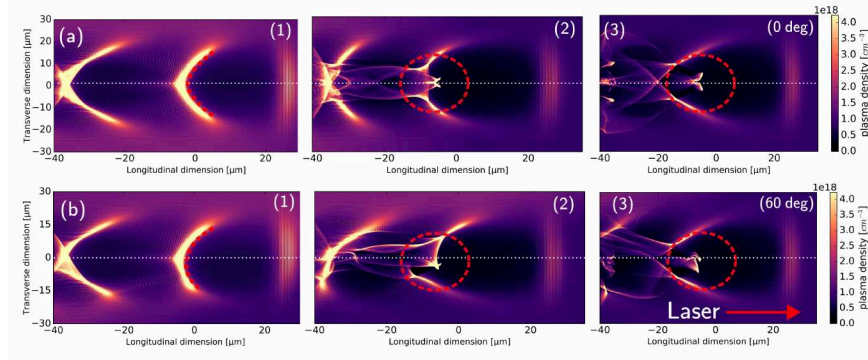


Figure 5.13: The snapshot of the wakefield process at the time-steps before, during and after the sharp density gradient (Fig:5.1) for two different angles of shockfront rotation (a)  $0^\circ$  and (b)  $60^\circ$  respectively . Compared to images in row (a) for straight edge, the axial symmetry of the injected electrons is broken for rotated downramp.

injection length created by rotated downramp.

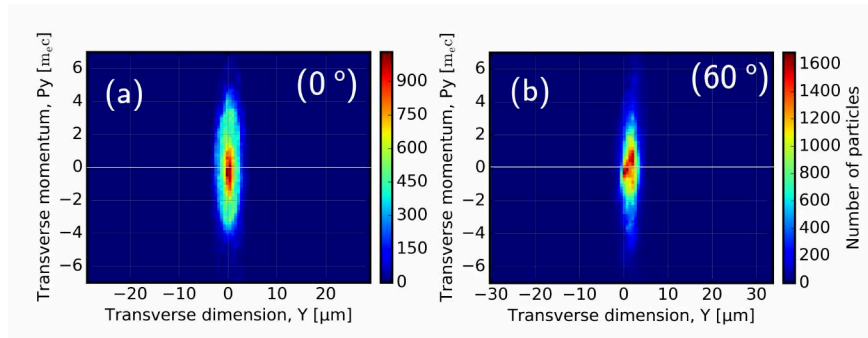


Figure 5.14: The histogram of the Y(transverse oscillation amplitude) -  $P_y$ (transverse momentum) phase space for  $0^\circ$  and  $60^\circ$  angle of shock-front rotation at identical simulation time-step, respectively. For  $60^\circ$ , a certain degree of asymmetry can be seen in the distribution of the particles when compared to the  $0^\circ$  case.

Moreover, the information about the weight, mean longitudinal momentum , mean transverse momentum, variance of the transverse momentum was calculated from the simulation data. The temporal evolution of these quantities were extracted from 2D PIC simulation for straight and rotating downramp. Figure 5.15 (a) and (b) shows the evolution of mean transverse momentum  $\langle P_y \rangle$  and its variance  $\langle \sigma^2 \rangle P_y$ . Although, the  $\langle P_y \rangle$  was relatively higher for the rotated shock-front case, the variance of the  $P_y$  was similar for both the cases. The variance measured shows any actual change in the transverse momentum of the trapped particles for the case of shockfront rotation. The increase in transverse amplitude and momentum by increasing the injection angle

of the electrons implies higher betatron oscillation amplitude which would in turn facilitate the betatron yield enhancement (Eqn: 2.41).

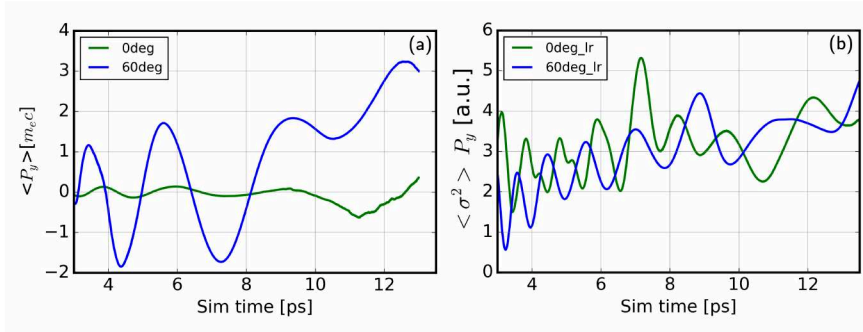


Figure 5.15: Temporal evolution of the electron transverse momentum (a) and its variance (b) for straight edge ( $0^\circ$ ) and rotated shockfront ( $60^\circ$ ). The mean transverse momentum,  $\langle P_y \rangle$ , was observed to be higher and its variance was found to be similar. The downramp length was  $300 \mu\text{m}$  with  $4.3 \text{ mm}$  acceleration length corresponding to  $13 \text{ ps}$  simulation time.

From figure 5.16 (a), we can see that the final energy of the injected electrons for both the case is  $\approx 190 \text{ MeV}$  (corresponding to the longitudinal momentum of  $380 [m_e c]$ ). This imply that the final energy of the injected electrons remains unaffected by the change in shock-front rotation angle. Figure 5.16 (b) points out that the number of particles injected for  $60^\circ$  angle of shockfront rotation is  $\approx 2.5\times$  higher than the case of straight edge. This is expected as by rotating the shockfront, there is a significant possibility of increasing the downramp length which then would assist in higher charge injection.

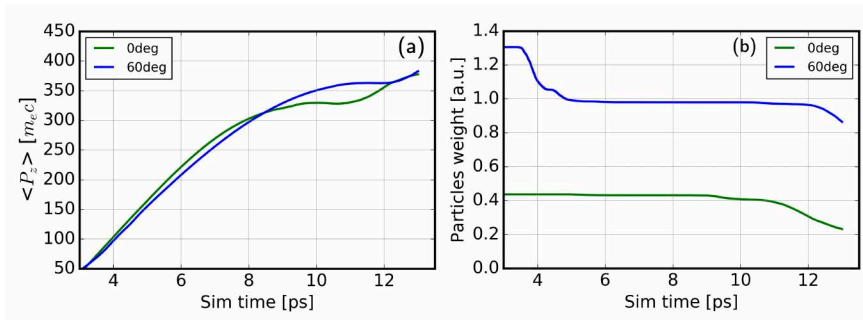


Figure 5.16: (a) The maximum longitudinal momentum for both the cases were fairly similar  $\approx 380 m_e c$  indicating no affect of rotation on the peak electron energy. (b) The final weight (charge) for the rotated case was  $\approx 2.5\times$  higher owing to longer downramp length due to shock-front rotation.

However, the simulation was done with the down-ramp length being kept as the floating parameter. The downramp length was chosen such that the simulation results

are in proximity with the experimental findings, in terms of injected charge and the final energy of the injected electron bunch. The increment in the transverse oscillation amplitude of the injected electron bunch and the increase in charge for the case of shockfront rotation points towards an increment in the betatron photon yield. However, the increase in the photon yield is majorly influenced by the increment in charge and not so significantly by the asymmetric injection of the electrons. Figure 5.17 compares the experimental and simulation data for the same.

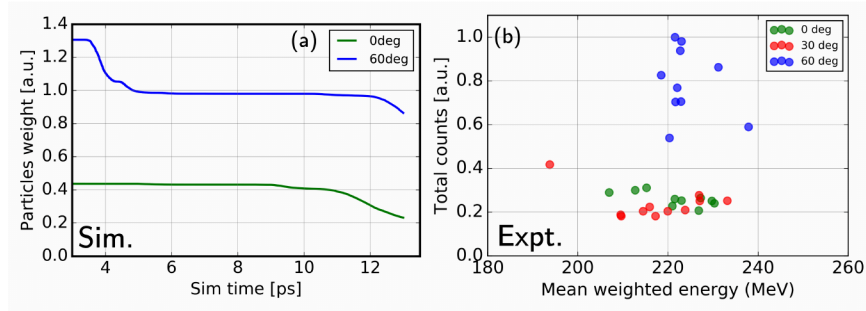


Figure 5.17: Total charge comparison for rotating shockfront, experimentally and by simulation. (a) The experimental data for the total injected charge in terms of CCD counts. It shows almost 3X increase in the total integrated counts (charge) for the case of  $60^\circ$  rotation angle when compared with the straight edge ( $0^\circ$ ). (b) The result from 2D-PIC simulation showing  $\approx 3\times$  increment in the charge for the rotated  $60^\circ$  case. The simulation data confirmed the increment in charge with the increase in the rotation angle.

In conclusion, It was observed that the electron beam measurements were highly sensitive to the change in laser beam parameters (chirp, pointing fluctuation) due to change in the plasma density and hence the refractive index for sharp density downramp. This lead to a high variance in the data obtained for this scheme. An increase in pointing fluctuation compared to the ionisation injection was expected as the laser gets refracted due to the sharp density gradient and injection of the electrons follow the directional change in the wake driving laser due to refraction. Even at lower plasma density  $2 \times 10^{18} \text{cm}^{-3}$ , the wiggler strength parameter ( $\mathcal{K}$ ) for shock-front injected electrons is higher than the dephasing electron beam from ionisation injection mechanism. This is due to the additional transverse momentum gained by the shock injected electrons from off-axis injection. This implies that the number of X-ray photons emitted/charge is higher for shock-front injection mechanism than ionisation injection for similar mean peak electron energies (Eqn:2.45).

Additionally, the change in transverse momentum of the injected electrons for rotated

shockfront was minimal compared to the change in the injected charge. The minimal change in the transverse momentum could be due to the ponderomotive scattered electrons coming back towards the laser axis at various angles resulting in a smaller net change in the transverse momentum amplitude. The increment in the injected charge with the increase in rotation angle is mainly due to the lengthening of the injection length while rotating the shockfront. The experimental and simulation results indicate the possibility of increasing the betatron yield by optimising the injection length and injection angle. For future purposes, a probe beam could be implemented to measure the change in the injection length with shockfront rotation experimentally.

Gas Jet Nozzle (mm)	Plasma Density [ $\times 10^{18}(\text{cm}^{-3})$ ]	$\langle E_{electron} \rangle$ (MeV)	$\langle Q \rangle$ (pC)	$\langle \text{Betatron energy} \rangle$ (nJ)	$\langle E_{crit} \rangle$ (keV)	$\mathcal{K}$ (x,y)
5	2	$\approx 220$	$34 \pm 17$	$\approx 24$	$\approx 10$	(14 , 9)

Table 5.1: Table summarising the electron and betatron beam properties measured from the shock-front injection scheme.

### 5.3 Summary

This chapter has reviewed results from shock assisted electron injection in laser plasma accelerator. By suppressing the self injection at lower plasma density and introducing the razor blade, a background free quasi-monoenergetic electron beam and the consequent betatron beam was measured (Tab: 5.1). The betatron beam produced had critical energy around 10 keV with  $10^6$  photons above 1 keV. Due to off-axis injection, the wiggler strength parameter ( $\mathcal{K}$ ) was higher compared to ionisation injection scheme implying higher X-ray photons emitted/charge for shock-front injection scheme for similar electron energies. Moreover, the rotating shockfront broke the axis-symmetry of the injected electrons and an increment in the X-ray photon yield was observed for higher degree of shockfront rotation. However, the increment in betatron yield was linear with the increment in charge due to increase in injection length for increasing angles of shock-front rotation. 2D PIC simulations based on experimental parameters agreed well with the qualitative observations of charge increment for the rotating shockfront case.

# 6 Discussions and Outlook

## 6.1 Discussion of Results

In this dissertation, the results from the two experiments are presented on electron acceleration and X-ray beam production using high intensity laser pulses.

	Ionisation injection	Shock-front Injection
<b>E-beam Parameters</b>		
$\langle E_{electron} \rangle$ (MeV)	$\approx 240$	$\approx 220$
$\langle Q \rangle$ (pC)	205	34
Divergence (x,y) ( $mrad^2$ )	$(7 \times 5)$	$(3 \times 3)$
Pointing ( $\Delta\theta_x, \Delta\theta_y$ ) ( $mrad^2$ )	$(0.65 \times 0.8)$	$(1.4 \times 2.1)$
Plasma Density ( $\times 10^{18} (cm^{-3})$ )	7.5	2
<b>Betatron beam parameters</b>		
Critical Energy ( $E_c$ ) (keV)	$\approx 30$	$\approx 10$
$\langle$ Integrated Betatron Energy $\rangle$ (nJ)	$\approx 470$	$\approx 24$
Divergence (x,y) ( $mrad^2$ )	$(25 \times 10)$	$(20 \times 6)$
Wiggler Parameter (x,y) ( $\mathcal{K}$ )	(10,4)	(14,9)
Source Size ( $\mu m$ )	$\approx 1.5$	$\approx 3$
Peak Brilliance ( $Photons/s/mm^2/mrad^2/0.1\%BW$ )	$10^{22}$	$10^{20}$

Table 6.1: Table comparing the electron beam and betatron beam parameters measured from ionisation injection and shock-front injection scheme.

The experiment presented in Chapter:4 produced relativistic electrons using ionization injection scheme. A gas cell with 10 mm gas cell length and  $H_2(95\%) + N_2(5\%)$  gas mixture was used to generate LWFA electrons. Due to small dephasing length (1.65 mm), the injected electrons caught upto the tail of the laser pulse and performed stronger oscillations under the effect of the laser's electric field. This increased the wiggler strength parameter ( $\mathcal{K}$ ) leading to an increment in critical energy and the photon flux of the betatron beam hence generated. A 25% increase in plasma density lead to 25% increment in  $\mathcal{K}$  which resulted in almost  $2\times$  increase in critical energy

and 25% increase in average photon flux/shot.

A higher  $\mathcal{K}$  along the laser polarisation direction resulted in higher angular distribution of the betatron beams along same direction, at higher plasma density. At higher plasma density, the electron pointing fluctuation was higher resulting in  $5\times$  increment in the pointing fluctuation of the generated betatron beams. The pointing fluctuation in the betatron beam was strongly correlated to the pointing fluctuations in the electron beam implying a strong pointing correlation between the electron beam and the resultant betatron beam. The source size was estimated to be around  $1\ \mu\text{m}$  giving the peak brilliance of the X-ray source as  $\approx 10^{22}$  photons/s/mm<sup>2</sup>/mrad<sup>2</sup>/0.1%BW.

In Chapter:5, the results were presented for the LWFA experiment using shockfront injection scheme. A 5 mm gas jet + razor blade assembly was used to create a sharp density downramp (shockfront) profile with Helium as the target gas. The self injection was suppressed at lower plasma density ( $\sim 2 \times 10^{18}\text{cm}^{-3}$ ) and by introducing the blade covering 30% of the gas jet nozzle, a quasi-monoenergetic beam was produced. The beam had  $< 10$  mrad divergence, 200-230 MeV peak energy with  $\frac{\Delta E}{E} < 10\%$  and  $34.8 \pm 17$  pC charge. The quasi-monoenergetic beams produced were quite sensitive to the experimental parameters leading to reproducibility at 40 – 50% (in general) and 70% in the best case scenario. The betatron beam generated from such quasi-monoenergetic electrons had critical energy around 10 keV, source size around  $3\ \mu\text{m}$ ,  $21 \times 6$  mrad<sup>2</sup> beam divergence resulting in the peak brilliance of  $\approx 10^{20}$  photons/s/mm<sup>2</sup>/mrad<sup>2</sup>/0.1%BW. To observe the effect of asymmetric injection on the X-ray photon yield, the shockfront was rotated and the electron and betatron beam diagnostics were analysed. The data-set lacked statistics due to unreliability of the electrons produced hence best single shot images were analysed for the rotated shockfront angles. The electron energy and charge showed increment with the increase in the rotation angle possibly due to the increase in acceleration length and injection length with rotating downramp. The X-ray flux also increased with increasing the shockfront rotation angle but it was mostly due to charge increment instead of the increment in the transverse oscillation amplitude of the injected electron bunch. A 2D PIC simulation done on smilei [77] using experimental parameters was in agreement with the increment of charge for the rotating shockfront case.

In conclusion, the brightest X-ray beams with greater shot-to- shot reproducibility was produced by using ionisation injection scheme. However, the number of X-ray photons/charge was higher for shockfront injection scheme.

## 6.2 Outlook

Betatron radiation presents a remarkable feature in the form of a high photon flux within an ultrashort femtosecond pulse, accompanied by a broad spectrum. This characteristic has been showcased in this work and by various other research groups previously [40, 83, 93]. In Figure 6.1, this high flux is vividly illustrated, showcasing the brilliant single-shot betatron beam imaging capability. In a demonstration of this, an IC was backlit by the betatron x-ray beam, and an x-ray camera recorded the transmitted x-rays.

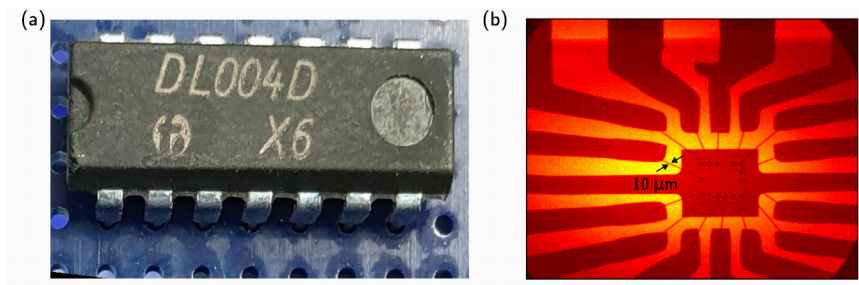


Figure 6.1: An IC imaged with an X-ray shadobox detector having  $49.5 \mu\text{m}$  pixel size. The IC (a) was backlit by the betatron X-ray beam and an X-ray camera recorded the image (b) with  $10\times$  magnification. One can see the  $10 \mu\text{m}$  connecting gold wires with a really high contrast clearly showing the single-shot imaging capability of the betatron source produced during the experiment.

As the betatron beam had high degree of stability 4.8, through meticulous optimization of object and detector positioning, a versatile setup can be devised for performing tomography, offering improved spatial resolution through phase-contrast imaging, as shown by the work of Wenz et al [115].

Betatron radiation's broadband and high photon flux characteristics make it exceptionally suitable for experiments demanding a uniform flux within an energy bandwidth of approximately 1 keV. This is particularly valuable in techniques like X-ray absorption spectroscopy (XAS) conducted near an absorption edge. XAS provides vital insights into an element's electronic and ionic structure.

In the vicinity of an absorption edge, X-ray absorption spectroscopy permits the determination of charge state and orbital occupancy, typically within about 50 eV from the absorption edge. Slightly offset at approximately 50 eV to 1000 eV, extended X-ray absorption fine structure analysis becomes feasible, offering valuable information regarding the type and number of lattice neighbors as well as bond distances.

Time-resolved spectroscopy of the absorption edge is a valuable tool commonly

employed in the investigation of Warm Dense Matter (WDM) within laboratory settings. WDM represents a unique state of matter characterized by densities near that of a solid and temperatures ranging from 0.1 eV to 100 eV (equivalent to  $10^3$  K to  $10^6$  K). The vast range of thermodynamic conditions poses a challenge for precise theoretical descriptions.

Research experiments focused on understanding the equation of state and transport properties of WDM provide crucial insights. These insights are not only relevant for fundamental physics but also have broader implications, such as enhancing our understanding of astrophysical phenomena. Comparing laboratory-based WDM studies with observations from telescopes and space probes enables a comprehensive investigation into the inner structure and evolutionary processes of giant gaseous planets.

Furthermore, this research approach has far-reaching applications. It aids in understanding ultra-fast laser processes, solid-liquid-plasma phase transitions, correlated electron systems, and the physics of high-pressure and shock environments.

Betatron radiation, employed as a source, offers a remarkable alternative for diving into new states of matter with exceptional temporal resolution. Utilizing femtosecond short x-ray probe pulses, we can access and explore non-equilibrium states. This capability opens up exciting possibilities for in-depth investigations into the properties of solid matter under extreme conditions of high temperature and pressure within the Warm Dense Matter (WDM) regime. The high precision and rapid time scales provided by betatron radiation enable a detailed and dynamic understanding of these non-equilibrium states, paving the way for groundbreaking advancements in material science and physics.



# Appendix

## Ionisation injection with He : N<sub>2</sub> (95 : 5)

The single shot electron beam spectrum along with its lineout for the gas cell length 10 mm having He : N<sub>2</sub> (95 : 5) as gas mix at plasma density  $5.1 \times 10^{18} [\text{cm}^{-3}]$ . The peak electron energy was consistently between 400-500 MeV with a mean charge of 17.8 pC.

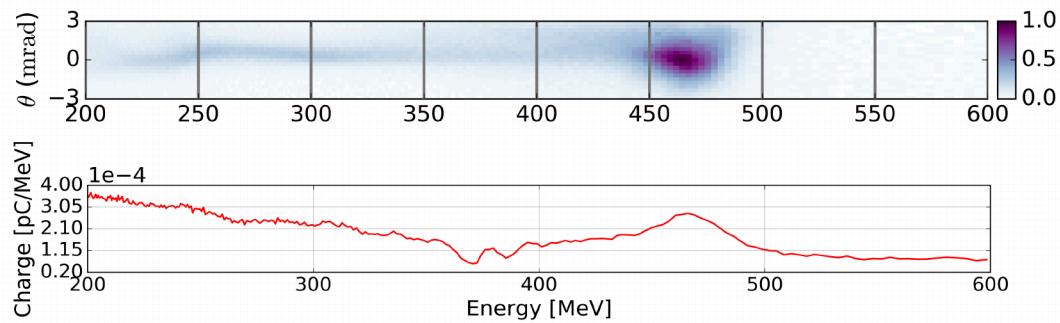


Figure 6.2: Single shot electron beam for gas mix He : N<sub>2</sub> (95 : 5). The total charge for this shot was 19 pC.

The X-ray beam profile for the same configuration shows the pointing fluctuation less than the single shot beam divergence for 45 consecutive shots.

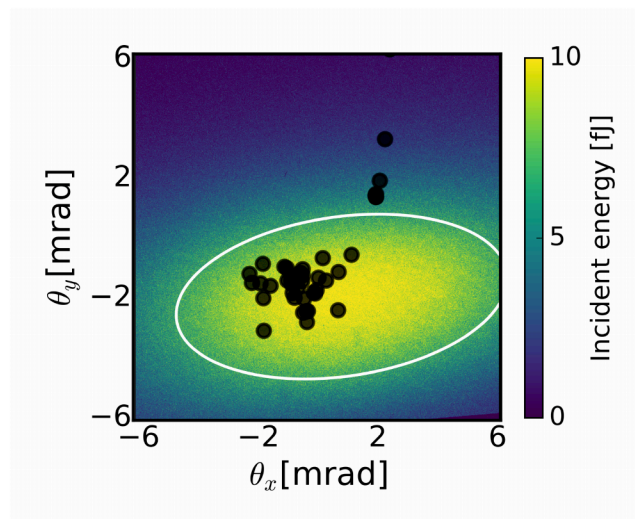


Figure 6.3: Single shot betatron beam profile for the above electron beam. The FWHM was 10 X 5 [mrad<sup>2</sup>]. The total integrated energy was 22 nJ.

## Electron beam oscillation in laser electric field

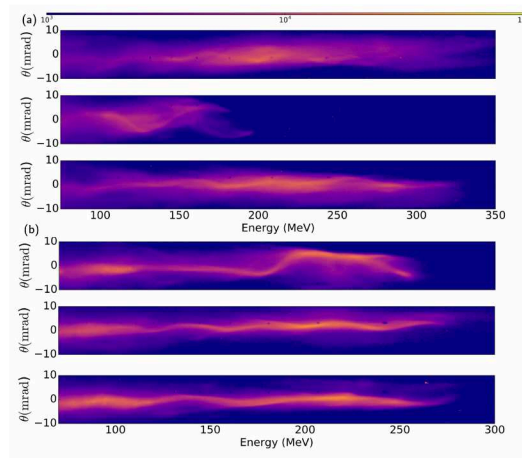


Figure 6.4: Consecutive electron beams showing dephasing of electrons for high plasma density (a) and low plasma density (b) for gas mix  $H_2 : N_2$  (95 : 5) in 10 mm gas cell.

## Betatron Imaging

An Iphone was placed in air just before the shadobox detector (in air) 10 cm away from the vacuum window. With no magnification, one can clearly see features  $< 1 \mu\text{m}$  being resolved with a high contrast in a single shot image.

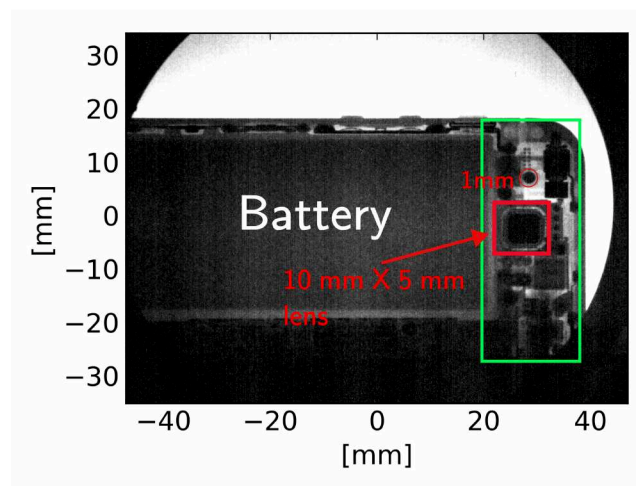


Figure 6.5: A single shot image of an Iphone 5s with magnification =1 with the betatron beam generated from 10mm gas cell length. The green rectangle shows a part of the motherboard where features smaller than 1 mm (red circle) could be easily resolved.

## Equations

<b>Laser and plasma parameters</b>	
Vector potential	$a_0 = 0.85\sqrt{I_0[10^{18}Wcm^{-2}]\lambda_L[\mu m]}$
Peak power	$P_0[TW] = 940(W_L[J]/t_{FWHM}[fs])$
Peak Intensity	$I_0[10^{18}W/cm^{-2}] = 1.37a_0^2/\lambda_L^2[\mu m]$
Plasma wavelength	$\lambda_p[\mu m] = 33.4/\sqrt{n_e[10^{18}cm^{-3}]}$

<b>LWFA parameters (Bubble regime)</b>	
Matched bubble radius	$R_b[\mu m] = 10 \times \sqrt{a_0/n_e[10^{18}cm^{-3}]}$
Dephasing length	$L_{deph}[\mu m] = 2/3 \times R_b[\mu m] \times \lambda_p^2[\mu m]/\lambda_0^2[\mu m]$
Pump depletion length	$L_{pd}[\mu m] = 0.3 \times \tau[fs] \times \lambda_p^2[\mu m]/\lambda_0^2[\mu m]$
Electron energy	$W_{el}[MeV] \approx 380 \frac{a_0}{n_e[10^{18}cm^{-3}]\lambda_L^2[\mu m]}$
Optimal charge	$Q_{opt}[pC] = 75\sqrt{a_0^2/n_e[10^{18}cm^{-3}]}$

<b>Betatron radiation</b>	
Betatron wavelength	$\lambda_\beta[\mu m] = 471 \times \sqrt{\gamma/n_e[10^{18}cm^{-3}]}$
Critical energy	$E_c[keV] = 5.24 \times 10^{-6} \times \gamma^2 \times n_e[10^{18}cm^{-3}] \times r_\beta[\mu m]$
Wiggler strength	$K = 0.133 \times \sqrt{\gamma \times n_e[10^{18}cm^{-3}]} \times r_\beta[\mu m]$

# Bibliography

- [1] A. Döpp, B. Mahieu, A. Lifschitz, C. Thaury, A. Doche, E. Guillaume, G. Grittani, O. Lundh, M. Hansson, J. Gautier, M. Kozlova, J. P. Goddet, P. Rousseau, A. Tafzi, V. Malka, A. Rousse, S. Corde, and K. Ta Phuoc, “Stable femtosecond x-rays with tunable polarization from a laser-driven accelerator,” *Light: Science & Applications*, vol. 6, pp. e17086–e17086, Nov 2017.
- [2] A. Döpp, L. Hehn, J. Götzfried, J. Wenz, M. Gilljohann, H. Ding, S. Schindler, F. Pfeiffer, and S. Karsch, “Quick x-ray microtomography using a laser-driven betatron source,” *Optica*, vol. 5, pp. 199–203, Feb 2018.
- [3] R. Rakowski, P. Zhang, K. Jensen, B. Kettle, T. Kawamoto, S. Banerjee, C. Fruhling, G. Golovin, D. Haden, M. S. Robinson, D. Umstadter, B. A. Shadwick, and M. Fuchs, “Transverse oscillating bubble enhanced laser-driven betatron x-ray radiation generation,” *Scientific Reports*, vol. 12, p. 10855, Jun 2022.
- [4] J. M. Cole, D. R. Symes, N. C. Lopes, J. C. Wood, K. Poder, S. Alatabi, S. W. Botchway, P. S. Foster, S. Gratton, S. Johnson, C. Kamperidis, O. Kononenko, M. De Lazzari, C. A. J. Palmer, D. Rusby, J. Sanderson, M. Sandholzer, G. Sarri, Z. Szoke-Kovacs, L. Teboul, J. M. Thompson, J. R. Warwick, H. Westerberg, M. A. Hill, D. P. Norris, S. P. D. Mangles, and Z. Najmudin, “High-resolution  $\mu\text{ct}$  of a mouse embryo using a compact laser-driven x-ray betatron source,” *Proceedings of the National Academy of Sciences*, vol. 115, pp. 6335–6340, Jun 2018.
- [5] A. Buck, J. Wenz, J. Xu, K. Khrennikov, K. Schmid, M. Heigoldt, J. M. Mikhailova, M. Geissler, B. Shen, F. Krausz, S. Karsch, and L. Veisz, “Shock-front injector for high-quality laser-plasma acceleration,” *Phys. Rev. Lett.*, vol. 110, p. 185006, May 2013.
- [6] H.-E. Tsai, K. K. Swanson, S. K. Barber, R. Lehe, H.-S. Mao, D. E. Mittelberger, S. Steinke, K. Nakamura, J. van Tilborg, C. Schroeder, E. Esarey, C. G. R. Geddes, and W. Leemans, “Control of quasi-monoenergetic electron beams from laser-plasma accelerators with adjustable shock density profile,” *Physics of Plasmas*, vol. 25, p. 043107, 04 2018.

- [7] M. Kozlova, I. Andriyash, J. Gautier, S. Sebban, S. Smartsev, N. Jourdain, U. Chaulagain, Y. Azamoum, A. Tafzi, J.-P. Goddet, K. Oubrierie, C. Thaury, A. Rousse, and K. Ta Phuoc, “Hard x rays from laser-wakefield accelerators in density tailored plasmas,” *Phys. Rev. X*, vol. 10, p. 011061, Mar 2020.
- [8] The CMS Collaboration, “Observation of a new boson at a mass of 125 gev with the cms experiment at the lhc,” *Physics Letters B*, vol. 716, no. 1, pp. 30–61, 2012.
- [9] ATLAS collaboration, “Evidence for the direct decay of the 125 gev higgs boson to fermions,” *Nature Physics*, vol. 10, pp. 557–560, Aug 2014.
- [10] M. Kado *et al.*, “Results with the full 2015 data sample from the atlas experiment,” 2015.
- [11] “Lightsources of the world.” <https://lightsources.org/lightsources-of-the-world>. Accessed: 2023-08-28.
- [12] “Cc by-sa 3.0,.” <https://commons.wikimedia.org/w/index.php?curid=537945>. Accessed: 2023-08-29.
- [13] M. Cornacchia, “The LCLS X-ray FEL at SLAC.” <https://www-ssrl.slac.stanford.edu/lcls/technotes/lcls-tn-99-6.pdf>, 1999. Accessed: 2023-08-29.
- [14] “The European XFEL.” <https://commons.wikimedia.org/w/index.php?curid=537945>. Accessed: 2023-08-29.
- [15] W. Röntgen, “Über eine neue Art von Strahlen: vorläufige Mitteilung.” [https://www.deutschestextarchiv.de/book/view/roentgen\\_strahlen\\_1896?p=10](https://www.deutschestextarchiv.de/book/view/roentgen_strahlen_1896?p=10). Accessed: 2023-08-31.
- [16] C. A. Taatjes, N. Hansen, J. A. Miller, T. A. Cool, J. Wang, P. R. Westmoreland, M. E. Law, T. Kasper, and K. Kohse-Höinghaus, “Combustion chemistry of enols: possible ethenol precursors in flames,” *The Journal of Physical Chemistry A*, vol. 110, pp. 3254–3260, Mar 2006.
- [17] T. Ohta, A. Bostwick, T. Seyller, K. Horn, and E. Rotenberg, “Controlling the electronic structure of bilayer graphene,” *Science*, vol. 313, pp. 951–954, Aug 2006.

- 
- [18] S.-B. Choe, Y. Acremann, A. Scholl, A. Bauer, A. Doran, J. Stöhr, and H. A. Padmore, “Vortex core-driven magnetization dynamics,” *Science*, vol. 304, pp. 420–422, Apr 2004.
- [19] H. Ohldag, T. Tyliczszak, R. Höhne, D. Spemann, P. Esquinazi, M. Ungureanu, and T. Butz, “ $\pi$ -electron ferromagnetism in metal-free carbon probed by soft x-ray dichroism,” *Phys. Rev. Lett.*, vol. 98, p. 187204, May 2007.
- [20] A. Wagner, R. Flaig, D. Zobel, B. Dittrich, P. Bombicz, M. Strümpel, P. Luger, T. Koritsanszky, and H.-G. Krane, “Structure and charge density of a c60-fullerene derivative based on a high resolution synchrotron diffraction experiment at 100 k,” *The Journal of Physical Chemistry A*, vol. 106, no. 28, pp. 6581–6590, 2002.
- [21] R. Fitzgerald, “Phase-sensitive x-ray imaging,” *Physics Today*, vol. 53, pp. 23–26, 07 2000.
- [22] V. Mocella, E. Brun, C. Ferrero, and D. Delattre, “Revealing letters in rolled herculaneum papyri by x-ray phase-contrast imaging,” *Nature Communications*, vol. 6, p. 5895, Jan 2015.
- [23] D. Strickland and G. Mourou, “Compression of amplified chirped optical pulses,” *Optics Communications*, vol. 55, no. 6, pp. 447–449, 1985.
- [24] C. N. Danson, C. Haefner, J. Bromage, T. Butcher, J.-C. F. Chanteloup, E. A. Chowdhury, A. Galvanauskas, L. A. Gizzi, J. Hein, D. I. Hillier, and et al., “Petawatt and exawatt class lasers worldwide,” *High Power Laser Science and Engineering*, vol. 7, p. e54, 2019.
- [25] G. Mourou, “Nobel lecture: Extreme light physics and application,” *Rev. Mod. Phys.*, vol. 91, p. 030501, Jul 2019.
- [26] K. J. Schafer, B. Yang, L. F. DiMauro, and K. C. Kulander, “Above threshold ionization beyond the high harmonic cutoff,” *Phys. Rev. Lett.*, vol. 70, pp. 1599–1602, Mar 1993.
- [27] P. B. Corkum, “Plasma perspective on strong field multiphoton ionization,” *Phys. Rev. Lett.*, vol. 71, pp. 1994–1997, Sep 1993.
- [28] F. Calegari, D. Ayuso, A. Trabattoni, L. Belshaw, S. D. Camillis, S. Anumula, F. Frassetto, L. Poletto, A. Palacios, P. Decleva, J. B. Greenwood, F. Martín, and

- M. Nisoli, “Ultrafast electron dynamics in phenylalanine initiated by attosecond pulses,” *Science*, vol. 346, no. 6207, pp. 336–339, 2014.
- [29] W. Mori, “The physics of the nonlinear optics of plasmas at relativistic intensities for short-pulse lasers,” *IEEE Journal of Quantum Electronics*, vol. 33, no. 11, pp. 1942–1953, 1997.
- [30] B. Albertazzi, A. Ciardi, M. Nakatsutsumi, T. Vinci, J. Béard, R. Bonito, J. Billette, M. Borghesi, Z. Burkley, S. Chen, T. Cowan, T. Herrmannsdörfer, D. Higginson, F. Kroll, S. Pikuz, K. Naughton, L. Romagnani, C. Riconda, G. Revet, and J. Fuchs, “Laboratory formation of a scaled protostellar jet by coaligned poloidal magnetic field,” *Science (New York, N.Y.)*, vol. 346, pp. 325–8, 10 2014.
- [31] S. P. D. Mangles, C. D. Murphy, Z. Najmudin, A. G. R. Thomas, J. L. Collier, A. E. Dangor, E. J. Divall, P. S. Foster, J. G. Gallacher, C. J. Hooker, D. A. Jaroszynski, A. J. Langley, W. B. Mori, P. A. Norreys, F. S. Tsung, R. Viskup, B. R. Walton, and K. Krushelnick, “Monoenergetic beams of relativistic electrons from intense laser–plasma interactions,” *Nature*, vol. 431, pp. 535–538, Sep 2004.
- [32] C. G. R. Geddes, C. Toth, J. van Tilborg, E. Esarey, C. B. Schroeder, D. Bruhwiler, C. Nieter, J. Cary, and W. P. Leemans, “High-quality electron beams from a laser wakefield accelerator using plasma-channel guiding,” *Nature*, vol. 431, pp. 538–541, Sep 2004.
- [33] J. Faure, Y. Glinec, A. Pukhov, S. Kiselev, S. Gordienko, E. Lefebvre, J.-P. Rousseau, F. Burgy, and V. Malka, “A laser–plasma accelerator producing monoenergetic electron beams,” *Nature*, vol. 431, pp. 541–544, Sep 2004.
- [34] P. Sprangle, E. Esarey, A. Ting, and G. Joyce, “Laser wakefield acceleration and relativistic optical guiding,” *Applied Physics Letters*, vol. 53, pp. 2146–2148, 11 1988.
- [35] E. Esarey, B. A. Shadwick, P. Catravas, and W. P. Leemans, “Synchrotron radiation from electron beams in plasma-focusing channels,” *Phys. Rev. E*, vol. 65, p. 056505, May 2002.
- [36] “Betatron etymology.” <https://physics.illinois.edu/people/history/betatron>. Accessed: 2023-10-12.

- 
- [37] S. Corde, K. Ta Phuoc, G. Lambert, R. Fitour, V. Malka, A. Rousse, A. Beck, and E. Lefebvre, “Femtosecond x rays from laser-plasma accelerators,” *Rev. Mod. Phys.*, vol. 85, pp. 1–48, Jan 2013.
- [38] S. Corde, C. Thaury, A. Lifschitz, G. Lambert, K. Ta Phuoc, X. Davoine, R. Lehe, D. Douillet, A. Rousse, and V. Malka, “Observation of longitudinal and transverse self-injections in laser-plasma accelerators,” *Nature Communications*, vol. 4, p. 1501, Feb 2013.
- [39] F. Albert, R. Shah, K. T. Phuoc, R. Fitour, F. Burgy, J.-P. Rousseau, A. Tafzi, D. Douillet, T. Lefrou, and A. Rousse, “Betatron oscillations of electrons accelerated in laser wakefields characterized by spectral x-ray analysis,” *Phys. Rev. E*, vol. 77, p. 056402, May 2008.
- [40] J. M. Cole, J. C. Wood, N. C. Lopes, K. Poder, R. L. Abel, S. Alatabi, J. S. J. Bryant, A. Jin, S. Kneip, K. Mecseki, D. R. Symes, S. P. D. Mangles, and Z. Najmudin, “Laser-wakefield accelerators as hard x-ray sources for 3d medical imaging of human bone,” *Scientific Reports*, vol. 5, p. 13244, Aug 2015.
- [41] M. Schnell, A. Sävert, B. Landgraf, M. Reuter, M. Nicolai, O. Jäckel, C. Peth, T. Thiele, O. Jansen, A. Pukhov, O. Willi, M. C. Kaluza, and C. Spielmann, “Deducing the electron-beam diameter in a laser-plasma accelerator using x-ray betatron radiation,” *Phys. Rev. Lett.*, vol. 108, p. 075001, Feb 2012.
- [42] T. Tajima and J. M. Dawson, “Laser electron accelerator,” *Phys. Rev. Lett.*, vol. 43, pp. 267–270, Jul 1979.
- [43] G. Mourou, “Nobel lecture: Extreme light physics and application,” *Reviews of Modern Physics*, vol. 91, 07 2019.
- [44] F. F. Chen, *Introduction to Plasma Physics and Controlled Fusion*. Springer New York, NY, 2013.
- [45] W. L. Kruer, “Laser plasma interactions with intensities,” *Physics of Plasmas*, vol. 10, pp. 2087–2092, 04 2003.
- [46] M. Schnell, *Betatron radiation from a laser plasma accelerator*. PhD dissertation, Friedrich-Schiller-Universität Jena, 2014.
- [47] E. Esarey, C. B. Schroeder, and W. P. Leemans, “Physics of laser-driven plasma-based electron accelerators,” *Rev. Mod. Phys.*, vol. 81, pp. 1229–1285, Aug 2009.

- [48] D. Umstadter, “Relativistic laser–plasma interactions,” *Journal of Physics D: Applied Physics*, vol. 36, p. 8, 2003.
- [49] E. Esarey, P. Sprangle, J. Krall, and A. Ting, “Self-focusing and guiding of short laser pulses in ionizing gases and plasmas,” *IEEE Journal of Quantum Electronics*, vol. 33, no. 11, pp. 1879–1914, 1997.
- [50] N. Kant, S. Saralch, and H. Singh, “Ponderomotive self-focusing of a short laser pulse under a plasma density ramp,” *Nukleonika*, vol. 56, no. 2, pp. 149–153, 2011.
- [51] E. S. Sarachik and G. T. Schappert, “Classical theory of the scattering of intense laser radiation by free electrons,” *Phys. Rev. D*, vol. 1, pp. 2738–2753, May 1970.
- [52] J. D. Lawson, “Lasers and accelerators,” *IEEE Transactions on Nuclear Science*, vol. 26, no. 3, pp. 4217–4219, 1979.
- [53] P. Woodward, “The theoretical precision with which an arbitrary radiation-pattern may be obtained from a source of finite size,” *Journal of the Institution of Electrical Engineers - Part I: General*, vol. 95, pp. 405–405(0), September 1948.
- [54] D. Bauer, P. Mulser, and W. H. Steeb, “Relativistic ponderomotive force, uphill acceleration, and transition to chaos,” *Phys. Rev. Lett.*, vol. 75, pp. 4622–4625, Dec 1995.
- [55] B. Quesnel and P. Mora, “Theory and simulation of the interaction of ultraintense laser pulses with electrons in vacuum,” *Phys. Rev. E*, vol. 58, pp. 3719–3732, Sep 1998.
- [56] K. Nakajima, D. Fisher, T. Kawakubo, H. Nakanishi, A. Ogata, Y. Kato, Y. Kitagawa, R. Kodama, K. Mima, H. Shiraga, K. Suzuki, K. Yamakawa, T. Zhang, Y. Sakawa, T. Shoji, Y. Nishida, N. Yugami, M. Downer, and T. Tajima, “Observation of ultrahigh gradient electron acceleration by a self-modulated intense short laser pulse,” *Phys. Rev. Lett.*, vol. 74, pp. 4428–4431, May 1995.
- [57] A. Modena, Z. Najmudin, A. E. Dangor, C. E. Clayton, K. A. Marsh, C. Joshi, V. Malka, C. B. Darrow, C. Danson, D. Neely, and F. N. Walsh, “Electron acceleration from the breaking of relativistic plasma waves,” *Nature*, vol. 377, pp. 606–608, Oct 1995.

- 
- [58] W. P. Leemans, B. Nagler, A. J. Gonsalves, C. Tóth, K. Nakamura, C. G. R. Geddes, E. Esarey, C. B. Schroeder, and S. M. Hooker, “Gev electron beams from a centimetre-scale accelerator,” *Nature Physics*, vol. 2, pp. 696–699, Oct 2006.
- [59] C. E. Clayton, K. A. Marsh, A. Dyson, M. Everett, A. Lal, W. P. Leemans, R. Williams, and C. Joshi, “Ultrahigh-gradient acceleration of injected electrons by laser-excited relativistic electron plasma waves,” *Phys. Rev. Lett.*, vol. 70, pp. 37–40, Jan 1993.
- [60] J. Faure, C. Rechatin, A. Norlin, A. Lifschitz, Y. Glinec, and V. Malka, “Controlled injection and acceleration of electrons in plasma wakefields by colliding laser pulses,” *Nature*, vol. 444, pp. 737–739, Dec 2006.
- [61] J. Faure, C. Rechatin, A. Norlin, F. Burgy, A. Tafzi, J.-P. Rousseau, and V. Malka, “Controlled electron injection in a laser-plasma accelerator,” *Plasma Physics and Controlled Fusion*, vol. 49, p. B395, nov 2007.
- [62] S. Kalmykov, S. A. Yi, V. Khudik, and G. Shvets, “Electron self-injection and trapping into an evolving plasma bubble,” *Phys. Rev. Lett.*, vol. 103, p. 135004, Sep 2009.
- [63] V. Maxim, B. D. Nikolai, and P. K. Vladimir, *Tunnel Ionization Of Complex Atoms And Atomic Ions In Electromagnetic Field*, vol. 0664. SPIE, October 1986.
- [64] A. Pak, K. A. Marsh, S. F. Martins, W. Lu, W. B. Mori, and C. Joshi, “Injection and trapping of tunnel-ionized electrons into laser-produced wakes,” *Phys. Rev. Lett.*, vol. 104, p. 025003, Jan 2010.
- [65] H. Suk, N. Barov, J. B. Rosenzweig, and E. Esarey, “Plasma electron trapping and acceleration in a plasma wake field using a density transition,” *Phys. Rev. Lett.*, vol. 86, pp. 1011–1014, Feb 2001.
- [66] A. Brantov, T. Esirkepov, M. Kando, H. Kotaki, V. Bychenkov, and S. Bulanov, “Controlled electron injection into the wake wave using plasma density inhomogeneity,” *Physics of Plasmas*, vol. 15, pp. 073111–073111, 07 2008.
- [67] K. Schmid, A. Buck, C. M. S. Sears, J. M. Mikhailova, R. Tautz, D. Herrmann, M. Geissler, F. Krausz, and L. Veisz, “Density-transition based electron injector

- for laser driven wakefield accelerators,” *Phys. Rev. ST Accel. Beams*, vol. 13, p. 091301, Sep 2010.
- [68] M. Burza, A. Gonoskov, K. Svensson, F. Wojda, A. Persson, M. Hansson, G. Genoud, M. Marklund, C.-G. Wahlström, and O. Lundh, “Laser wakefield acceleration using wire produced double density ramps,” *Phys. Rev. ST Accel. Beams*, vol. 16, p. 011301, Jan 2013.
- [69] P. Brijesh, C. Thaury, K. T. Phuoc, S. Corde, G. Lambert, V. Malka, S. P. D. Mangles, M. Bloom, and S. Kneip, “Tuning the electron energy by controlling the density perturbation position in laser plasma accelerators,” *Physics of Plasmas*, vol. 19, p. 063104, 06 2012.
- [70] A. Pukhov and J. Meyer-ter Vehn, “Laser wake field acceleration: the highly non-linear broken-wave regime,” *Applied Physics B*, vol. 74, pp. 355–361, Apr 2002.
- [71] W. Lu, C. Huang, M. Zhou, W. B. Mori, and T. Katsouleas, “Nonlinear theory for relativistic plasma wakefields in the blowout regime,” *Phys. Rev. Lett.*, vol. 96, p. 165002, Apr 2006.
- [72] I. Kostyukov, A. Pukhov, and S. Kiselev, “Phenomenological theory of laser-plasma interaction in “bubble” regime,” *Physics of Plasmas*, vol. 11, 10 2004.
- [73] S. Gordienko and A. Pukhov, “Scalings for ultrarelativistic laser plasmas and quasimonoenergetic electrons,” *Physics of Plasmas*, vol. 12, p. 043109, 04 2005.
- [74] T. Katsouleas, “Physical mechanisms in the plasma wake-field accelerator,” *Phys. Rev. A*, vol. 33, pp. 2056–2064, Mar 1986.
- [75] W. Rittershofer, C. B. Schroeder, E. Esarey, F. J. Grüner, and W. P. Leemans, “Tapered plasma channels to phase-lock accelerating and focusing forces in laser-plasma accelerators,” *Physics of Plasmas*, vol. 17, p. 063104, 06 2010.
- [76] J. Wenz and S. Karsch, “Physics of laser-wakefield accelerators (lwfa),” 2020.
- [77] J. Derouillat, A. Beck, F. Pérez, T. Vinci, M. Chieramello, A. Grassi, M. Flé, G. Bouchard, I. Plotnikov, N. Aunai, J. Dargent, C. Riconda, and M. Grech, “Smilei : A collaborative, open-source, multi-purpose particle-in-cell code for plasma simulation,” *Computer Physics Communications*, vol. 222, pp. 351–373, 2018.

- 
- [78] R. A. Fonseca, S. F. Martins, L. O. Silva, J. W. Tonge, F. S. Tsung, and W. B. Mori, “One-to-one direct modeling of experiments and astrophysical scenarios: pushing the envelope on kinetic plasma simulations,” *Plasma Physics and Controlled Fusion*, vol. 50, p. 124034, nov 2008.
- [79] F. Quere, C. Thaury, H. George, J. Geindre, E. Lefebvre, G. Bonnaud, P. Monot, and P. Martin, “High-order harmonic generation using plasma mirrors,” *Plasma Physics and Controlled Fusion*, vol. 50, 12 2008.
- [80] S. Kuschel, *Generation of dense electron bunches by laser plasma accelerators for QED experiments in high fields*. PhD dissertation, Friedrich-Schiller-Universität Jena, 2018.
- [81] A. Buck, *Advanced characterization and control of laser wakefield acceleration*. PhD dissertation, Ludwig-Maximilians-Universität München, 2011.
- [82] A. Buck, M. Nicolai, K. Schmid, C. M. S. Sears, A. Sävert, J. M. Mikhailova, F. Krausz, M. C. Kaluza, and L. Veisz, “Real-time observation of laser-driven electron acceleration,” *Nature Physics*, vol. 7, pp. 543–548, Jul 2011.
- [83] S. Kneip, C. McGuffey, J. L. Martins, S. F. Martins, C. Bellei, V. Chvykov, F. Dollar, R. Fonseca, C. Huntington, G. Kalintchenko, A. Maksimchuk, S. P. D. Mangles, T. Matsuoka, S. R. Nagel, C. A. J. Palmer, J. Schreiber, K. T. Phuoc, A. G. R. Thomas, V. Yanovsky, L. O. Silva, K. Krushelnick, and Z. Najmudin, “Bright spatially coherent synchrotron x-rays from a table-top source,” *Nature Physics*, vol. 6, pp. 980–983, Dec 2010.
- [84] J. Jackson, *Classical electrodynamics*. Wiley 2021-05-13, Hoboken, 2021.
- [85] F. R. Elder, A. M. Gurewitsch, R. V. Langmuir, and H. C. Pollock, “Radiation from electrons in a synchrotron,” *Phys. Rev.*, vol. 71, pp. 829–830, Jun 1947.
- [86] M. Z. Mo, Z. Chen, S. Fourmaux, A. Saraf, K. Otani, J. C. Kieffer, Y. Y. Tsui, A. Ng, and R. Fedosejevs, “Laser wakefield generated X-ray probe for femtosecond time-resolved measurements of ionization states of warm dense aluminum,” *Review of Scientific Instruments*, vol. 84, p. 123106, 12 2013.
- [87] J. C. Wood, D. J. Chapman, K. Poder, N. C. Lopes, M. E. Rutherford, T. G. White, F. Albert, K. T. Behm, N. Booth, J. S. J. Bryant, P. S. Foster, S. Glenzer, E. Hill, K. Krushelnick, Z. Najmudin, B. B. Pollock, S. Rose, W. Schumaker,

- R. H. H. Scott, M. Sherlock, A. G. R. Thomas, Z. Zhao, D. E. Eakins, and S. P. D. Mangles, “Ultrafast imaging of laser driven shock waves using betatron x-rays from a laser wakefield accelerator,” *Scientific Reports*, vol. 8, p. 11010, Jul 2018.
- [88] S. Fourmaux, S. Corde, K. T. Phuoc, P. Lassonde, G. Lebrun, S. Payeur, F. Martin, S. Sebban, V. Malka, A. Rousse, and J. C. Kieffer, “Single shot phase contrast imaging using laser-produced betatron x-ray beams,” *Opt. Lett.*, vol. 36, pp. 2426–2428, Jul 2011.
- [89] T. Brabec and F. Krausz, “Intense few-cycle laser fields: Frontiers of nonlinear optics,” *Rev. Mod. Phys.*, vol. 72, pp. 545–591, Apr 2000.
- [90] B. Dromey, M. Zepf, A. Gopal, K. Lancaster, M. S. Wei, K. Krushelnick, M. Tatarakis, N. Vakakis, S. Moustazis, R. Kodama, M. Tampo, C. Stoeckl, R. Clarke, H. Habara, D. Neely, S. Karsch, and P. Norreys, “High harmonic generation in the relativistic limit,” *Nature Physics*, vol. 2, pp. 456–459, Jul 2006.
- [91] T. Z. Esirkepov, S. V. Bulanov, M. Kando, A. S. Pirozhkov, and A. G. Zhidkov, “Boosted high-harmonics pulse from a double-sided relativistic mirror,” *Phys. Rev. Lett.*, vol. 103, p. 025002, Jul 2009.
- [92] A. Rousse, P. Audebert, J. P. Geindre, F. Fallières, J. C. Gauthier, A. Mysyrowicz, G. Grillon, and A. Antonetti, “Efficient  $k\alpha$  x-ray source from femtosecond laser-produced plasmas,” *Phys. Rev. E*, vol. 50, pp. 2200–2207, Sep 1994.
- [93] H.-P. Schlenvoigt, K. Haupt, A. Debus, F. Budde, O. Jäckel, S. Pfotenhauer, H. Schwoerer, E. Rohwer, J. G. Gallacher, E. Brunetti, R. P. Shanks, S. M. Wiggins, and D. A. Jaroszynski, “A compact synchrotron radiation source driven by a laser-plasma wakefield accelerator,” *Nature Physics*, vol. 4, pp. 130–133, Feb 2008.
- [94] M. Fuchs, R. Weingartner, A. Popp, Z. Major, S. Becker, J. Osterhoff, I. Cortrie, B. Zeitler, R. Hörlein, G. D. Tsakiris, U. Schramm, T. P. Rowlands-Rees, S. M. Hooker, D. Habs, F. Krausz, S. Karsch, and F. Grüner, “Laser-driven soft-x-ray undulator source,” *Nature Physics*, vol. 5, pp. 826–829, Nov 2009.
- [95] K. Ta Phuoc, S. Corde, C. Thaury, V. Malka, A. Tafzi, J. P. Goddet, R. C. Shah,

- 
- S. Sebban, and A. Rousse, “All-optical Compton gamma-ray source,” *Nature Photonics*, vol. 6, pp. 308–311, May 2012.
- [96] H. Schwöerer, B. Liesfeld, H.-P. Schlenvoigt, K.-U. Amthor, and R. Sauerbrey, “Thomson-backscattered x rays from laser-accelerated electrons,” *Phys. Rev. Lett.*, vol. 96, p. 014802, Jan 2006.
- [97] A. Rousse, K. T. Phuoc, R. Shah, A. Pukhov, E. Lefebvre, V. Malka, S. Kiselev, F. Burgy, J.-P. Rousseau, D. Umstadter, and D. Hulin, “Production of a keV x-ray beam from synchrotron radiation in relativistic laser-plasma interaction,” *Phys. Rev. Lett.*, vol. 93, p. 135005, Sep 2004.
- [98] K. T. Phuoc, F. Burgy, J.-P. Rousseau, V. Malka, A. Rousse, R. Shah, D. Umstadter, A. Pukhov, and S. Kiselev, “Laser based synchrotron radiation,” *Physics of Plasmas*, vol. 12, p. 023101, 01 2005.
- [99] M. Schnell, A. Sävert, B. Landgraf, M. Reuter, M. Nicolai, O. Jäckel, C. Peth, T. Thiele, O. Jansen, A. Pukhov, O. Willi, M. C. Kaluza, and C. Spielmann, “Deducing the electron-beam diameter in a laser-plasma accelerator using x-ray betatron radiation,” *Phys. Rev. Lett.*, vol. 108, p. 075001, Feb 2012.
- [100] S. Kiselev, A. Pukhov, and I. Kostyukov, “X-ray generation in strongly nonlinear plasma waves,” *Phys. Rev. Lett.*, vol. 93, p. 135004, Sep 2004.
- [101] S. P. D. Mangles, G. Genoud, M. S. Bloom, M. Burza, Z. Najmudin, A. Persson, K. Svensson, A. G. R. Thomas, and C.-G. Wahlström, “Self-injection threshold in self-guided laser wakefield accelerators,” *Phys. Rev. ST Accel. Beams*, vol. 15, p. 011302, Jan 2012.
- [102] S. Semushin and V. Malka, “High density gas jet nozzle design for laser target production,” *Review of Scientific Instruments*, vol. 72, pp. 2961–2965, 07 2001.
- [103] J. Osterhoff, A. Popp, Z. Major, B. Marx, T. P. Rowlands-Rees, M. Fuchs, M. Geissler, R. Hörlein, B. Hidding, S. Becker, E. A. Peralta, U. Schramm, F. Grüner, D. Habs, F. Krausz, S. M. Hooker, and S. Karsch, “Generation of stable, low-divergence electron beams by laser-wakefield acceleration in a steady-state-flow gas cell,” *Phys. Rev. Lett.*, vol. 101, p. 085002, Aug 2008.
- [104] C. E. Clayton, J. E. Ralph, F. Albert, R. A. Fonseca, S. H. Glenzer, C. Joshi, W. Lu, K. A. Marsh, S. F. Martins, W. B. Mori, A. Pak, F. S. Tsung, B. B.

- Pollock, J. S. Ross, L. O. Silva, and D. H. Froula, “Self-guided laser wakefield acceleration beyond 1 gev using ionization-induced injection,” *Phys. Rev. Lett.*, vol. 105, p. 105003, Sep 2010.
- [105] T. Kurz, J. P. Couperus, J. M. Krämer, H. Ding, S. Kuschel, A. Köhler, O. Zarini, D. Hollatz, D. Schinkel, R. D’Arcy, J.-P. Schwinkendorf, J. Osterhoff, A. Irman, U. Schramm, and S. Karsch, “Calibration and cross-laboratory implementation of scintillating screens for electron bunch charge determination,” *Review of Scientific Instruments*, vol. 89, p. 093303, 09 2018.
- [106] S. Cipiccia, M. R. Islam, B. Ersfeld, R. P. Shanks, E. Brunetti, G. Vieux, X. Yang, R. C. Issac, S. M. Wiggins, G. H. Welsh, M.-P. Anania, D. Maneuski, R. Montgomery, G. Smith, M. Hoek, D. J. Hamilton, N. R. C. Lemos, D. Symes, P. P. Rajeev, V. O. Shea, J. M. Dias, and D. A. Jaroszynski, “Gamma-rays from harmonically resonant betatron oscillations in a plasma wake,” *Nature Physics*, vol. 7, pp. 867–871, Nov 2011.
- [107] “Photon cross section data for silicon.” <https://physics.nist.gov/PhysRefData/Xcom/html/xcom1.html>. Accessed: 2023-09-07.
- [108] ANDOR, “High Energy Detection Solutions Beyond The Visible. Product brochure.” [https://andor.oxinst.com/assets/uploads/Andor\\_High\\_Energy\\_Detection\\_Brochure.pdf](https://andor.oxinst.com/assets/uploads/Andor_High_Energy_Detection_Brochure.pdf). Accessed: 2023-09-12.
- [109] ANDOR, “ANDOR direct detection imaging.” <https://andor.oxinst.com/assets/uploads/products/andor/documents/andor-ikon-1-and-m-so-specifications.pdf>. Accessed: 2023-09-12.
- [110] TELEDYNE, “Shad-o-Box HS Product Family Datasheet.” [https://www.teledyneicm.com/wp-content/uploads/2016/05/ShadoBoxHS\\_datasheet.pdf](https://www.teledyneicm.com/wp-content/uploads/2016/05/ShadoBoxHS_datasheet.pdf). Accessed: 2023-09-12.
- [111] S. Kneip, “Laser plasma accelerator and wiggler.” <https://spiral.imperial.ac.uk/handle/10044/1/5671>. Accessed: 2023-08-12.
- [112] A. Schöps, P. Vagin, and M. Tischer, “Properties of the insertion devices for PETRA III and its extension,” *AIP Conference Proceedings*, vol. 1741, p. 020019, 07 2016.

- [113] C. G. Schroer, H.-C. Wille, O. H. Seeck, K. Bagschik, H. Schulte-Schrepping, M. Tischer, H. Graafsma, W. Laasch, K. Baev, S. Klumpp, R. Bartolini, H. Reichert, W. Leemans, and E. Weckert, “The synchrotron radiation source petra iii and its future ultra-low-emittance upgrade petra iv,” *The European Physical Journal Plus*, vol. 137, p. 1312, Dec 2022.
- [114] A. Doherty, S. Fourmaux, A. Astolfo, R. Ziesche, J. Wood, O. Finlay, W. Stolp, D. Batey, I. Manke, F. Légaré, M. Boone, D. Symes, Z. Najmudin, M. Endrizzi, A. Olivo, and S. Cipiccia, “Femtosecond multimodal imaging with a laser-driven x-ray source,” *Communications Physics*, vol. 6, p. 288, Oct 2023.
- [115] J. Wenz, S. Schleede, K. Khrennikov, M. Bech, P. Thibault, M. Heigoldt, F. Pfeiffer, and S. Karsch, “Quantitative x-ray phase-contrast microtomography from a compact laser-driven betatron source,” *Nature Communications*, vol. 6, p. 7568, Jul 2015.



# List of Publications

## Unpublished

1. **H. Harsh**, D. Ullman, F. C. Salgado, D. Seipt, A. Sävert, M. Zepf “Bright and stable X-rays from Laser Wakefield Accelerator Using Ionization Injection Scheme” *in preparation*
2. **H. Harsh**, F. C. Salgado, D. Ullman, A. Sävert, D. Seipt, M. Zepf “Betatron beam measurement from quasi-monoenergetic electron beam generated using shockfront injection scheme” *in preparation*
3. **H. Harsh**, I. Uschmann, M. Zepf “Calibration of the Shd-o-box detector” *in preparation*

## Published

1. F. C. Salgado, N. Cavanagh, M. Tamburini, D. W. Storey, R. Beyer, P. H. Bucksbaum, Z. Chen, A. Di Piazza, E. Gerstmayr, **Harsh**, E. Isele, A. R. Jungmans, C. H. Keitel, S. Kuschel, C. F. Nielsen, D. A. Reis, C. Roedel, G. Sarri, A. Seidel, C. Schneider, U. I. Uggerhøj, J. Wulff, V. Yakimenko, C. Zepf, S. Meuren, and M. Zepf, “Single particle detection system for strong-field QED experiments,” *New J. Phys.*, vol. 24, no. 1, p. 015002, 2022.
2. B. Kettle, D. Hollatz, E. Gerstmayr, G. M. Samarin, A. Alejo, S. Astbury, C. Baird, S. Bohlen, M. Campbell, C. Colgan, D. Dannheim, C. Gregory, **H. Harsh**, P. Hatfield, J. Hinojosa, Y. Katzir, J. Morton, C. D. Murphy, A. Nurnberg, J. Osterhoff, G. Pérez-Callejo, K. Pöoder, P. P. Rajeev, C. Roedel, F. Roeder, F. C. Salgado, G. Sarri, A. Seidel, S. Spannagel, C. Spindloe, S. Steinke, M. J. V. Streeter, A. G. R. Thomas, C. Underwood, R. Watt, M. Zepf, S. J. Rose, and S. P. D. Mangles, “A laser–plasma platform for photon–photon physics: the two photon Breit–Wheeler process,” *New J. Phys.*, vol. 23, no. 11, p. 115006, 2021.
3. H. Abramowicz, U. Acosta, M. Altarelli, R. Aßmann, Z. Bai, T. Behnke, Y. Benhammou, T. Blackburn, S. Boogert, O. Borysov, M. Borysova, R. Brinkmann, M. Bruschi, F. Burkart, K. Büßer, N. Cavanagh, O. Davidi, W. Decking, U. Dosselli, N. Elkina, A. Fedotov, M. Firlej, T. Fiutowski, K. Fleck, M. Gostkin, C.

- Grojean, J. Hallford, **H. Harsh**, A. Hartin, B. Heinemann, T. Heinzl, L. Helary, S. Huang, X. Huang, M. Idzik, A. Ilderton, R. Jacobs, B. Kämpfer, B. King, H. Lahno, A. Levanon, A. Levy, I. Levy, J. List, W. Lohmann, T. Ma, A. J. Macleod, V. Malka, F. Meloni, A. Mironov, M. Morandin, J. Moron, E. Negodin, G. Perez, I. Pomerantz, R. Pöschl, R. Prasad, F. Quéré, A. Ringwald, C. Rödel, S. Rykovanov, F. Salgado, A. Santra, G. Sarri, A. Sävert, A. Sbrizzi, S. Schmitt, U. Schramm, S. Schuwalow, D. Seipt, L. Shaimerdenova, M. Shchedrolosiev, M. Skakunov, Y. Soreq, M. Streeter, K. Swientek, N. T. Hod, S. Tang, T. Teter, D. Thoden, A. I. Titov, O. Tolbanov, G. Torgrimsson, A. Tyazhev, M. Wing, M. Zanetti, A. Zarubin, K. Zeil, M. Zepf, and A. Zhemchukov, “Conceptual design report for the LUXE experiment,” *Eur. Phys. J. Spec. Top.*, vol. 230, no. 11, pp. 2445–2560, 2021.
4. H. Abramowicz, M. Altarelli, R. Aßmann, T. Behnke, Y. Benhammou, O. Borysov, M. Borysova, R. Brinkmann, F. Burkart, K. Büßer, O. Davidi, W. Decking, N. Elkina, **H. Harsh**, A. Hartin, I. Hartl, B. Heinemann, T. Heinzl, N. TalHod, M. Hoffmann, A. Ilderton, B. King, A. Levy, J. List, A. R. Maier, E. Negodin, G. Perez, I. Pomerantz, A. Ringwald, C. Rödel, M. Saimpert, F. Salgado, G. Sarri, I. Savoray, T. Teter, M. Wing, and M. Zepf, “Letter of Intent for the LUXE Experiment.” (arXiv:1909.00860).
5. J. A. Cardarelli, M. J. V. Streeter, C. Colgan, D. Hollatz, A. Alejo, C. Arran, C. D. Baird, M. D. Balcazar, E. Gerstmayr, **H. Harsh**, B. Kettle, E. Los, C. Roedel, F. Salgado, G. M. Samarin, G. Sarri, A. G. R. Thomas, C. I. D. Underwood, M. Zepf, and S. P. D. Mangles, “Shock injection producing narrow energy spread, GeV electron beams from a laser wakefield accelerator,” in *APS Division of Plasma Physics Meeting Abstracts*, vol. 2019 of APS Meeting Abstracts, p. BO6.006, 2019.

# Danksagung

As I stand at the culmination of an incredible journey, it just feels like yesterday when a curious me was excited about joining this research group in 2018. During this time I was privileged to work at world class research facilities alongside brilliant scientist and travel to international schools and conferences. By overcoming the challenges and adapting to the new ways along this arduous journey, I have learned an awful lot.

A warm thanks to my supervisor Matt, for guiding this 'young' *Padavan* through this complex (and sometimes bewildering) world of Laser-Particle acceleration. Your wisdom (I still have no clue how you do those quick calculations), encouragement and definitely the unending patience have shaped not just my research but my growth as a scientist. Moreover, thanks for keeping the door open for all the discussions and letting me work on many interesting projects.

A heartfelt thanks to Andreas, Dominik, Alex, Christian and Daniel Ullman for showing me the ropes for doing such complex yet fascinating experiments and Georg for taking care of all laser related issues during my beamtime at JeTi200. A special shout out to my international colleagues Elias and Guillermo for all the encouragement and motivation during my time at RAL. Daniel Seipt, I apologise for dumping all those silly theory and simulation questions on you but you always explained the nitty-gritty details with patience. Thanks also to Felipe, my partner-in-crime in lab and also in office for the countless hours spent troubleshooting, laughing, and occasionally shedding tears which created the bond that go beyond the boundaries of academia.

To my friends outside academia, in particular Alperen, Rishika, Janna and Dietrich, thanks for keeping me sane with pub visits, coffee breaks, Mensa gathering and your witty behaviours.

To Reena, thanks for taking utmost care of me during my lows and celebrating all the little successes in your own unique ways. I promise I will try to cook more delicious food for you in future.

To my brother, Rajat, thanks for distracting me with your usual funny stories and coping with my sudden radio silences.

To my parents, thank you for consistently being by my side, for your unwavering love and support in every circumstance. This journey would not have been achievable without you.



# Ehrenwörtliche Erklärung

Ich erkläre hiermit ehrenwörtlich, dass ich die vorliegende Arbeit selbständig, ohne unzulässige Hilfe Dritter und ohne Benutzung anderer als der angegebenen Hilfsmittel und Literatur angefertigt habe. Die aus anderen Quellen direkt oder indirekt übernommenen Daten und Konzepte sind unter Angabe der Quelle gekennzeichnet.

Weitere Personen waren an der inhaltlich-materiellen Erstellung der vorliegenden Arbeit nicht beteiligt. Insbesondere habe ich hierfür nicht die entgeltliche Hilfe von Vermittlungs- bzw. Beratungsdiensten (Promotionsberater oder andere Personen) in Anspruch genommen. Niemand hat von mir unmittelbar oder mittelbar geldwerte Leistungen für Arbeiten erhalten, die im Zusammenhang mit dem Inhalt der vorgelegten Dissertation stehen.

Die Arbeit wurde bisher weder im In- noch im Ausland in gleicher oder ähnlicher Form einer anderen Prüfungsbehörde vorgelegt.

Die geltende Promotionsordnung der Physikalisch-Astronomischen Fakultät ist mir bekannt.

Ich versichere ehrenwörtlich, dass ich nach bestem Wissen die reine Wahrheit gesagt und nichts verschwiegen habe.

Ort, Datum

Harsh

**CV**

**CV**

# HARSH HARSH

PARTICLE PHYSICIST

## KONTAKT

📞 +49 17636722108  
 ✉️ harsh.harsh@uni-jena.de  
 📍 07745, Jena,  
 Deutschland

## FÄHIGKEITEN

Elektronenstrahlerzeugung und transport  
 Arbeiten mit unterdichtetem Plasma  
 Computational modelling  
 Experimente in der Vakuumkammer  
 Arbeiten in Reinräumen  
 LateX, Python

## AUSBILDUNG

**PhD Student**  
**Helmholtz Institute, Jena, Deutschland**  
 2019- Heute

**Masters of Science in Photonics**  
**Abbe School of Photonics, Jena, Deutschland**  
 2016-2018

**Bachelor of Science in Physics**  
**University of Delhi, India**  
 2010-2013

## SPRACHEN

Englisch C2  
 Deutsch B2  
 Hindi Native

## KURZPROFIL

Erfahrener Physiker mit Fachkenntnissen in der Entwicklung und Betrieb von Elektronenstrahlerzeugung und -transport. Kenntnisse in den Bereichen Vakuumtechnik, CCD-Betrieb, Bildgebungsverfahren, Röntgenstrahlen und umfassende Datenanalyse mit Python. Darüber hinaus habe ich auch die Planung und Überwachung eines wissenschaftlichen Projekts demonstriert.

## BERUFLICHE ERFAHRUNGEN

### Wissenschaftlicher Mitarbeiter

Helmholtz Institute Jena

2019-2024

- Arbeit an der Elektronenbeschleunigung mit Hilfe eines ultra-intensiven JETI200-Lasersystems zur Erzeugung von Elektronen und Röntgenstrahle.
- Entwurf des experimental set-up für die Erzeugung und den Transport von Elektronenstrahlen in der Vakuumkammer.
- Charakterisierung und Diagnose der Elektronenstrahlen und der Röntgenemission.
- Detektor-Kalibrierung und Datenanalyse für Elektronen- und Röntgenstrahlen.

### Master Student

Rutherford Appleton Lab, Oxford, England

2018-2019

- Arbeitete mit einem internationalen Team von Wissenschaftlern an einem Photonen-Photonen Collider.
- Bewertung des background signal bei Elektron-Photonen Kollisionen zur Optimierung des Versuchsplans.

## INTERESSEN

- Sports: Badminton, Volleyball, Wandern, und Schwimmen
- Hobbys: Kochen, Lesen und Meet-ups